Buckling Type, Domain Boundaries and Donor Atoms: Atomic Scale Characterization of the Si(111)-2×1 Surface

Dissertation
zur Erlangung
des mathematisch-naturwissenschaftlichen
Doktorgrades
„Doctor rerum naturalium“
der Georg-August-Universität Göttingen

vorgelegt von
Karolin Löser
aus Göttingen

Göttingen, 2013

Referent: Prof. Dr. R. G. Ulbrich
Korreferent: Prof. Dr. M. Rohlfing
Tag der mündlichen Prüfung:

Contents

Chapter 1

Introduction

Although the silicon (Si) (111)-2×1 surface reconstruction was one of the first sample systems which were thoroughly investigated following the invention of the scanning tunnelling microscopy (STM) in 1981 [1–5], there are still open questions and phenomena which are not yet resolved.

One of these open questions concerns the buckling of the π-bonded chains which form the Si(111)-2×1 reconstruction. Only recently, it was shown that the two buckling possibilities – positive and negative buckling of the atoms of the π-bonded chain – coexist [6]. This means that the Si(111)-2×1 surface belongs to the semiconductor systems where different atomic configurations with similar total energies close to the ground state exist in parallel. Semiconductor systems offering two such meta-stable states with similar total energies close to the ground state are of increasing interest due to potential applications for nanoscale devices, e.g. rewritable nanoscale memory [7]. The system Appelbaum *et al.* consider is the Si(001) surface where differently tilting dimers lead either to a c(2×4) or to a p(2×2) reconstruction. The same applies for the germanium (Ge)(001) surface. The reconstruction can be reversibly changed from c(2×4) to p(2×2) applying different voltages and tunnelling currents [8–11]. Calculations confirm the influence of electric fields and charge injection on the stability of the two reconstructions [12, 13]. The different buckling types of Si(111)-2×1 might present a similar system. In chapter 4, the two buckling types are investigated with special attention to the surface band structure and the relative positions of the surface bands.

A phenomenon first described in 1999 is the movement of a domain boundary over the distance of a few nanometres (nm) [14]. Only recently, Studer *et al.* revived the topic by studying strain induced domain boundary movement between two domains with positive buckling [15]. The case of mobile domain boundaries treated in chapter 5 of this thesis is slightly different, as it involves two differently buckled domains. Thus, the movement of the domain boundary

also constitutes a switching between the two meta-stable reconstructions of the Si(111)-2×1 surface.

The third topic of this thesis are the signatures of phosphorus (P) atoms. Semiconductors are doped with atoms of a different chemical element in order to control their conductivity. The most common elements used to dope Si are boron (B) for doping with positive charge carriers (p-type) and P and arsenic (As) for doping with negative charge carriers (n-type). Consequently, the properties of substitutional P atoms in bulk Si have been studied nearly as long as Si itself [16, 17]. Substitutional P atoms in the Si(111)-2×1 surface at room temperature (RT) first have been studied by Trappmann *et al.* in 1997 [18]. In that study, voltage dependent contrast patterns were attributed to signatures of P atoms. The assignment of different contrast patterns to P atoms at the four substitutional sites of the Si(111)-2×1 surface was achieved in low temperature (LT)-STM studies for π-bonded chains with positive buckling in 2004 [19].

In chapter 6, the sites corresponding to signatures of substitutional P atoms in negatively buckled π-bonded chains are determined. Improvements in the sample preparation enabled measurements on quasi-infinite π-bonded chains (length > 1 μm). In such areas, P atoms at the different sites in the surface layer show the same topographic signatures as for shorter chains, but in addition, signatures of P atoms in subsurface layers are found. Surprisingly, spectroscopic measurements reveal substantial differences in the origin of the signatures which P atoms induce within the surface band gap. This is investigated in the second part of chapter 6. The origin cannot be a defect state of the P atom itself, as the defect state is strongly localised, and the signature extends over several nm along the π-bonded chains. The dispersion of the surface bands is important in order to explain the spatial extend of the signature in direction parallel to the π-bonded chains. Interactions between P atoms, with the π-bonded chains of different lengths, domain boundaries and other defects cannot be neglected when one investigates complex system. They must be taken into account considering the differences in the energetic positions of signatures of P atoms in various configurations.

Chapter 2

Si(111)-2×1

This chapter introduces the Si(111)-2×1 surface reconstruction which is investigated in this thesis. It starts with the formation and atomic configuration of this reconstruction, describes the electronic structure, and concludes by introducing different defect structures. Some more detailed aspects, which are necessary for interpreting the STM results, are treated in the respective chapters.

2.1 Surface reconstruction

Cutting a crystal causes numerous broken bonds in the unreconstructed surface where the surface atoms would bond to the next layer of atoms. As these dangling bonds are energetically unfavourable, many surfaces form surface reconstructions in order to reduce dangling bonds and lower the total energy.

Si is a covalent semiconductor crystallising in a diamond lattice with a lattice constant of a=5.43 Å [21] (Fig. 2.1a). A cut along the (111)-plane results in an unreconstructed surface with unit vectors of length $a_1 = a_2 = \frac{\sqrt{2}}{2}a_0 = 3.84$ Å and a threefold rotational symmetry. The distance between two adjacent Si(111) planes (and thus the height of monoatomic steps) is 3.14 Å. The unreconstructed Si(111)-1×1 surface has one dangling bond per unit cell. Depending on the energy available for the formation, different surface reconstructions may be obtained. The most famous one is Si(111)-7×7 – the first surface investigated by STM [22] – which reduces the dangling bonds significantly from 49 to 19. This is achieved by considerably restructuring the surface, including dimers, adatoms, and a stacking fault (DAS-model [20], see Fig. 2.1b). The necessary energy is obtained by heating the sample up to 1000° C and cooling it slowly. The 7×7 reconstruction forms at about 860° C [23].

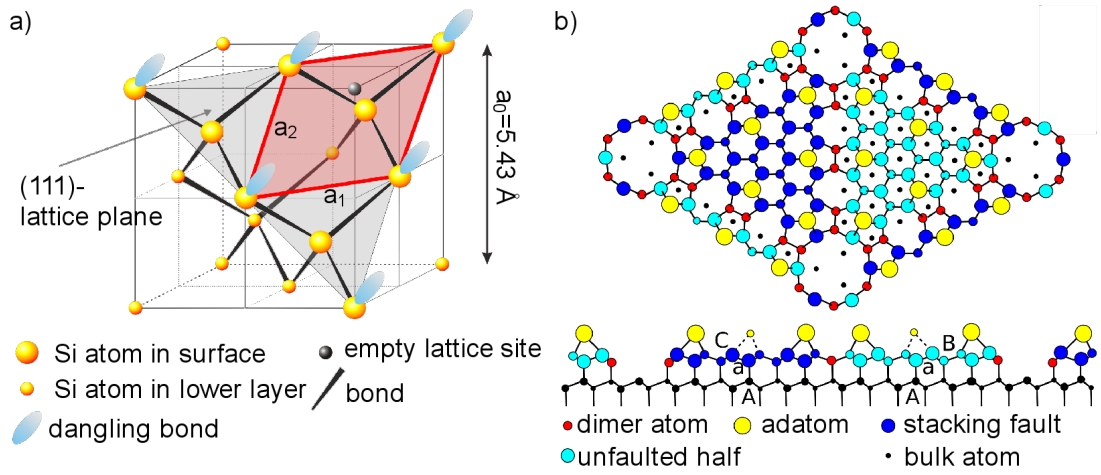

Figure 2.1: *(a) Model of the diamond lattice structure of silicon: The (111)-plane is displayed as shaded layer and the atoms of the unreconstructed surface are enlarged. The surface unit cell is marked in red. Surface buckling and dangling bonds at every second atom are visible.*
(b) Si(111)-7×7 surface reconstruction: Surface unit cell in the dimer-adatom-stacking fault (DAS)-model [20].

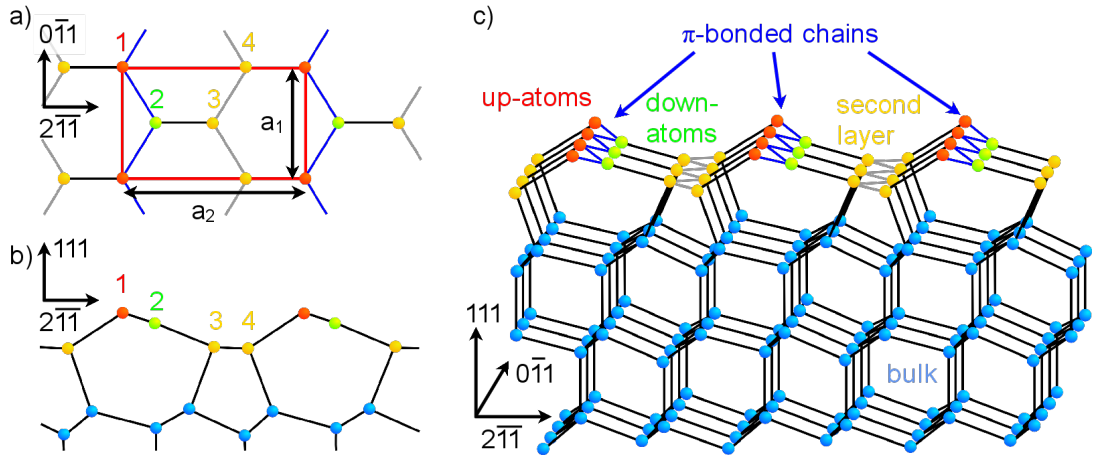

Figure 2.2: *Atomic configuration of the buckled π-bonded chain model: (a) top view, (b) side view, (c) perspective view.*

In contrast, the 2×1 reconstruction is found only at samples which were cleaved at RT or below. It is a meta-stable reconstruction which is transformed into the stable 7×7 if enough thermal energy is provided. The π-bonded chain model by Pandey [24] is the best fitting description of the 2×1 reconstruction. LEED studies by Himpsel at al. [25] led to a modification of the model, including a buckling of the atoms in the π-bonded chain. Figure 2.2 depicts different views of the Pandey model with the additional buckling. The unit vectors are $a_1 = 3.84$ Å in <0$\bar{1}$1>- and $a_2 = 6.65$ Å in <$\bar{2}$11>-direction. The π-bonded chains

are formed by zigzag rows of atoms in <0$\bar{1}$1>-direction. The half filled p_z-orbitals of the atoms in the π-bonded chain (still two dangling bonds per 2×1 unit cell) form π-bonds which results in a reduction in surface energy. According to *ab initio* calculations, the height difference between 'up' atom (site 1) and 'down' atom (site 2) is 0.51 Å. The atoms next to 'down' (site 3) and 'up' atom (site 4) lie 1.0 Å lower than the π-bonded chain [19,26].

There are two possibilities for the atoms to buckle (Fig. 2.3a+b) which show a mirror symmetry in the upper three surface layers (Fig. 2.3c). This causes difficulties in determining the buckling type. In positively buckled π-bonded chains the atoms on the side in ($\bar{2}$11)-direction are higher, negative buckling is characterised by a higher atom on the side in (2$\bar{1}\bar{1}$)-direction of the zigzag chain. Calculations predict similar surface band structures and total energies for the two configurations [27]. Until Bussetti *et al.* could prove the co-existence of positive and negative buckling for highly n-doped samples and at low temperatures in 2011 [6], it was assumed by experimentalists as well as theoreticians that all Si(111)-2×1 surfaces were buckled the same way. Nie *et al.* found that in RT-STM measurements the buckling of the π-bonded chains of the Si(111)-2×1 surface is positive while it is negative for Ge(111)-2×1 [29]. This was in good agreement with first principle calculations by Rohlfing *et al.* [30], who found negative buckling favourable for Ge(111)-2×1, while Si(111)-2×1 should show positive buckling. Bussetti *et al.* assumed that while normally positive buckling is preferable, the total energy of the highly n-type doped samples may be reduced by the occupation of the empty states of the negatively buckled π-bonded chains. Thus, domains with negative buckling form in addition to the positively buckled areas [6].

2.2 Electronic structure

Bulk Si is an indirect semiconductor with the maximum of the projected bulk valence band (BVB) at $\bar{\Gamma}$, while the projected bulk conduction band (BCB) mini-

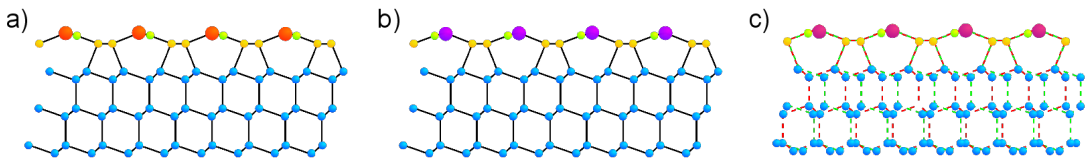

Figure 2.3: *Equilibrium structures of positively (a) and negatively (b) buckled π-bonded chains [27], (c) broken red lines: positive buckling, broken green lines: mirrored structure of negative buckling (on the basis of [28]).*

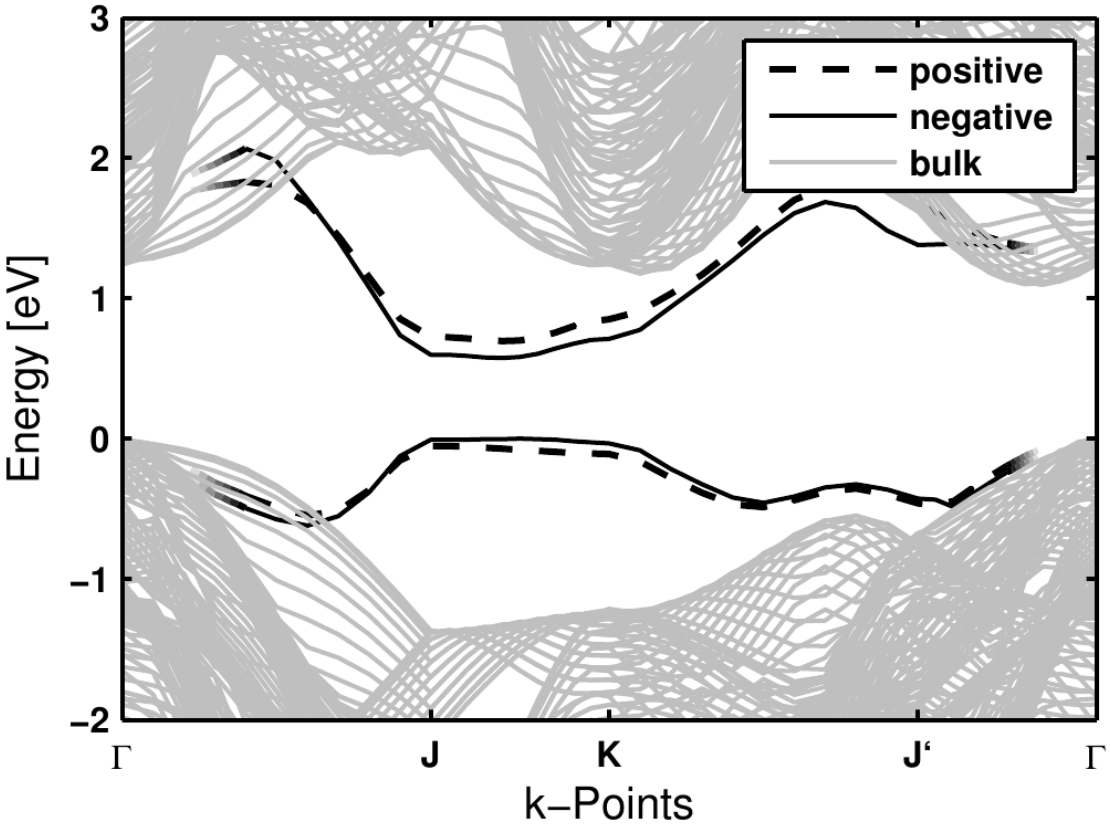

Figure 2.4: *Calculated electronic surface dispersion for positive (dashed lines) and negative (solid lines) buckling in comparison with the projected bulk band structure (grey), resulting from the GW band-structure theory [31].*

mum is located near $\bar{\mathrm{K}}$ (grey in Fig. 2.4). The width of the band gap (E_G) at RT is $\mathrm{E}_{\mathrm{GB}} = 1.12\,\mathrm{eV}$ [32,33]. The electronic structure of the Si(111)-2×1 surface is dominated by the dangling bond states of π-surface conduction band (SCB) and π-surface valence band (SVB) (see the lines in Fig. 2.4). The empty state π-SCB is located at the 'down'-atom and the filled π-SVB state at the 'up'-atom [19,26]. Density functional theory (DFT) calculations [19,27,31] and inverse and normal angle resolved photo electron spectroscopy (ARPES) measurements [34–36] show a strong dispersion along the π-bonded chains ($\overline{\Gamma J}$) while in perpendicular direction ($\overline{JK}$) the dispersion is very weak. The surface states have a direct band gap at $\bar{J}$, the boundary of the surface Brillouin zone.

Positive and negative buckling lead to similar band structures. Only the region near the surface band gap and the band gap itself differ: According to the band structures calculated by M. Rohlfing, the band gap is smaller for negative buckling ($\mathrm{E}_{\mathrm{Gn}} = 0.58\,\mathrm{eV}$) than for positive buckling ($\mathrm{E}_{\mathrm{Gp}} = 0.75\,\mathrm{eV}$), and the surface bands for negative buckling lie within the surface band gap of positive

buckling (Fig. 2.4: solid (positive buckling) and dashed (negative buckling) lines) [6,27,31].

The surface bands are located within the band gap of bulk Si which results in Fermi level pinning for doped samples [37]. This is important for the interpretation of STM measurements. The sample bias voltage (V_{bias}) is thus directly related to the electron energy via $E = E_F + eV$.

In this thesis, highly n-type doped samples are studied. For high n-type doping with P in the bulk, Fermi energy (E_F) is located in the shallow donor band ∼45 meV below the BCB [38]. At the surface, there is a surface state within the bulk band gap. The high density of states of the conduction surface band in combination with a large charge accumulation as a result from the n-doped bulk leads to a quasi pinning of E_F near the SCB minimum [37]. This situation is comparable to a Schottky-barrier with a barrier height corresponding to ΔE_F ($\Delta E_{Fp} = \Delta E_{SCp-BC} - 0.045\,\text{eV} = 0.355\,\text{eV}$ with $\Delta E_{SCp-BC} = 0.4\,\text{eV}$ for positive buckling, corresponding to the calculations by M. Rohlfing (Fig. 2.4) [31]).

Figure 2.5 illustrates the resulting bending of the bulk bands according to the rigid band model. According to H. Föll [39] the width Debye length (λ_D) of the space charge region may be calculated with the following formula:

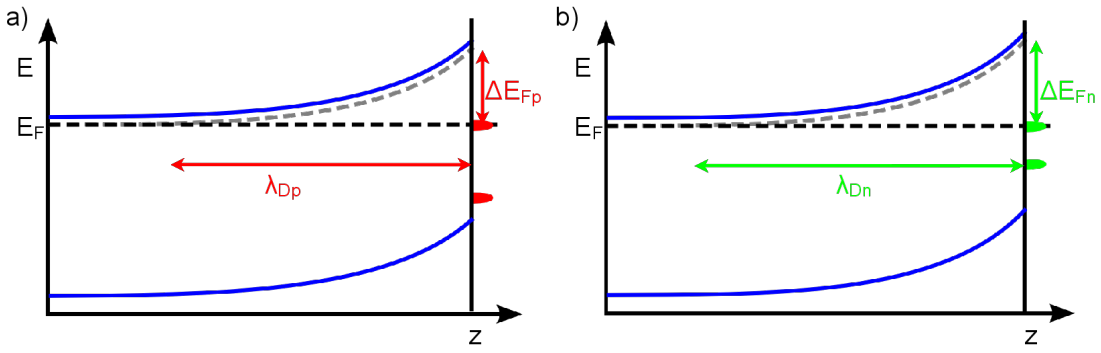

Figure 2.5: *Bending of the bulk bands due to the filled SCB states according to the rigid band model: (a) positive buckling, (b) negative buckling.*

$$\lambda_D = \sqrt{\frac{2\epsilon\epsilon_0 \Delta E_F}{e^2 N_D}} \tag{2.1}$$

with:
- ϵ_0 : vacuum permittivity
- ϵ : relative permittivity of silicon
- ΔE_F : difference of energetic positions of Fermi energies relative to the bulk bands at the surface and in the bulk
- e : elementary charge
- N_D : donor concentration of the sample

The width of the resulting space charge region for positive buckling is λ_{Dp} = 9.0 nm and, considering the donor concentration of the sample, the resulting surface charge density (ρ) is $\rho_p = 5.4 \cdot 10^{12} cm^{-2}$ (Fig. 2.5a). For negative buckling, with ΔE_{SCn-BC} = 0.485 eV [31], the Schottky barrier $\Delta E_{Fn} - 0.045 = \Delta E_{SCn-BC} - 0.045$ eV = 0.440 eV is higher than for positive buckling. Consequently, a wider space charge region with λ_{Dn} = 10.0 nm and higher surface charge density $\rho_n = 6.0 \cdot 10^{12} cm^{-2}$ at negatively buckled domains develop (Fig. 2.5b).

2.3 Surface defects on Si(111)-2×1

There are three different, intrinsic surface defects which occur in doped Si(111)-2×1 surfaces and have effects on the atomic and electronic structure of the surface: surface steps, domain boundaries, and dopant atoms. On the one hand, these defects are interesting objects to study by themselves. On the other hand, they may be utilised as tools to investigate surface properties which would be not accessible otherwise.

2.3.1 Surface steps - Coulomb gap

Monoatomic steps on Si(111) have a height of 0.314 nm and effectively disconnect the π-bonded chains. In contrast to steps on gallium-arsenide (GaAs)(110) [40], Si(111)-2×1 surface steps are not charged and show only the geometric step height of monoatomic steps in STM measurements at all voltages [3].

In former studies by J. K. Garleff *et al.*, steps of different widths have been utilised to study the effects of chain length on the electronic structure of the

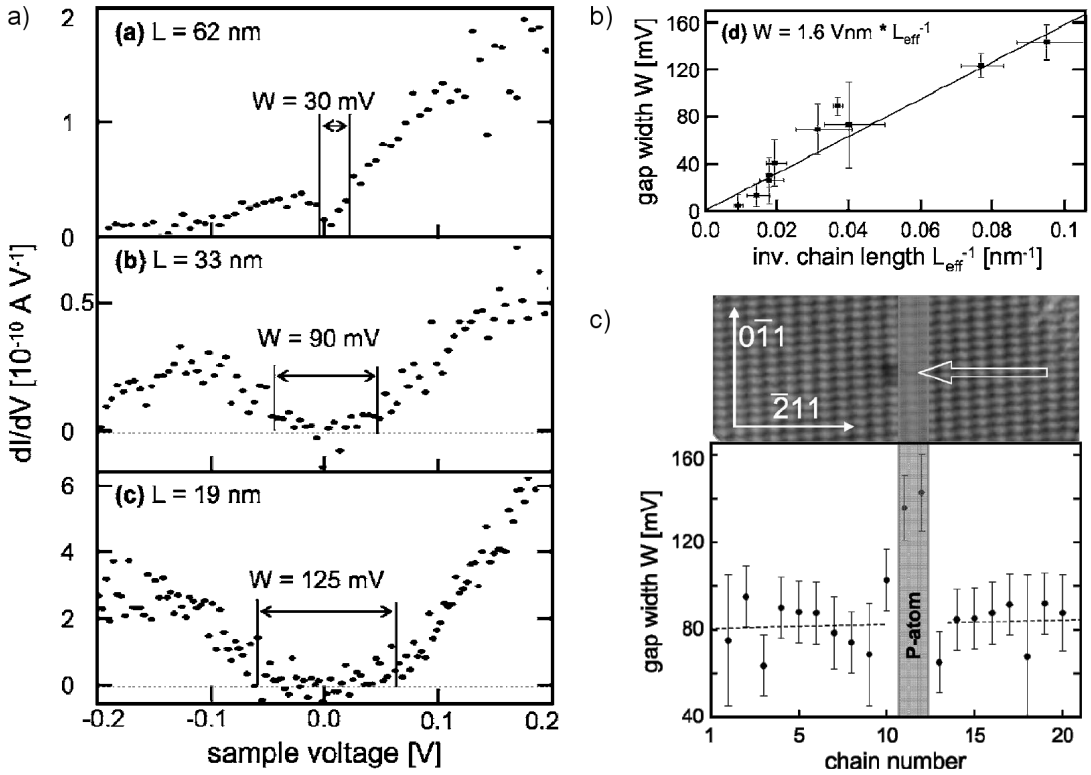

Figure 2.6: *(a) High resolution differential conductivity (dI/dV) spectra on π-bonded chain segments with different length [41].*
(b) Linear dependence of gap width on inverse chain length [41].
(c) Width of Coulomb gap on free chains compared to chains cut by a P atom [41].

π-bonded chains. A Coulomb gap was found which scales with the inverse chain length (Fig. 2.6). The width of the Coulomb gap is also affected by P atoms within the chain. This proves that P atoms divide the chains as far as electrons are concerned. The case of a P atom between two chains demonstrates that the coupling between neighbouring π-bonded chains is negligible, as only the two directly adjacent chains show a wider Coulomb gap. The other chains are unaffected (Fig. 2.6c) [41].

2.3.2 Domain boundaries - different buckling types

There are multiple possibilities for the arrangement of the 2×1 reconstruction with respect to the unreconstructed 1×1 surface (Fig. 2.7a). Due to the threefold symmetry of the Si(111)-plane the π-bonded chains can run in the three equivalent lattice directions [0$\bar{1}$1], [10$\bar{1}$], and [$\bar{1}$10] (blue, green, and red in Fig. 2.7a). In addition, there are two possibilities for the π-bonded chains to be placed

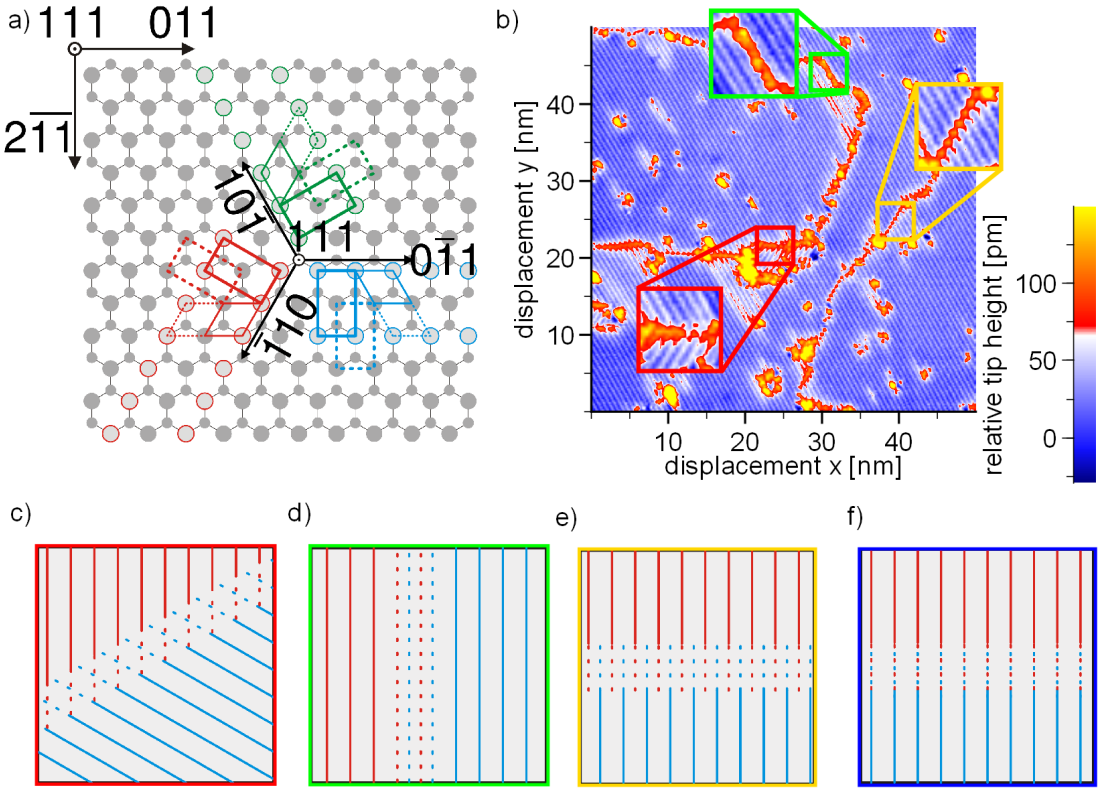

Figure 2.7: *(a) Atomic positions of the six configurations, green: [10$\bar{1}$]-direction, blue: [0$\bar{1}$1]-direction, red: [$\bar{1}$10]-direction; solid and dashed lines: two possibilities of up-atom positions with displacement of half a 2×1 unit cell;*
(b) STM topography showing domain boundary type I (red), type II (green) and type III (yellow) [V_{bias} = -1 V; I_t = 0,1 nA; T = 300 K];
(c-f) schemes of type I (c), type II (d), type III (e), and type IV (f) domain boundaries [28, 31].

in relation to the underlying bulk structure. These possible positions have a translational displacement by half a 2×1 unit cell in the direction perpendicular to the chains (solid and dashed lines in Fig. 2.7a). Thus, there are six different positions of the π-bonded chains regarding the unreconstructed Si(111)-1×1 structure. Taking the two different buckling types into consideration, there are all in all twelve different configurations.

Domains of these configurations are separated by four types of domain boundaries. Figure 2.7b shows a topography image of a multi-domain surface where the first three types occur. The boundaries are visible as brighter lines in the topography image. The first type unites all boundaries with a rotation by 120° between the π-bonded chains of the two domains (Fig. 2.7c). Type II and III domain boundaries both separate domains with π-bonded chains running in the same direction but with a displacement by half a unit cell. A type II bound-

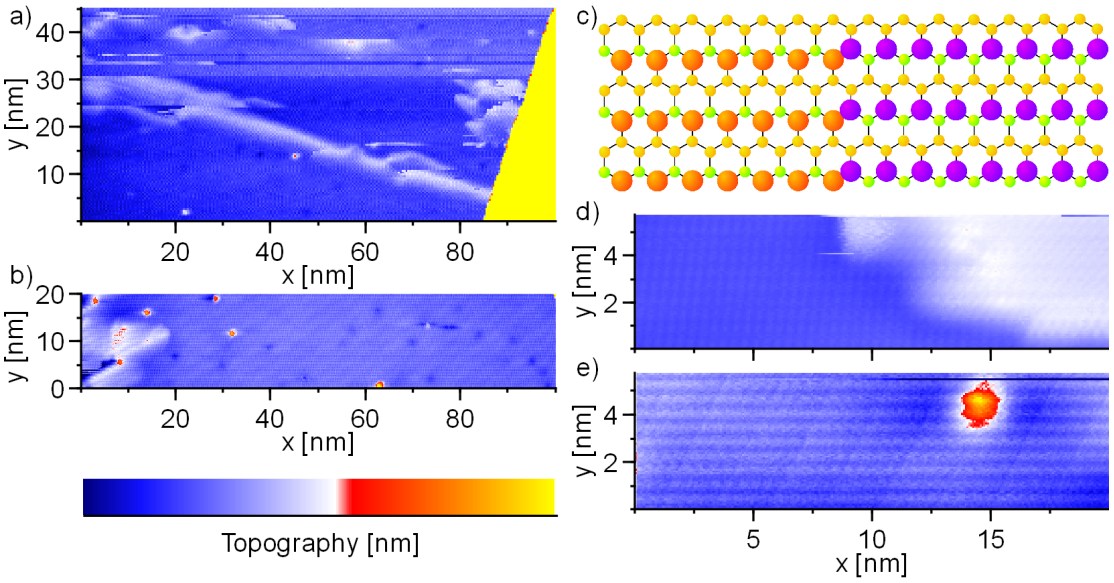

Figure 2.8: *Type IV domain boundaries without displacement of π-bonded chains: (a) These boundaries occur mainly next to surface steps [V_{bias} = -2.0 V; I_t = 0.1 nA; T = 6 K]. (b) Defects pin the position [V_{bias} = -0.5 V; I_t = 0.1 nA; T = 6 K]. (c) Model of a type IV domain boundary: big red circles – up-atoms (positive buckling), big violet circles – up-atoms (negative buckling), green circles – down-atoms, yellow circles – atoms of lower chain. (d+e) While there is a high contrast difference at -0.5 V (d) the boundary is invisible at +1.0 V (e) [V_{bias} = -0.5 V / +1.0 V; I_t = 0.1 nA; T = 6 K].*

ary runs parallel to the chains (Fig. 2.7d) while a type III boundary separates frontally meeting chains (Fig. 2.7e). A type IV domain boundary separates frontally meeting π-bonded chains without rotation or displacement of the surface unit cell but with a change of the buckling type (Fig. 2.7f and 2.8). These boundaries mainly occur next to surface steps (Fig. 2.8a) and show as cloud-like contrast enhancement at -0.5 V. Defects pin the position of the domain boundaries (Fig. 2.8b). The only difference between the two domains separated by a type IV domain boundary is in the positions of 'up' and 'down' atoms (Fig. 2.8c). The π-bonded chains are not interrupted. But the 'up'-atoms are at different positions with respect to the surface unit cell. The domain boundary is clearly visible at -0.5 V. At this voltage, positively and negatively buckled π-bonded chains exhibit a difference in the local density of states (LDOS). Therefore, a high contrast difference in the STM image occurs (Fig. 2.8d). The STM image at +1.0 V shows that there is no displacement between the π-bonded chains of the two domains (Fig. 2.8e). In this work, domain boundaries are utilised as tools to investigate the properties of positive and negative buckling.

2.3.3 Dopant-atoms: surface vs. bulk properties

The samples investigated in this thesis are heavily n-type doped with P atoms. As the SCB is partially filled due to the high doping, the surface is metallic. This leads to the assumption that P atoms in the bulk do not show up in STM, as their charge is easily screened by the electrons in the surface state. The P atoms are distributed statistically in bulk material as all positions are equivalent. Trappmann *et al.* [18] also found statistically distributed P atoms at the surface in RT-STM studies. These RT studies assign voltage dependent contrasts to the P atoms in the surface layer: At -1.1 V there is a depression at the site of the P atom, while at +1.1 V the contrast shows a protrusion (Fig. 2.9a+b). There is also an anisotropic contrast with an extension of about 10 nm along one single or two adjacent π-bonded chains. In surfaces with positive buckling, this contrast shows up at -0.4 V in RT images [18] and at -0.5 V at a temperature of 8 K [43]. This elongated contrast appears, too, for positive doping with boron at a voltage of +0.4 V [44]. Subsurface P atoms were not observed, up to now, but Studer found signatures of subsurface Sb and bismuth (Bi) atoms (Fig. 2.9c) [42].

The charge state of the P atoms deep in the bulk is neutral except for some donors ionised by thermal energy while in the space charge region near the surface all P atoms are ionised and thus positively charged. The P atoms directly in the surface layer have a strongly enhanced binding energy of more then 0.4 eV due to the fact that they have to be described as defects in a quasi-one-dimensional (1D) chain. Therefore, they show a neutral charge state. This is supported by density functional theory (DFT) calculations which show a strong localisation of the additional charge from the P atom within 1-2 angstroms of its binding site [45].

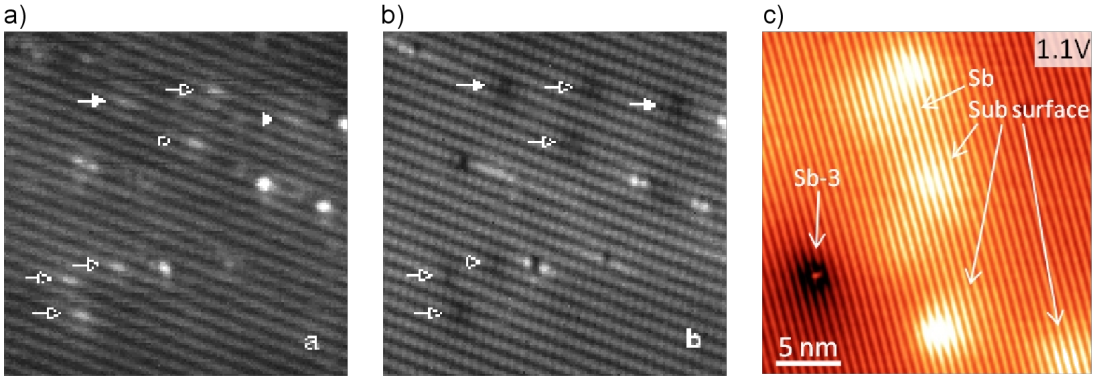

Figure 2.9: *(a+b) P atoms in Si(111)-2×1 at RT at different sample bias voltages, arrows indicate dopant-induced features [15 nm×15 nm; I_t = 0.3 nA; T = 300 K; $N_D = 6 \cdot 10^{19}$ cm^{-3}]: (a) V_{bias} = +1.1 V, (b) V_{bias} = -1.1 V [18].*
(c) Signatures of buried antimony (Sb) atoms beneath Si(111)-2×1 [42].

Chapter 3

Scanning tunnelling microscopy

STM was the first method allowing atomically resolved investigation of flat, conducting surfaces in real space. Although other methods, which produce real space images, existed, these were either limited to the investigation of tips (field ion microscopy (FIM)) or the resolution was limited to displaying atomic steps but not the details of surface atom positions (scanning electron microscopy (SEM), low energy electron microscopy (LEEM)). Until 1981, when Gerd Binnig and Heinrich Rohrer developed the STM [5], the atomic structure of flat surfaces was investigated using diffraction methods, for example low energy electron diffraction (LEED) and reflection high energy electron diffraction (RHEED). While these methods are well suited to gain information about periodic structures such as surface reconstructions, it was impossible to resolve the local structure of a surface, including defects, surface steps, and dopant atoms in semiconductors. The invention of atomic force microscopy (AFM) for non-conducting samples [46], magnetic force microscopy (MFM) to investigate magnetic properties [47], Kelvin probe force microscopy (KPFM) [48], and a lot of other methods enlarged the variety of scanning probe methods significantly.

STM itself became a more powerful tool for surface analysis by the development of advanced data acquisition modes, for example dI/dV-spectroscopy, potentiometry, and multiple-tips STMs.

3.1 Basic concept of STM

STM is a scanning probe method. This means that data is acquired by scanning a surface step by step with a sharp tip and performing measurements at each position. The result is a map of the measured quantity, for example the relative tip height.

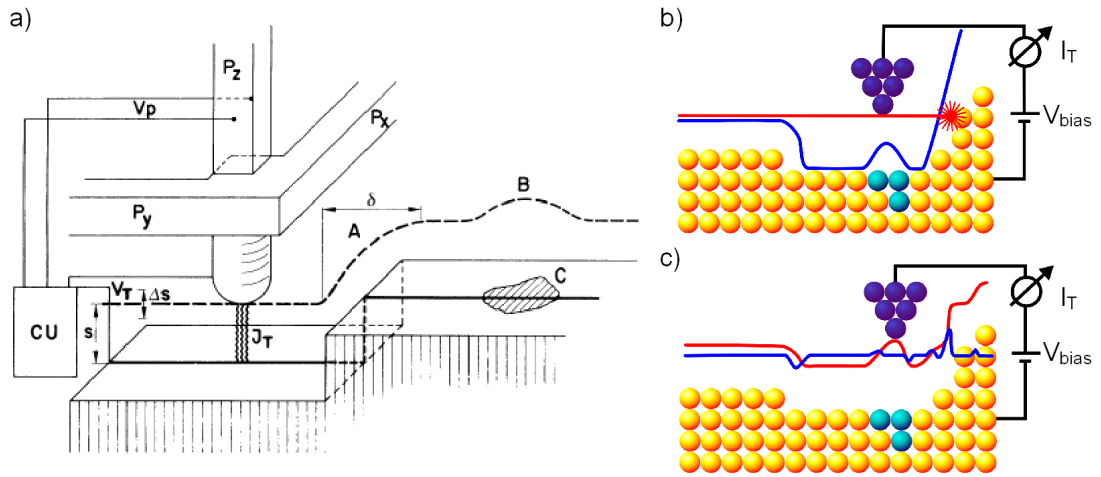

Figure 3.1: *(a) Original STM setup using a tripod piezo as proposed by Binnig and Rohrer [5]. (b) Constant height and (c) constant current scanning modes: schematic profile of tunnelling current (blue) and tip height (red), atoms of a different chemical element (turquoise) resulting in a higher tunnelling current in b.*

As it is crucial to move the tip with subatomic resolution, piezo crystals are employed for the precise positioning of the tip. Three piezo elements, one for each spatial coordinate, were used in the first STM design by Binnig and Rohrer [5]. For this thesis, a different STM design is used as will be explained in section 3.3.3.

The actual measurements rely on the quantum-mechanical tunnelling effect which leads to a small tunnelling current (I_T) between two conductors separated by a few angstroms (Å) of isolating material or vacuum when a bias voltage is applied between sample and tip (V_{bias}). The tunnelling current is very sensitive to the thickness of the isolating layer. For a detailed description of the tunnelling current see section 3.2. The electron energies are limited to a few electron Volts (eV) in most setups, and thus no destruction of the investigated sample is caused.

There are two different modes for scanning the surface:

1. In **constant height mode** the tip is scanned over the surface without height adjustment and the tunnelling current is recorded (Fig. 3.1b). This method is very fast because no feedback loop is needed to adjust the tip height. But it may only be used on atomically flat surfaces, as the tip might crash into higher surface structures.

2. For the measurements of this thesis, **constant current mode** is used. Here the tip height is adjusted via a proportional-integral (PI)-feedback loop in order to obtain a constant current at all positions. The measured quantity in this mode is the relative height of the tip. (Fig. 3.1b)

3.2 Theoretical description of the tunnelling current

In this section, theoretical descriptions for different tunnelling geometries are summarised, mainly following the approach of R. Wiesendanger [23] to the topic, while concentrating on the descriptions most important for this thesis. Another comprehensive theoretical treatment of the tunnelling current can be found in [49].

3.2.1 Quantum tunnelling effect

Tunnelling of particles through a potential barrier is an effect that can only be explained within quantum theory. In classical physics, a particle with smaller energy than the height of the potential barrier is never able to pass this barrier (Fig. 3.2a). The wave – particle dualism in quantum theory [50] leads to an evanescent wave amplitude within the barrier and thus to a finite probability of finding the particle at the other side of the barrier. This process is called tunnelling. First experiments and theories based on tunnelling theory were, for example, the observation and explanation of field emission [51,52], ionisation of hydrogen atoms [53], and a theoretical treatment of α-decay [54,55]. In the case of STM, electrons tunnel from the tip through vacuum into the sample and vice versa. The direction of the resulting tunnelling current depends on the applied bias voltage.

3.2.2 Tunnelling in one dimension

To keep the theoretical treatment as simple as possible, the following distinctions and constraints are made:

- **elastic tunnelling:** Only tunnelling processes with equal initial and final states of the electron are considered.

- **one- vs. three-dimensional potential barrier**

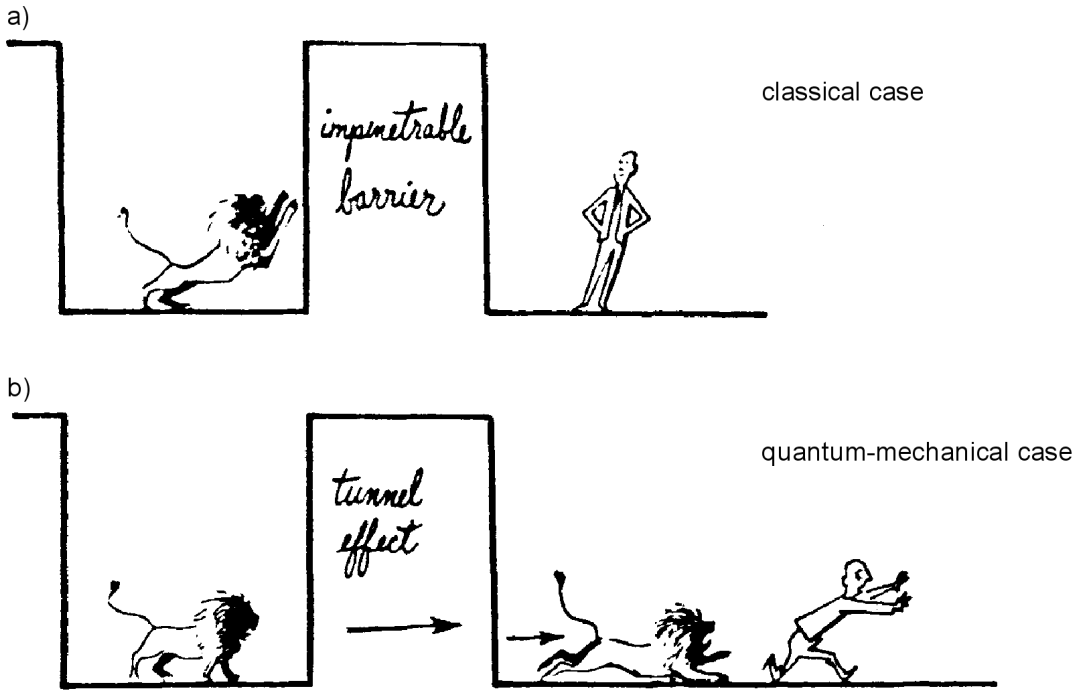

Figure 3.2: *Tunnelling through a potential barrier:*
(a) In the classical case the lion is unable to pass the barrier.
(b) In the quantum case there is a small probability of finding the lion on the 'wrong' side of the barrier.
According to Bleany, 'this illustration was used by Van Vleck (1979) in his last publication, the Julian E. Mack Lecture at his Alma Mater, the University of Wisconsin [56]' [57].

- **rectangular barrier shape**
- **time-independent vs. time-dependent approach**

At first, a time-independent approach for 1D, elastic tunnelling through a rectangular barrier is presented. An electron with mass m and energy E impinges on a barrier with height V_0. The time-independent Schrödinger equations and an *Ansatz* for the wave functions can be written for each of the three regions 1-3 (Fig. 3.3a):

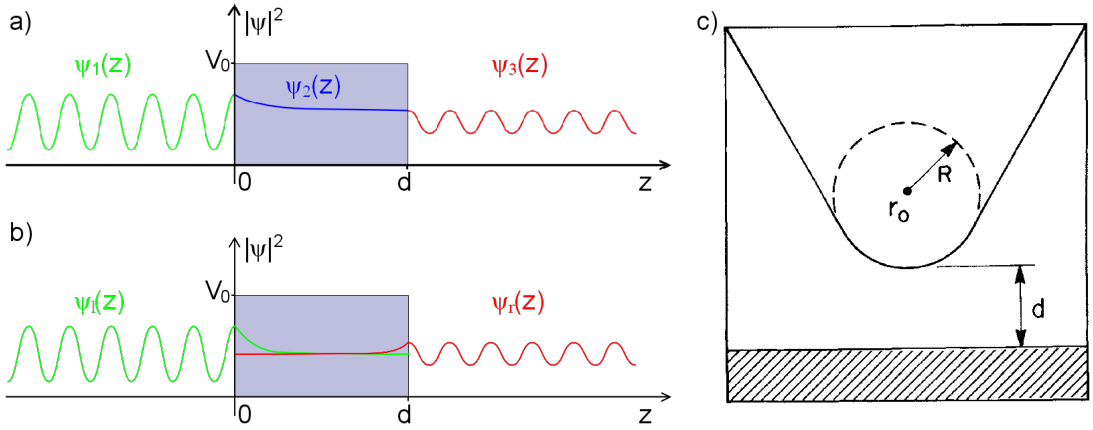

Figure 3.3: *(a+b) One-dimensional models of electrons tunnelling through a rectangular barrier with height V_0 and width d:*
(a) Time-independent Schrödinger equation, (b) time-dependent 'transfer-Hamiltonian approach' by Bardeen [58].
(c) Schematic picture of the tunnelling geometry assumed by Tersoff and Hamann: the arbitrarily shaped probe tip is spherical with radius R at the position with the shortest distance d to the surface (shaded). r_o is the centre of curvature of the tip [59].

$$\text{region 1:} \quad -\frac{\hbar^2}{2m}\frac{\partial^2}{\partial z^2}\Psi_1(z) = E\,\Psi_1(z) \tag{3.1}$$

$$\Psi_1(z) = e^{ikz} + Ae^{-ikz}; \qquad k = \frac{\sqrt{2mE}}{\hbar}$$

$$\text{region 2:} \quad -\frac{\hbar^2}{2m}\frac{\partial^2}{\partial z^2}\Psi_2(z) + V_0\Psi_2(z) = E\,\Psi_2(z) \tag{3.2}$$

$$\Psi_2(z) = Be^{-\kappa z} + Ce^{\kappa z}; \qquad \kappa = \frac{\sqrt{2m(V_0 - E)}}{\hbar}$$

$$\text{region 3:} \quad -\frac{\hbar^2}{2m}\frac{\partial^2}{\partial z^2}\Psi_3(z) = E\,\Psi_3(z) \tag{3.3}$$

$$\Psi_3(z) = De^{ikz}$$

The overall wave function is constructed by matching the Ψ_j and their first derivatives $\frac{d\Psi_j}{dz}$ at z = 0 and z = d, where the discontinuities of the potential are located. The following transmission coefficient T may be derived:

$$\mathrm{T} = \frac{\mathrm{j}_t}{\mathrm{j}_i} = |\mathrm{D}|^2 \tag{3.4}$$

with: $\mathrm{j}_t = \frac{\hbar \mathrm{k}}{\mathrm{m}} |\mathrm{D}|^2$ transmitted current density

$\mathrm{j}_i = \frac{\hbar \mathrm{k}}{\mathrm{m}}$ incident current density

for $\kappa \cdot \mathrm{d} \gg 1$:

$$\mathrm{T} \approx \frac{16\mathrm{E}(\mathrm{V}_0\text{-E})}{{\mathrm{V}_0}^2} e^{-2\kappa \mathrm{d}} \tag{3.5}$$

The factor $e^{-2\kappa \mathrm{d}}$ is the dominant part of the transmission coefficient and the source of the extreme sensitivity of the tunnelling current to the barrier width. Assuming an effective barrier height (V_0 - E) of 4 eV, a change of the barrier width by 1 Å results in a change of the tunnelling current by approximately one order of magnitude.

The same dependence on the barrier width d of the 1D-transmission coefficient may be obtained using a time-dependent 'transfer-Hamiltonian approach' as first suggested by Bardeen [58]. The advantage of this method is that it is more generally applicable, especially, it is not restricted to 1D problems. In his perturbation treatment of tunnelling Bardeen introduced approximate solutions to the exact Hamiltonian (Fig. 3.3b). $\Psi_l(z)$ ($\Psi_r(z)$) solves the Schrödinger equation for $z \leq 0$ ($z \geq d$) but decays exponentially on the right (left) side of the barrier instead of solving the Schrödinger equation. Within the barrier both wave functions decay exponentially:

$$\Psi_l(z) = ae^{-\kappa z}; \qquad z \geq 0 \tag{3.6}$$

$$\Psi_r(z) = be^{\kappa z}; \qquad z \leq \mathrm{d} \tag{3.7}$$

For an electron initially in state Ψ_l the transition rate into state Ψ_r may be computed starting with the time-dependent Schrödinger equation:

$$\begin{aligned} \mathrm{H}\Psi(t) &= i\hbar\frac{\mathrm{d}\Psi(t)}{\mathrm{d}t} && (3.8)\\ \text{with: } \mathrm{H} &= (\mathrm{H}_l + \mathrm{H}_r) + \mathrm{H}_T = \mathrm{H}_0 + \mathrm{H}_T \\ \mathrm{H}_0\Psi_l &= \mathrm{E}_l\Psi_l \\ \mathrm{H}_l(\mathrm{H}_r): &\ \text{Hamiltonian for the left (right) side of the barrier} && (3.9)\\ \mathrm{H}_T: &\ \text{transfer-Hamiltonian describing tunnelling from one side of the barrier to the other} \end{aligned}$$

Assuming that the wave function describing the whole system ($\Psi(t)$) is a superposition of the wave functions right and left of the barrier

$$\Psi(t) = \mathrm{c}(t)\Psi_l e^{-\frac{i\mathrm{E}_l t}{\hbar}} + \mathrm{d}(t)\Psi_r e^{-\frac{i\mathrm{E}_r t}{\hbar}}, \tag{3.10}$$

The effective tunnelling matrix element is

$$\mathrm{M}_{rl} = \int \Psi_r * \mathrm{H}_T\Psi_l \mathrm{d}z \tag{3.11}$$

For $\kappa\mathrm{d} \gg 1$ 'Fermi's golden rule' may be used. This leads to the following transmitted current:

$$\mathrm{j}_t = \frac{2\pi}{\hbar}|\mathrm{M}_{rl}|^2\rho_r \tag{3.12}$$

with: ρ_r: density of states in the final state

Using Ψ_l and Ψ_r from equations 3.6 and 3.7 results in:

$$\mathrm{T} \propto e^{-2\kappa\mathrm{d}} \tag{3.13}$$

3.2.3 Tunnelling theory for three-dimensional configurations

Due to the geometry of STM measurements – sharp tip in front of a flat surface – a 1D treatment of the problem is not sufficient. While the method of wave function matching becomes very difficult, the transfer-Hamiltonian approach is still applicable. The tunnelling current is given by:

$$\begin{aligned} I_T = & \frac{2\pi e^2}{\hbar} \sum_{\mu,\nu} \{ f(E_\mu)[1 - f(E_\nu + eV)] - f(E_\nu + eV)[1 - f(E_\mu)] \} \\ & \cdot |M_{\mu\nu}|^2 \delta(E_\nu - E_\mu) \end{aligned} \tag{3.14}$$

with:
- $f(E)$: Fermi function
- V : applied sample bias voltage
- $M_{\mu\nu}$: tunnelling matrix element between states Ψ_μ of the tip and Ψ_ν of the sample surface
- $E_\mu(E_\nu)$: energy state of $\Psi_\mu(\Psi_\nu)$ in absence of tunnelling
- $\delta(E_\nu - E_\mu)$: energy conservation (elastic tunnelling)

The difficult problem is the calculation of the tunnelling matrix element:

$$\begin{aligned} M_{\mu\nu} &= -\frac{\hbar^2}{2m} \int_\Sigma (\Psi_\mu^* \nabla \Psi_\nu - \Psi_\nu \nabla \Psi_\mu^*) \cdot d\vec{S} \\ &= -\frac{\hbar^2}{2m} \int_\Sigma j_{\mu\nu} \cdot d\vec{S} \end{aligned} \tag{3.15}$$

with:
- Σ : separation plane between tip and sample surface
- $j_{\mu\nu}$: current density

The wave functions of tip Ψ_μ and sample surface Ψ_ν have to be known explicitly to calculate $M_{\mu\nu}$. As the exact atomic configuration of the tip is generally unknown in STM experiments, a model tip wave function has to be used.

J. Tersoff and D. R. Hamann [59], who first applied the transfer-Hamiltonian approach to STM in 1983, considered the problem within the following limits:

- tip with local spherical geometry (Fig. 3.3c)

- just the first tip atom contributes to tunnelling
- tip density of states is constant: $\rho_T = \text{const.}$
- s-type tip wave function
- low temperature
- small applied bias voltage

They obtained:

$$I_T \propto V \rho_T(E_F) e^{2\kappa R} \rho_S(\vec{r}_0, E_F) \tag{3.16}$$

with:

$$\begin{aligned} \kappa &= \frac{\sqrt{2m\phi}}{\hbar} : \text{ decay rate} \\ \phi &: \text{ effective local potential barrier height} \\ R &: \text{ effective tip radius} \\ \vec{r}_0 &: \text{ centre of curvature of the tip} \\ E_F &: \text{ Fermi energy} \\ \rho_T(E_F) &: \text{ tip density of states at Fermi level} \\ \rho_S(\vec{r}_0, E_F) &= \sum_\nu |\Psi_\nu(\vec{r}_0)|^2 \delta(E_\nu - E_F) \\ &: \text{ surface LDOS at } E_F \text{ evaluated at } \vec{r}_0 \end{aligned}$$

The exponential decay of the wave functions in z-direction (into the vacuum barrier)

$$\Psi_\nu(\vec{r}) \propto e^{-\kappa z}$$

leads to

$$I_T \propto |\Psi_\nu(\vec{r}_0)|^2 \propto e^{-2\kappa(d+R)} \tag{3.17}$$

with:

$$d : \text{distance between tip and sample surface} \tag{3.18}$$

and the tunnelling current, as expected, depends exponentially on the tip sample distance d:

$$I_T \propto e^{-2\kappa d} \tag{3.19}$$

Considering a finite applied bias voltage leads to an energy and voltage dependence of the decay rate κ via the voltage dependence of the local potential barrier height $\Phi(V)$.

3.2.4 Sample properties derivable by STM

Making use of the expression for the tunnelling current derived in section 3.2.3, several properties of the sample are accessible by STM.

$$\begin{aligned} \mathrm{I_T}(V,\vec{r}) &\propto V\rho_\mathrm{T}(\mathrm{E_F})e^{2\kappa \mathrm{R}}\rho_\mathrm{S}(\vec{r_0},\mathrm{E_F}) \qquad (3.20)\\ &\propto e^{-2\kappa \mathrm{d}} \end{aligned}$$

$$\text{with:}\quad \kappa = \frac{\sqrt{2\mathrm{m}\phi(V,\vec{r})}}{\hbar} \qquad (3.21)$$

1. **Relative tip height:** Due to the extreme sensitivity of the tunnelling current on the distance between tip and sample, height profiles of the surface are an obvious choice for STM measurements.

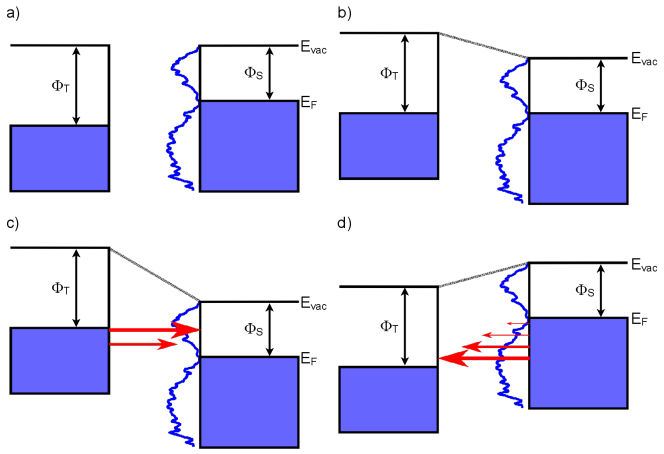

Figure 3.4: *Relative energetic positions of sample and tip states:*
(a) Tip and sample are independent.
(b) Tip and sample are in equilibrium with aligned Fermi levels, separated by a small vacuum gap.
(c) Positive sample bias voltage: Electrons tunnel from tip to sample.
(d) Negative sample bias voltage: Electrons tunnel from sample into tip.
Sketch on the basis of [60].

2. **Sample LDOS:** According to equation 3.20, the tunnelling current is proportional to the sample LDOS at E_F. But in the case of higher applied voltages or non-linear energy band dispersions, for example at semiconductor surfaces, the tunnelling current is rather proportional to the sum of all sample states between E_F and the state eV_{bias}, addressed by the applied sample bias voltage.

   Figure 3.4 shows energy level diagrams for sample and tip. In equilibrium, the Fermi levels align at close distance (Fig. 3.4b). A bias voltage applied to the sample results in a rigid shift of the energy levels of the sample by an amount $|eV_{bias}|$. Electrons tunnel from filled tip states into unoccupied sample states at positive bias voltage (Fig. 3.4c) and vice versa for negative sample bias voltage (Fig. 3.4d). LDOS(V) at constant x, y, and z may be obtained either directly via Lock-In spectroscopy or by taking I(V)-spectra and deriving dI/dV.

3. **Apparent barrier height (ABH):** The assumption, that the local potential barrier height ϕ is independent of the lateral position (x,y) and band structure effects, is not valid in the microscopic limit of atomic resolution and in tunnelling experiments on semiconductors. The local apparent barrier height (ABH) is usually defined by:

$$\phi_A = \frac{\hbar^2}{8m}\left(\frac{d\ln I_t}{d\Delta z}\right)^2 \approx 0.95\left(\frac{d\ln I_t}{d\Delta z}\right)^2 \tag{3.22}$$

   According to Wiesendanger [23], the parallel component of the wave vector, $k_{\|}$, increases the apparent barrier height:

$$\phi_A = \phi_0 + \frac{\hbar^2}{2m}k_{\|}^2 \tag{3.23}$$

   with: ϕ_A : apparent barrier height
   ϕ_0 : average work function of sample surface and tip $\frac{(\phi_S+\phi_T)}{2}$

   Chemical variations of the surface lead to macroscopic variations of $\phi_S(x,y)$ while in the microscopic quantum-mechanical limit the measured ABH should be interpreted as decay rate of the wave functions describing sample surface and tip [23].

3.3 Experimental set-up

In this section, the different elements necessary for STM experiments on Si(111)-2×1 are explained. At first, the preparation processes of tip and sample are lined out, then the experimental set-up including STM chamber, electronic set-up, and data-acquisition processes are explicated.

3.3.1 Tip preparation

It is essential for STM measurements to have well-defined, sharp, and stable tips. This is especially important for spectroscopic measurements which strain the tip stability due to the high variations in sample bias voltage and tunnelling current. Additionally, these measurements often take several hours for one map, and during this time, no tip change may occur to guarantee the comparability of all spectra of the map.

For measurements in this thesis, electro-chemically etched tungsten (W) tips are used. The tips are further prepared under ultra-high vacuum (UHV) conditions and transferred into the STM without breaking the vacuum. A detailed description of the tip preparation process used in Göttingen is given by H. Schleiermacher [61].

1. In the first step, a poly-crystalline, 250 μm thick W wire is electro-chemically etched (anodic oxidation) in the 'drop-off' technique to gain short, sharp tips (Fig. 3.5a). After fastening the W wire to the tip holder, the lower part of the W wire is immersed in potassium hydroxide (KOH) base. The electro-chemical etching process is started by applying a voltage. The cathode is a PtIr spiral, the anode is the W wire. The electro-chemical process may be described by [62]:

$$W + 2OH^- + 2H_2O \longmapsto WO_4^{2-} + 3H_2$$

   The reaction mainly takes place where the wire touches the surface of the solution as sinking tungsten oxide (WO_4^{2-}) screens the lower part of the wire. When the lower part of the wire drops down, etching is finished, and the resulting tip is controlled by an optical microscope to ensure correct length and at least minimum sharpness.

2. The next steps take place in the tip preparation shuttle (Fig. 3.5b) under UHV conditions at a base pressure of about $5 \cdot 10^{-10}$ mbar. The second

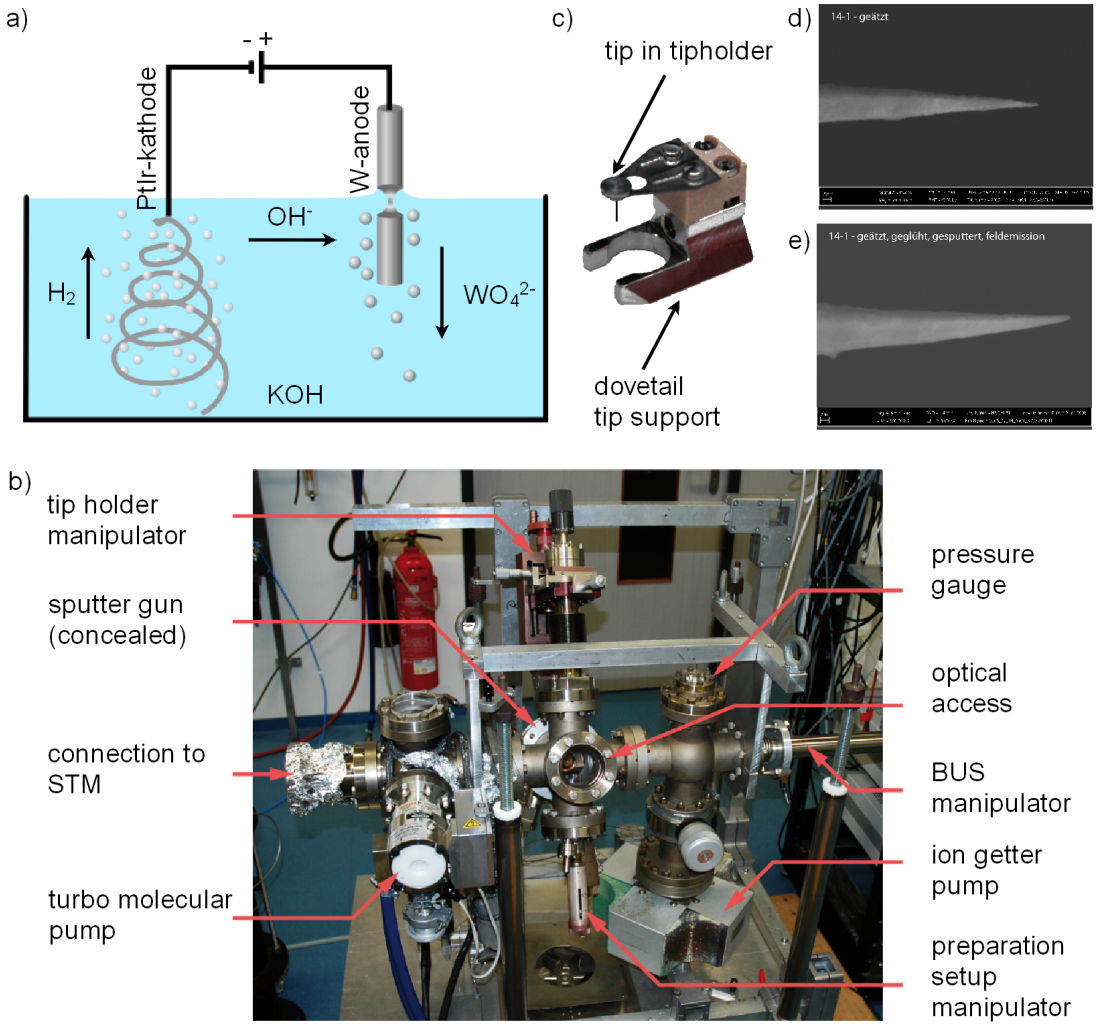

Figure 3.5: *(a) Sketch of etching process: Tungsten oxide falls down directly at the W-wire, hydrogen (H_2) rises at the platinum-iridium (PtIr)-cathode.*
(b) Tip preparation shuttle [28].
(c) Tip holder in dovetail support, ready for transfer into UHV [61].
(d+e) SEM images of tip before (d) and after (e) UHV preparation [61].

procedure is heating the tip resistively until it glows orange. Although this leads to a blunter tip apex, this step is necessary to remove oxide.

3. The third process is sputtering the apex of the tip with argon ions. Loose atoms and clusters, which cause lower stability, are removed, and the tip is sharpened.

4. The last operation is a control via field emission. The slope of the corresponding I(V)-curves gives a clue to the sharpness of the tip, and the high

applied field induces changes in unstable tip configurations, hopefully leading to more stable tips.

After tip preparation is finished, the tips are transferred into the STM chamber and stored there until being mounted into the STM.

3.3.2 Sample preparation

Measurement of cleaved Si(111)-2×1 surfaces at low temperature requires $(\bar{2}11)$ or $(0\bar{1}1)$ oriented wafers with a very high doping concentration (N_D) of about $5 \cdot 10^{18}\text{cm}^{-3}$ to prevent a freeze-out of the sample conductivity. As it is nearly impossible to purchase commercial silicon wafers in these orientations and doping concentrations, all samples for this work are cut from a silicon single crystal. $[\bar{2}11]$- and $[0\bar{1}1]$-direction of the $6 \cdot 10^{18}\text{cm}^{-3}$ phosphor doted silicon single crystal bought from Wacker-Chemietronik were determined by X-ray diffraction in the work of J. Garleff [63].

With a diamond wire saw, wafers in $(\bar{2}11)$ and $(0\bar{1}1)$ orientation are sliced from the crystal, cut to samples with a size of $4\times8\times0.3\,\text{mm}^3$, and a slit for defined cleaving of the samples is applied. Afterwards, the samples are thinned mechanically from 300 μm to approximately 100 μm and polished with 0.25 μm-diamond paste. Figure 3.6b shows the geometry of the finished sample.

Ohmic contacts on the sample are applied with an aluminium-gallium alloy. Additionally, contact to the sample holder is strengthened by a small amount of indium between sample and clamps. A copper block steadies the sample during cleavage (Fig. 3.6a).

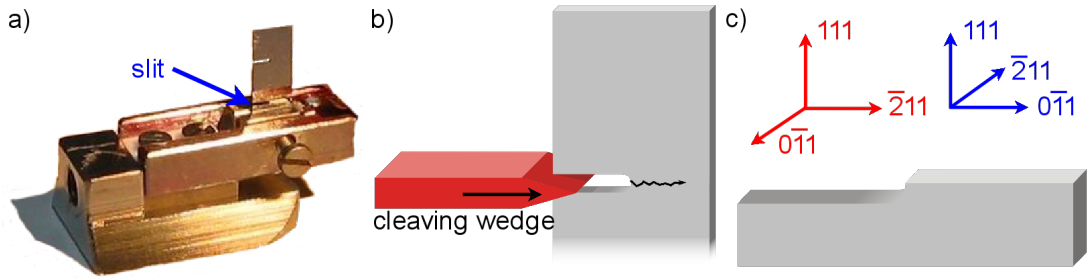

Figure 3.6: *(a) Sample mounted in sample holder [28].*
(b) Sample geometry for cleavage with wedge [28].
(c) Cleaved sample [28]. Red and blue arrow sets indicate crystal directions for cleavage in $(\bar{2}11)$- and $(0\bar{1}1)$-direction.

Directly before the first measurement, the sample is cleaved with the help of a tungsten-carbide splitting wedge in the storage BUS of the STM chamber at room temperature and a base pressure lower than $5 \cdot 10^{-11}$ mbar. The cleaved sample is transferred at once into the cold STM (5.6 K).

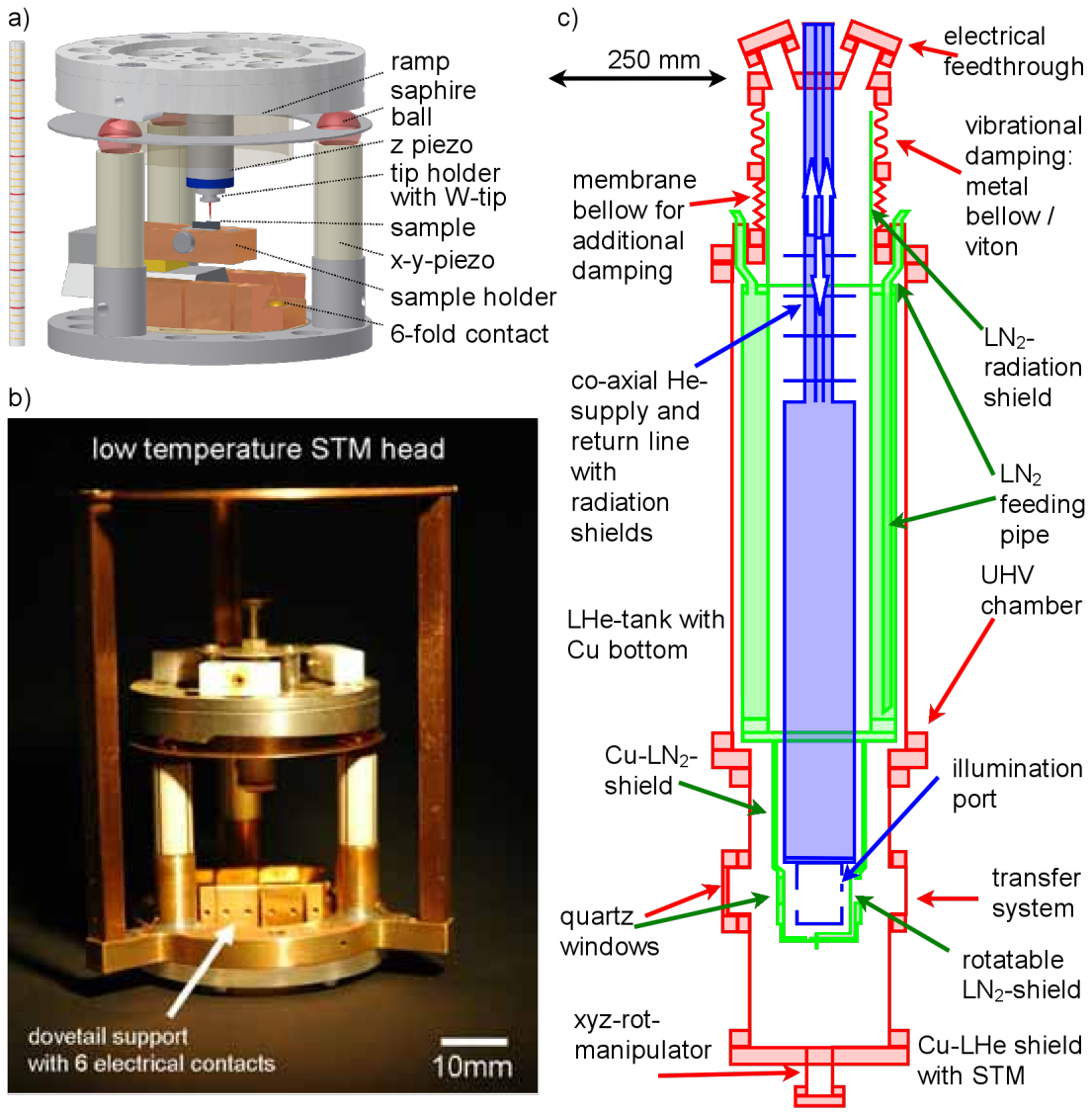

Figure 3.7: *(a) Schematic view of Beetle STM head [64].*
(b) STM head of the cryogenic STM-setup [65].
(c) Schematic drawing of the cryogenic part of the STM chamber [66].

3.3.3 STM set-up

Measurements are performed with a home-built [66] Beetle-type STM (Fig. 3.7a+b) [67]. Coarse movement is realised with three segmented tubular piezos in slip-stick mode enabling x- and y-ranges of about 3 mm and a z-range of 1.5 mm via rotating the ramp of the scan head. Thus, all areas of a sample may be examined. View ports allow optical access to the STM which is crucial for tip approach onto a cleaved sample. A cernox sensor is placed near the sample support to control the temperatures of sample and tip which are assumed to be equal.

Figure 3.3.3c shows a schematic drawing of the cryogenic system of the STM chamber. The STM is coupled to a liquid helium (LHe) bath cryostat (blue) with a filling volume of 4 l. The LHe cryostat is shielded by a surrounding liquid nitrogen (LN_2) cryostat (green). This enables measurements at 5.6 K for a time of 20 hours before LHe and LN_2 have to be refilled.

Isolation from vibrations is realised by mounting the LHe-cryostat with the STM as a spring suspended pendulum. Coupling to the LN_2-cryostat and the UHV-chamber is viton-dampened. The whole UHV-chamber is placed on pneumatic vibration isolators on a separate foundation, effectively decoupling the STM from vibrations of the surrounding building. Soundproof walls hold back most noise from beyond the STM laboratory.

3.3.4 STM electronic

The inset in figure 3.8 sketches the wiring of the tunnelling contact. The sample bias voltage (V_{bias}) is applied to the sample with reference to ground and the tip is grounded. The tunnelling current (I_t) is measured between tip and ground.

The control of the STM (Fig. 3.8) consists of:

- PC with the control program 'Göttinger STM Tool for Measurements' ('GoeSTM') and in- and output card (I/O-card)
- two external digital signal processor (DSP) boards for feedback loop and lock-in measurements, each with a special program
- electronic rack unit with digital analogous converters (DACs) and analogous digital converters (ADCs), a high voltage amplifier, and a control for the piezos

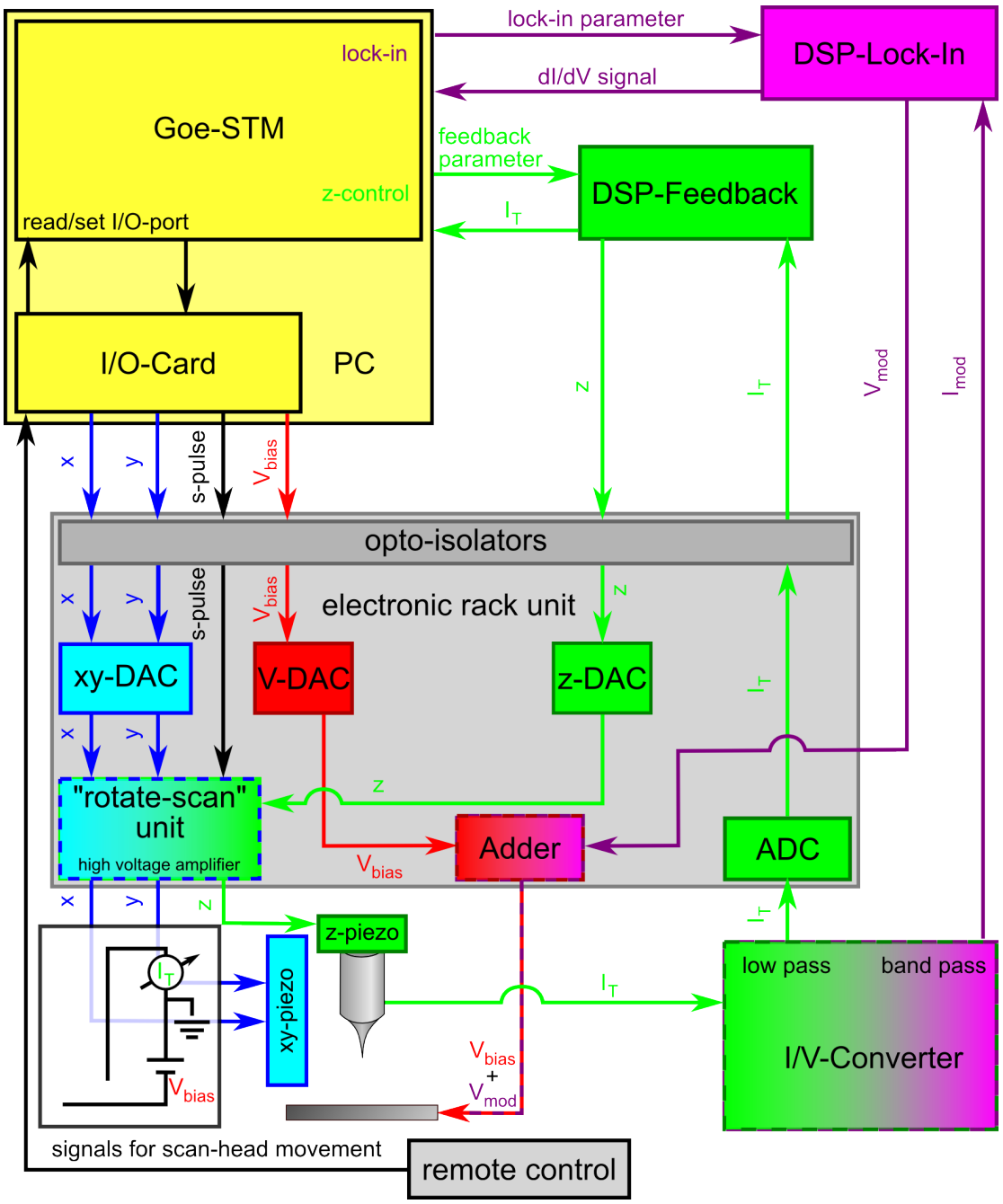

Figure 3.8: *Electronic setup: PC (yellow), electronic rack unit (grey), feedback loop (green), V_{bias} (red), xy-piezo control (blue), and lock-in unit (violet) - Inset: wiring of the tunnel contact*

- IU-converter and bandpass directly at the current feed-through of the STM-chamber

All signals between PC and STM are separated galvanically by opto-isolators to avoid ground loops and other problems due to current flows caused by the ground of circles being on different potentials. The signals at the STM side are grounded via the ion-getter-pump of the UHV-chamber, at the other side of the opto-isolators the reference point for signals is the PC ground.

All settings for the measurements are done in 'GoeSTM'. Everything concerning feedback loop, tunnelling current or tip height adjustments (marked green in Fig 3.8) is controlled by $DSP_{feedback}$. The program running on $DSP_{feedback}$ controls the tip height via a z-signal which is converted into a high voltage and applied to the z-piezo by the electronic rack unit. The tunnelling current is recorded, and in the case of an active feedback loop the z-signal is adjusted. Values for z and I_t are read out by 'GoeSTM'.

The signal for V_{bias} (red in Fig 3.8) is set by 'GoeSTM', sent to the electronic rack unit via I/O-card, converted into a voltage by V-DAC, and applied to the sample. During lock-in mode (violet in Fig. 3.8), $DSP_{lock-in}$ generates a sine voltage signal according to the parameters set by 'GoeSTM'. This signal is added to V_{bias} in the electronic rack unit. The resulting high frequency variation of I_t is separated from I_t by the bandpass and fed to $DSP_{lock-in}$. Here, total amplitude, sine, and cosine of the dI/dV-signal are calculated and sent to 'GoeSTM'.

The signals for x- and y-movement are sent via I/O-card to the electronic rack unit where they are converted to high voltages. These voltages are applied to the piezo segments by the 'rotate-scan' unit according to the geometry of the STM and to the movement mode (rotate or scan).

3.3.5 Data acquisition modes and interpretation of the measured quantities

During the work for this thesis, the old, Linux-based data acquisition program 'stm-mess' was replaced by a new program for data acquisition in order to run on modern computers and with Windows XP^{TM}. This was caused by the necessity to renew the computer hardware and, more important, the need for more flexibility in data acquisition and also for new measurement modes. We developed the data acquisition program 'GoeSTM' which not only offers new measurement methods, as for example voltage dependent determination of the ABH, but also enables flexible combination of measurement modes, set points, resolutions, and areas of data acquisition in one project.

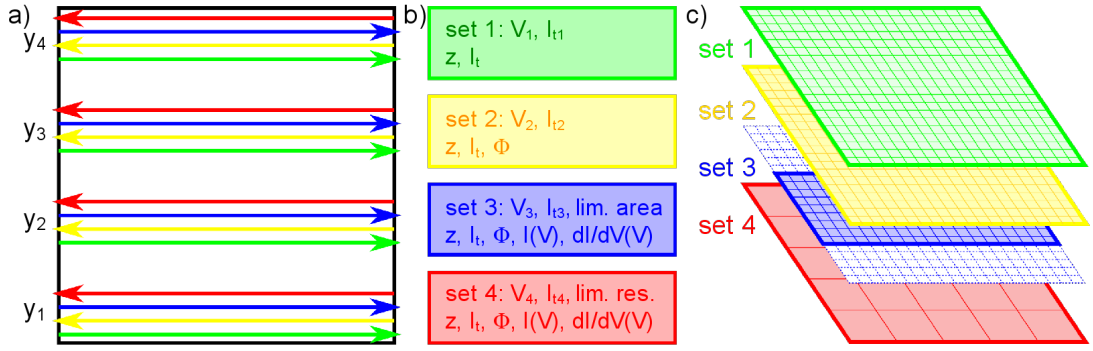

Figure 3.9: *Quasi-simultaneous data acquisition with four data sets: (a) every line is scanned four times; (b) examples of different parameters for data sets; (c) pixel, where data acquisition takes place: set 1 (green) and 2 (yellow) – at every pixel, set 3 (blue) – in a limited area, and set 4 (red) – with a limited resolution.*

In general, data acquisition with 'GoeSTM' is based on so-called data acquisition sets which are measured quasi-simultaneously. All sets of one measurement have the same scanspeed, scanangle, and basic x- and y-offset, scansize, and resolution. During measurement, each scanline is scanned multiple times according to the number of data acquisition sets. For example, in a measurement containing four sets two trace-retrace scans are run (Fig. 3.9a). In trace 1 all measurements included in set 1 are performed, during retrace 1 the measurements for set 2 are executed, and so on. Only after all measurements for all sets are finished, the scanner moves to the next line.

As the drift of the measurement system is negligible for the (short) time scale on which all measurements in one scanline are performed, all data sets in trace direction are taken at the same position with high precision. The same is true for all retrace data sets, while a direct comparison of trace and retrace data sets is more complicated due to a small shift.

Several parameters are unique for each data set. The first pair are setpoint current and sample bias voltage which determine the vertical tip position for all measurements of the set.

The second is the assortment of measurements which are performed at each pixel of the data set (Fig. 3.9b).

The last group are the actual scansize, position, and resolution of the data set. In order to reduce measurement time and amount of data for more extensive data acquisition modes without losing detailed topographic information, it is possible to limit the data acquisition of a set with such extensive modes while performing the detailed topographic measurements in another data set. There

are two possibilities to limit data acquisition. Either the area is limited (e.g. measurements for this set are performed only in line 100 to 150 of 256, the same for pixel in x-direction – blue set in Fig. 3.9c) or the resolution of of this data set is reduced (e.g. measurements only take place in every third pixel in x-direction and every third line in y-direction – red set in Fig. 3.9c).

In practice, an STM measurement takes place in the following way: At the beginning of each line, the setpoint is adjusted for the corresponding data set. At each pixel of the scan line, all measurements activated for this data set are performed or skipped according to the settings for limited data acquisition. At the end of each line a query, whether there is a further data set, is sent. Only if that is not the case, the scanner moves on to the next scan line and starts data acquisition for the first set.

There is a wide variety of measurement modes ranging from simple topography and current maps over I(V)- and dI/dV-maps to measurements with applied cross voltage and potentiometry. I will only go into detail explaining measurement modes utilised in this thesis. Topography and current data are always recorded, all other modes may be activated as required.

- **Topography map:** As all scans are performed in constant current mode, the topography contains the relative tip height necessary to achieve a constant current at each position. This tip height results from a combination of the actual height profile of the sample surface (atomic corrugation, surface steps, adsorbates) and the integrated LDOS.

  At high positive and negative voltages ($\sim \pm 2\,\mathrm{V}$ for silicon), bulk states dominate the integrated LDOS. These are approximately homogeneous at the tip position. Thus, the tip height represents mainly the height structure of the surface. At lower voltages, addressing states within the bulk band gap, surface and defect states dominate the integrated LDOS. These states are highly localised, and the relative tip height is strongly influenced by the electronic structure of the sample surface.

- **Current map:** In constant current mode, the current map is mainly an instrument to control the adjustment of feedback parameters and inherent noise. Deviations from setpoint current should only occur at abrupt, large height variations.

- **I(V)- and dI/dV-maps:** I(V)-curves are taken at each pixel of the data set, dI/dV-curves may be gained either by numerically deriving the I(V)-spectra or, in order to reduce noise and effects of systematic errors, via a digital Lock-In measurement at each voltage step of the I(V)-measurement

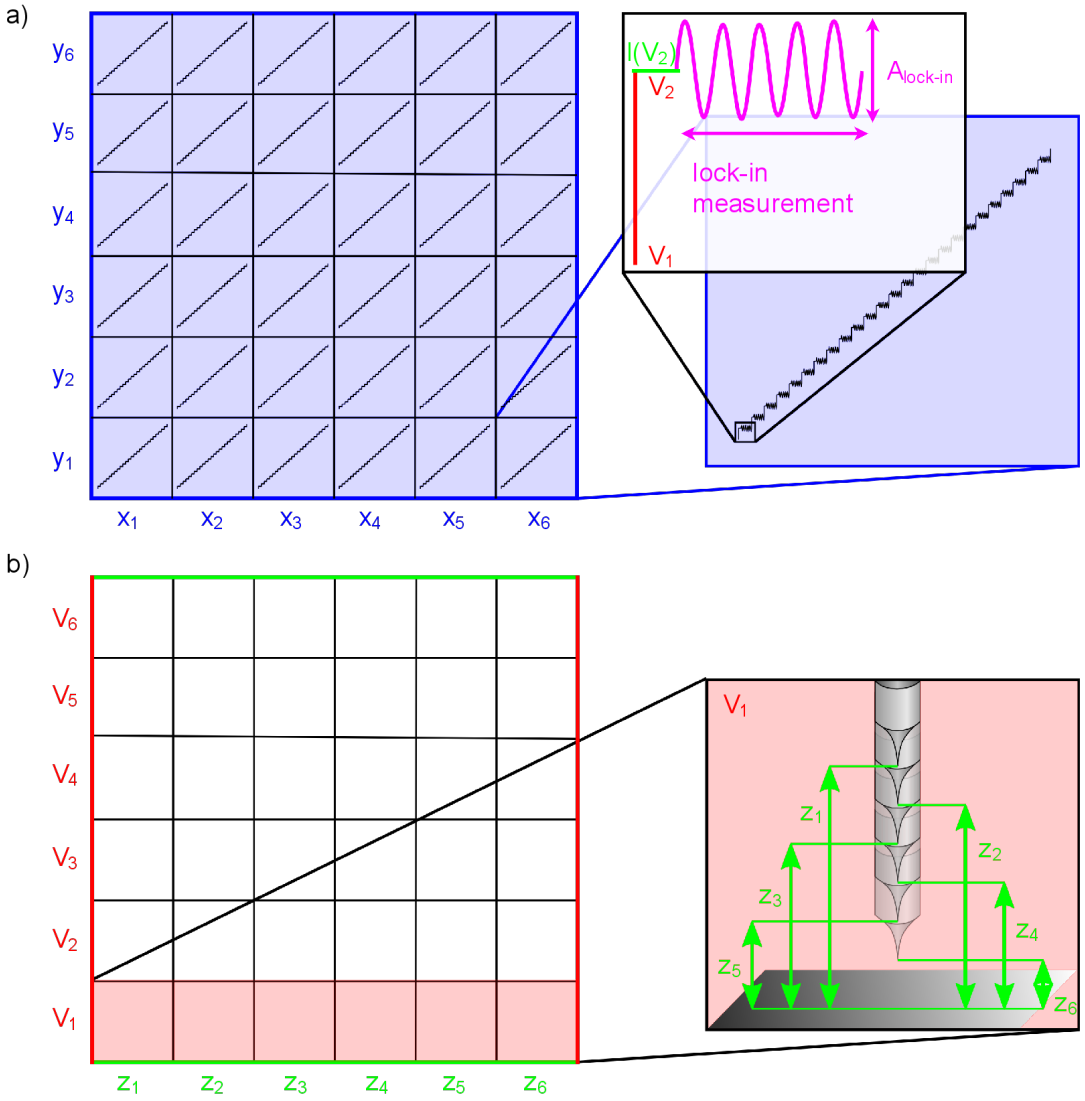

Figure 3.10: *(a) Lock-in measurement: At every x-y-position a voltage ramp is set via equal, small steps. Each step consists of setting the new voltage (V_2), read out $I_T(V_2)$, and performing the lock-in measurement with modulation amplitude $A_{lock-in}$.*
(b) I(z,V) measurement: At every voltage value the tip moves toward the sample in small, equal steps, and $I_T(z_i)$ is recorded.

(Fig. 3.10a). The results are four-dimensional (4D) data sets I(V,x,y) or dI/dV(V,x,y). A multitude of different information may be extracted from these 4D-data sets by keeping one or two parameters constant. Constant voltage results in current imaging tunnelling spectroscopy (CITS) and dI/dV-maps, single I(V) and dI/dV-spectra are obtained by holding x and y constant, and spatial variations of the electronic structure are visualised

by plotting I(V) or dI/dV along a line in (x,y)-plane (called spatial profile of the dI/dV(x,y,V) data set).

Note that in order to obtain LDOS the dI/dV-spectra have to be 'topography normalised' (for details see J. Garleff [68]). For this process it is necessary to know the ABH.

- **Apparent barrier height (ABH):** On the basis of equation 3.22, the displacement of the tip by Δz and measurement of I(z_1) and I($z_1 - \Delta z$) allows the calculation of the ABH:

$$\phi[\mathrm{eV}] = 9.5 \cdot 10^{-21} \left(\frac{\ln \frac{\mathrm{I}(z_1)}{\mathrm{I}(z_1 - \Delta z)}}{\Delta z} \right)^2 . \tag{3.24}$$

Apparent barrier height maps show variations in the sample work function due to chemical differences in the surface. In addition, the values for the local ABH are utilised to get the LDOS from dI/dV-spectra. In the case of an approximately constant ABH, an averaged value is sufficient.

In addition to the measurement of these maps, local measurements at exact positions are performed. Here the noise factor may be significantly reduced by averaging over multiple single measurements. Local measurements are implemented for ABH, I(V), and dI/dV mode. There is one further mode only available in local measurement, this is I(V,z) mode.

- **local I(V,z)-spectroscopy:** The tunnelling current is recorded for a 'map' of varying tip heights and sample bias voltages. At every step of the voltage slope, the setpoint is adjusted, 'sample and hold' mode is activated, and the voltage according to the voltage step is applied. Then the tip is moved within a defined z-range, and the current is measured. This procedure is repeated until the I(V,z) data set is complete (Fig. 3.10b).

  Applying an algorithm for calculating the ABH in a voltage and z dependent image allows comparison of the decay rates of the wave functions for conduction and valence band states and for bulk, surface, and gap states.

Chapter 4

Positive and negative buckling

In this chapter, the influence of the buckling of the Si(111)-2×1 surface on the electronic structure is studied. The multitude of domain boundaries is utilised to identify differently buckled domains. I(V)-measurements with high spatial and energetic resolution show the electronic structures of the two buckling types. The spatial resolution provides insight into the crossover from one buckling type to the other at the domain boundaries. The different band gaps and the position of the surface bands in the band gap of the bulk silicon and relative to each other are determined. The experimental results are compared to *ab initio* calculations by M. Rohlfing and M. Pötter. The geometry based method of recognising differently buckled domains and the room temperature studies of the electronic structure have been treated by T. Spaeth during his diploma thesis [28]. The main results of this topic were published in PRB in 2012 [31] (see also for details on the calculations).

4.1 How to recognise differently buckled domains?

Here, domain boundaries are used to determine whether two adjacent domains are buckled differently or likewise. In STM measurements at room temperature as well as at 6 K domains of positively buckled π-bonded chains are found as well as domains with negative buckling on multi-domain Si(111)-2×1 surfaces.

Close examination of type III domain boundaries in STM measurements at room temperature and at 6K reveals π-bonded chains meeting with different displacements of the up-atoms (Fig. 4.1). The displacement of the up-atoms of a π-bonded chain in one domain relative to the two neighbouring π-bonded chains in the second domain is compared. In many cases, the distance is the same to both adjacent π-bonded chains which means that the up-atoms are displaced by exactly half a 2×1-unit cell (Fig. 4.1a).

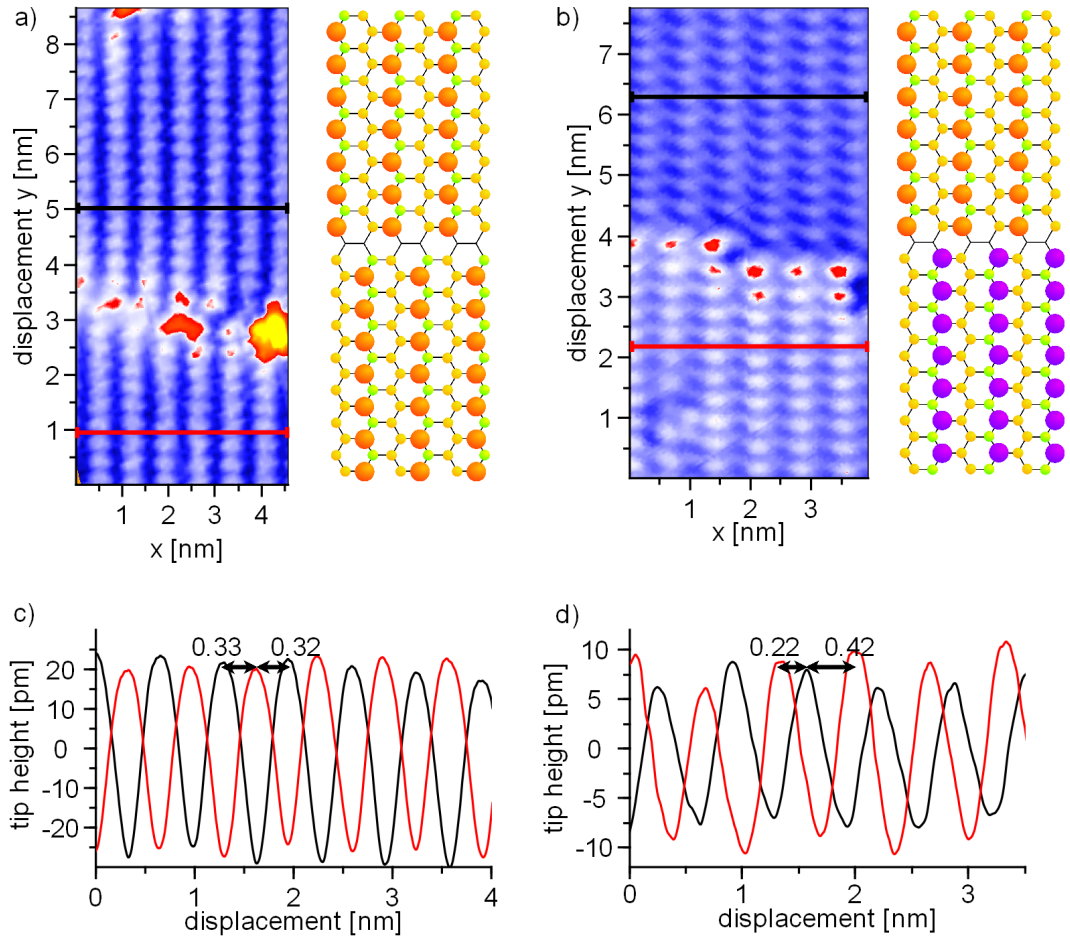

Figure 4.1: *(a+b) Topography images of type III domain boundary separating two domains with same (a) and with different (b) buckling types [V_{bias} = -1 V; I_t = 0.1 nA; T = 300 K]. At the right side of the images the respective surface models are illustrated - big red circles: up-atoms (positive buckling), big violet circles: up-atoms (negative buckling), green circles: down-atoms, yellow circles: atoms of lower chain.*
(c+d) Averaged height profiles of upper (black) and domain lower (red) (see corresponding lines in topography images (a+b)).

But there are also type III domain boundaries where the displacement to one neighbouring chain is twice as much as to the neighbouring π-bonded chain on the other side. While the centred meeting up-atoms can be easily explained by a model with only one buckling type in both domains (Fig. 4.1a+c) another model must be taken into account to describe the π-bonded chains meeting with the up-atoms in the distance relation of 0.42 nm vs. 0.22 nm. By assuming that the π-bonded chains in one domain are buckled positively while the other domain consists of negatively buckled π-bonded chains, this distance relation of 0.42 nm vs. 0.22 nm can be explained perfectly (Fig. 4.1b+d). DFT-optimised structures

yield 0.447 nm and 0.218 nm for these spatial offset values [31]. In this way, it is possible to see in the topography measurement whether two domains are buckled likewise or differently. The actual buckling type may not be determined by these considerations. All positions visible in Fig. 4.1b would be the same for a structure with swapped buckling types. For a definite determination of the buckling type the electronic structure must be considered.

4.2 Comparative study of the electronic structure

The electronic structure of differently buckled domains is studied with high spatial and energetic resolution. This allows the determination not only of the band gaps of the two buckling types but also of the crossover between the two buckling types at domain boundaries, parallel and perpendicular to the chains. *Ab initio* calculations of the band structure for both buckling types [31] are used for comparison with the experimental results.

CITS maps of multi-domain areas of the Si(111)-2×1 surface reveal differences in the electronic structure of differently buckled domains (Fig. 4.2). Figure 4.2a shows topography data of a large domain with one type of buckling enveloping a smaller domain with the other buckling type. The CITS maps at different voltages display the differing integrated densities of states of the domains. At the setpoint voltage of V_{bias} = -1.0 V all domains as expected show the same tunnelling current (Fig. 4.2b), while at V_{bias} = -0.3 V the small domain displays a much higher tunnelling current due to an increased density of states at this voltage (Fig. 4.2c). This situation is reversed for positive voltages where the surrounding domains have a higher tunnelling current (Fig. 4.2d).

To study these differences in the electronic structure and the crossover between the buckling types in more detail, high-resolution I(V)-measurements of different domain boundaries at 6 K and at room temperature are examined (figures 4.3 and 4.4). The band gaps of the differently buckled domains are determined using single dI/dV spectra. Spatial profiles of the dI/dV(x,y,V) data set, the variations of the band gap E_G, the valence, and the conduction bands along a line in the topography data are revealed. dI/dV data in this chapter is obtained by numerical derivation of I(V) curves. Noise is reduced by averaging over several spectra in x- and y-direction.

Figure 4.3 shows data of a I(V) map taken at 6 K that includes three domains which are separated by a type II domain boundary (between left (p) and right (n_1) side in the upper part of Fig. 4.3a+b) as well as a type III domain boundary (between upper (p and n_1) and lower (n_2) part of Fig. 4.3a+b). In the topography

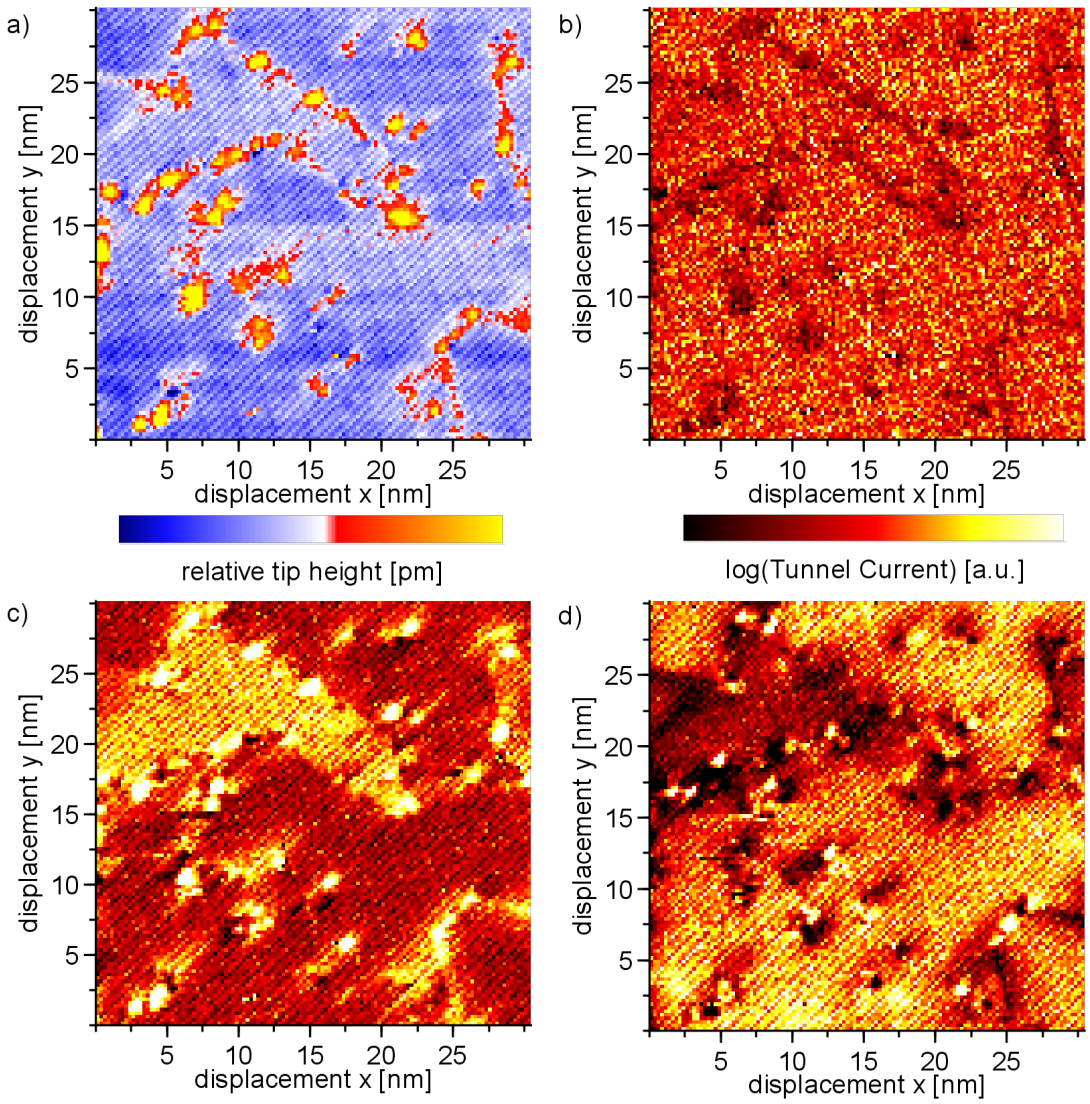

Figure 4.2: *CITS data of multi-domain Si(111)-2×1 surface:*
(a) Topography image [V_{bias} = -1 V ; I_t = 0,15 nA; T = 300 K].
(b-d) Current maps at a voltage of -1.0 V (b), -0.5 V (c), and +1.0 V (d). The contrast is due to different buckling types in the domains. Note that one colour depicts different current values in the individual figures as the current ranges differ a lot between the maps at different voltages.

image (Fig. 4.3a) the type II boundary is visible in a slightly lighter colour of the two π-bonded chains that form the boundary while the type III boundary is visible as bright line cutting the π-bonded chains.

At low temperatures of 6 K the different band gaps are well distinguished, as single dI/dV spectra from the different domains show (Fig. 4.3c). Due to the high negative doping, E_F lies at the lower edge of the SCB for both buckling types

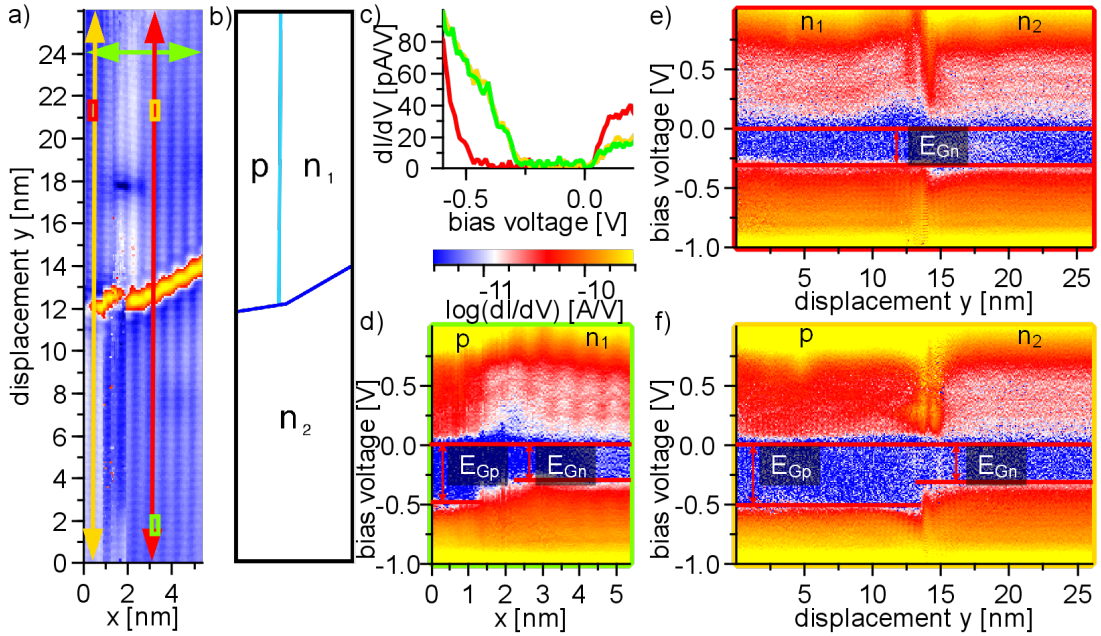

Figure 4.3: *STS data of measurements at 6 K:*
(a) Topography image: Red, yellow, and green boxes mark positions of dI/dV single spectra (c). Red, yellow, and green lines mark positions of spatial profiles of the dI/dV(x,y,V) data set (d-f). [V_{bias} = -1 V; I_t = 0,1 nA; T = 6 K].
(b) Sketch of domains (p: positively buckled domain, n_1 and n_2: negatively buckled domains) and domain boundaries (light blue: type II boundary and dark blue: type III boundary).
(c) Single dI/dV spectra of different domains in (a) – positions marked by coloured boxes: red: positive buckling (p), yellow: negative buckling (n_1), and green: negative buckling (n_2).
(d-f) Spatial profiles of the dI/dV(x,y,V) data set across type III boundary with same (e; red line) / different (f; yellow line) buckling type in the two domains and type II boundary (d; green line). Red lines mark positions of band edges.

in agreement with photo emission studies by Himpsel *et al.* [37]. The band gap of the π-bonded chains with positive buckling has a width of E_{Gp} = 520 (20) mV while the π-bonded chains with negative buckling exhibit a smaller band gap of E_{Gn} = 290 (20) mV. These values are in qualitative agreement with the results by Bussetti *et al.* [6]. The surface band gaps calculated by Pötter and Rohlfing amount to E^t_{Gp} = 750 mV and E^t_{Gn} = 580 mV [31], showing the same band-gap reduction when changing the buckling from positive to negative. Note that measured band gaps are systematically smaller than the calculated ones. In the experiment, the tail of the spectrum makes it difficult to assign absolute values to band positions. Furthermore, the theoretical approach does not consider spectral broadening (and possibly level shifts) from electron-phonon interaction (which might account for 100 meV or more in the present case [69]). Also, the n-type

doping might reduce the absolute size of the gap, which cannot be considered in the present theory.

Figure 4.3e shows a spatial profile of the dI/dV(x,y,V) data set across the type III boundary between the two domains with negative buckling (n_1 and n_2, red line in Fig. 4.3a). Both domains have the same band gap E_{Gn}. The spatial profile of the dI/dV(x,y,V) data set across the type III domain boundary separating two domains of different buckling types (p and n_2, Fig. 4.3f) was taken at the position of the yellow line in Fig. 4.3a. The variation in the dI/dV spectra resembles the band structure of a hetero structure of materials with different band gaps. The domain on the left side has the larger band gap E_{Gp} of π-bonded chains with positive buckling while the right domain shows the significantly smaller band gap E_{Gn} of negative buckling.

The type II boundary (Fig. 4.3d) between domains with different buckling types (p and n_1, green line in Fig. 4.3a) affects only the two π-bonded chains that form the boundary itself while the energetic position of the bands in the neighbouring chain remains undisturbed. This confirms that the interaction between neighbouring π-bonded chains inside a given domain is negligible [41].

The room temperature spectroscopy maps in Fig. 4.4 contain type III domain boundaries, one with two positively buckled domains (Fig. 4.4a+d), the other with both buckling types (Fig. 4.4b+e). The band gaps, extracted from single dI/dV spectra, taken at various sites and samples, differ more than the low temperature results. The band gap for positively buckled domains is larger than for negative buckling. Approximate values are E_{Gp} = 300-400 mV for positively buckled π-bonded chains and E_{Gn} = 200-250 mV for π-bonded chains with negative buckling (Fig. 4.4c).

The spatial profile of the dI/dV(x,y,V) data set across the type III domain boundary separating two positively buckled domains has the larger band gap E_{Gp} in both domains (Fig. 4.4d) while the spatial profile of the dI/dV(x,y,V) data set across the type III boundary with both buckling types looks similar to the one at low temperatures (Fig. 4.4e) with the smaller band gap E_{Gn} in the left domain with negative buckling and E_{Gp} in the positively buckled right domain.

4.2.1 Position of the surface bands

Going a step further in the analysis of single dI/dV spectra gives us access to the exact positions of the surface bands for both buckling types within the bulk band gap (Fig. 4.5a). The determination of the positions is not intuitive

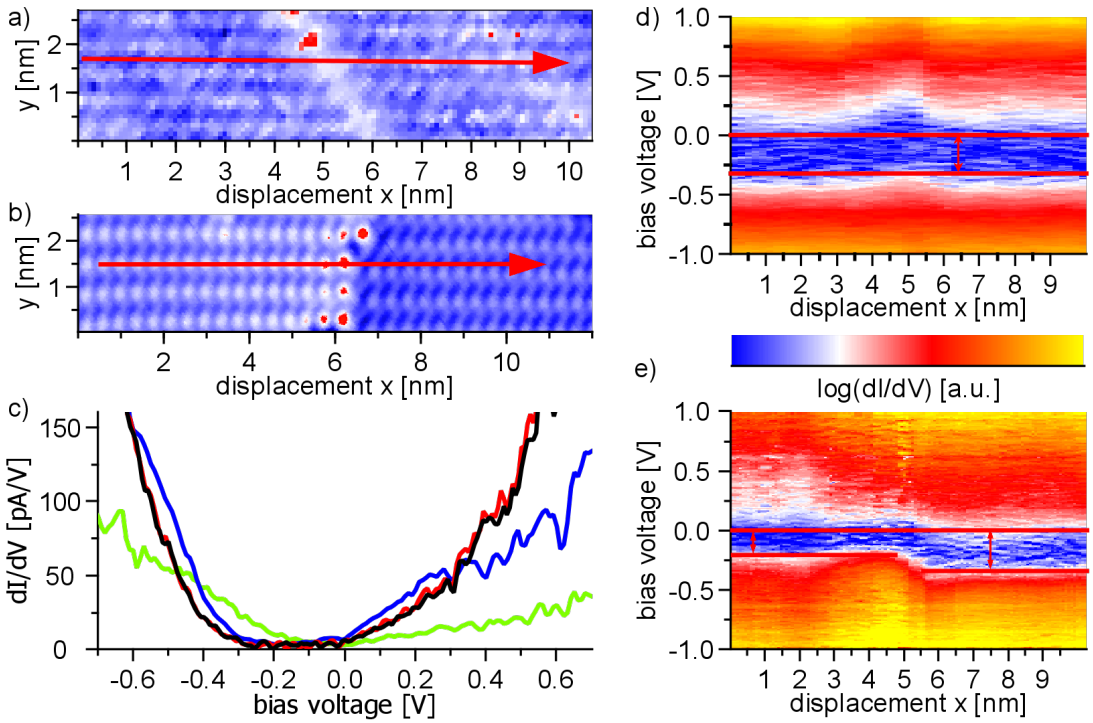

Figure 4.4: *STS data of room temperature measurements:*
(a+b) Topography images across type III domain boundary with same (a) / negative (left side) and positive (right side) (b) buckling type in the two domains. Red line marks position of spatial profiles of the dI/dV(x,y,V) data set (d+e). [V_{bias} = -1 V; I_t = 0.1 nA; T = 300 K].
(c) Single dI/dV spectra of the different domains in (a) and (b): red: left side in (a), black: right side in (a), green: left side in (b), and blue: right side in (b).
(d+e) Spatial profiles of the dI/dV(x,y,V) data set along red lines in (a) and (b). Red lines mark positions of band edges.

because of diverse configurations leading to different energetic positions of the bulk bands in relation to E_F at the surface. We assume that the sample is in equilibrium (const. E_F) and that we can neglect the effect of tip induced band bending. This assumption is supported by I(V) measurements where we find no significant impact of V_{bias} and I_t on the spectroscopic signatures. At first, we describe for one buckling type (e.g. positive buckling) the potential landscape perpendicular to the surface within the rigid band model. For high n-type doping with phosphorus in the bulk, E_F is located in the shallow donor band ∼45 meV below the BCB [38]. At the surface, there is a surface state within the bulk band gap. As explicated in chapter 2.2, the energetic difference between bulk and SCB is different for positive and negative buckling resulting in different Schottky barriers between surface and bulk (Fig. 4.5b+c). In the last step we consider the lateral co-existence of negative and positive buckled areas including the resulting domain boundary. At a large distance from the

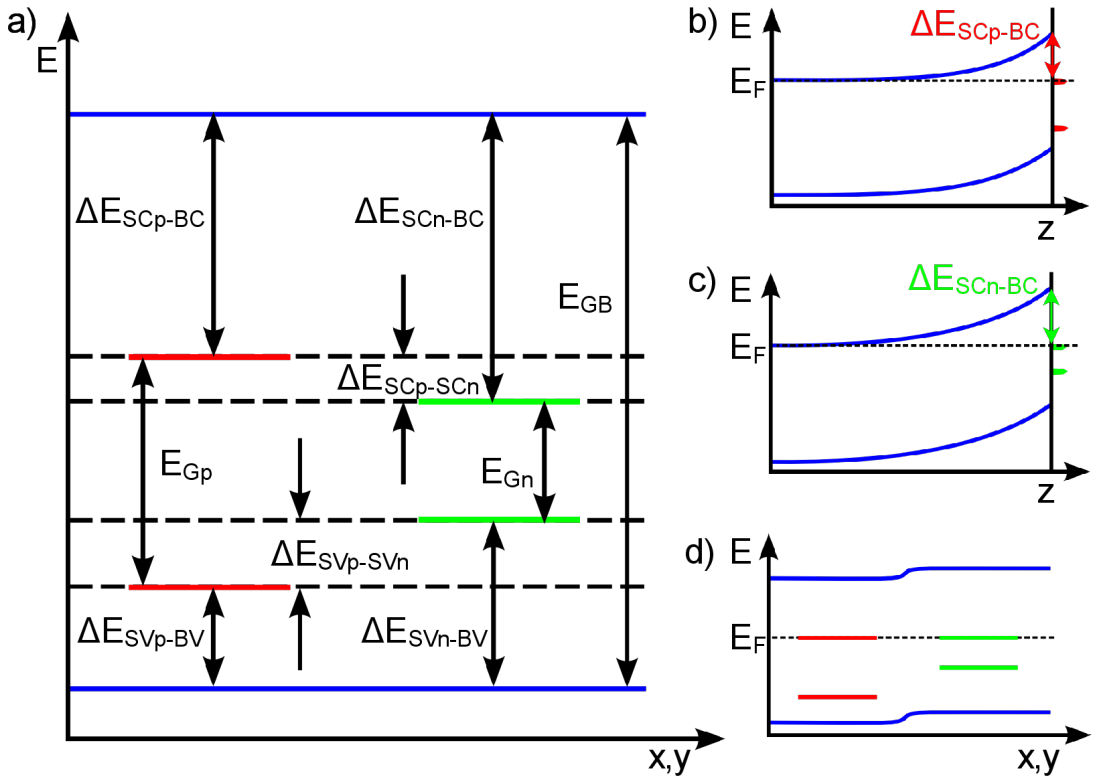

Figure 4.5: *(a)Sketch of the relative energetic positions of bulk and surface bands. (b+c) Band bending of the bulk bands and resulting space charge regions for domains with positive (b) and negative (c) buckling.*
(d) Band positions of bulk bands (blue) and surface bands of positively (red) and negatively (green) buckled π-bonded chains and after the surface conduction bands are aligned.

domain boundary the surface conduction band minima are both close to E_F and the bulk bands at the energetic positions of 0.4 eV (positive buckling) and 0.5 eV (negative buckling) respectively above E_F (Fig. 4.5d). Directly at the boundary position the two electronic systems align similar to contact between two different semiconductors e.g. GaAs/aluminum-arsenide (AlAs) resulting in *surface band offsets* at the boundary line and a three-dimensional (3D) space charge layer in the vicinity. The latter electrostatic problem is defined by the charge distribution in the surface layer and the space charge layer in the bulk. The precise nature of this junction depends on the nature of edge states resulting from broken symmetry at the boundary and perhaps on the 'electron affinity' of the two systems. It is not possible to disentangle the source of the different signatures occurring at a domain boundary on the basis of our measured data, but from Fig.4.3e+f we can define a length scale at which the contact region may

be neglected: At a distance of more than 5 nm apart from the domain boundary there is no significant influence on the electronic structure.

In the following analysis, we use a signature of the bulk bands within our I(V) spectra as reference for all energetic positions. In the voltage regime of our I(V)-measurements between -1.0 V and 1.0 V, we can distinguish different tunnelling channels (Fig. 4.6a). For higher voltages, the main contribution to the tunnelling current comes from the bulk bands (yellow). At small positive voltages the major tunnelling channel is provided by tunnelling into the empty states of the

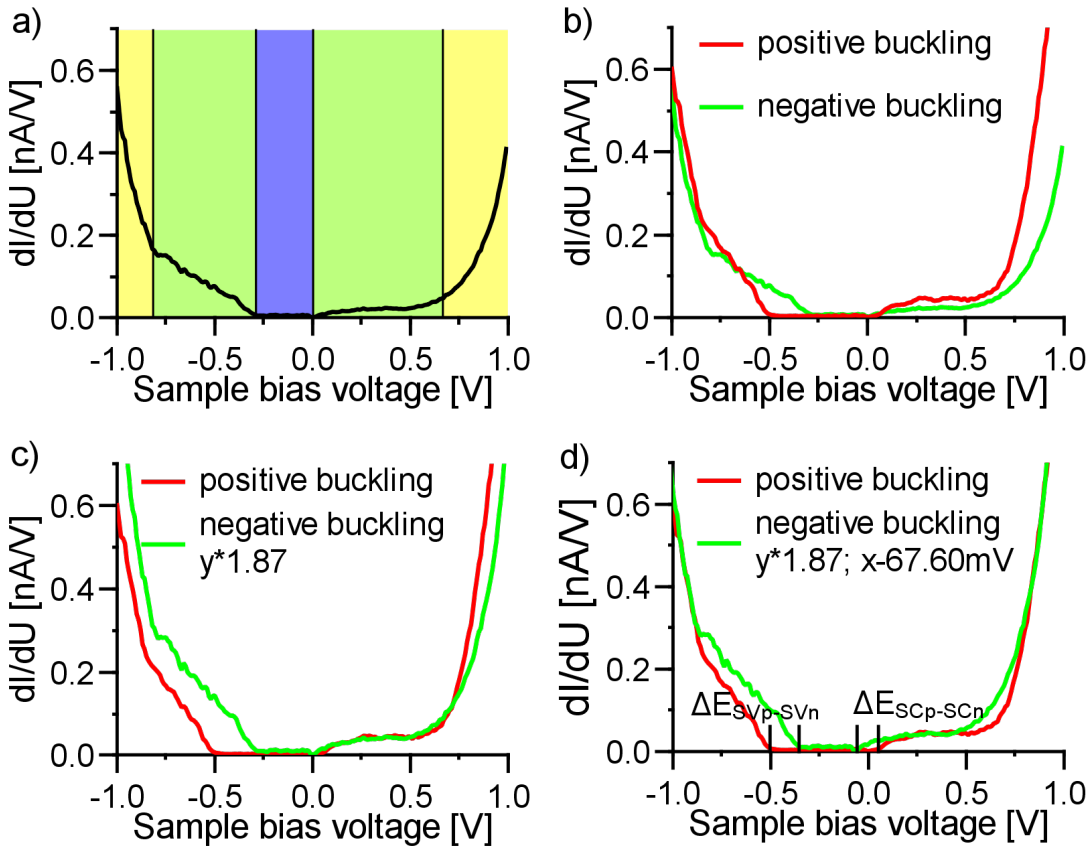

Figure 4.6: *Single dI/dV spectra [T = 6 K]:*
(a) Different major contributions to the tunnelling current I_T: Bulk Valence Band (BVB - yellow), Bulk Conduction Band (BCB - yellow), Surface Valence Band (SVB - green), and Surface Conduction Band (SCB - green). In the Band Gap (BG - blue) there is no tunnelling.
(b-d) Alignment for single dI/dV spectra from positively (red line) and negatively (green line) buckled domains: (b) original spectra, (c) multiplication of y-values with 1.87 for in order to adjust dI/dV-values in surface states, (d) shifting x-values of spectrum from negatively buckled domain by -67.6 meV in order to align the energetic positions of bulk conduction and valence band.

SCB (green). The fraction of tunnelling into the tails of the BCB is very small and adds no distinct signature to the dI/dV spectrum. The situation is similar for negative voltages between the edge of the SCB and higher negative voltages up to -0.8 V. There the main component of tunnelling current stems from tunnelling out of the SVB with only a small part of tunnelling current from the BVB. In the surface band gap (blue) there is only a small amount of tunnelling current due to tunnelling out of the filled states of the SCB.

The fraction of tunnelling current due to tunnelling through the space charge region is negligible [70] but leads to a smoothed onset of current into the BCB instead of a sharp step. In combination with the small density of states (DOS) of the BCB states and the low transmission into them at the edge of the Brillouin zone this leads to masking of the bulk band edges by the surface bands and thus to a seemingly larger gap of the bulk bands. For our analysis this means that we cannot use the edges of the bulk bands as reference. Instead the strong increase in dI/dV signal at higher voltages is considered. In addition, at the setpoint of our measurements (V_{Bias} = -1.0 V; I_T = 0.1 nA) the distance between sample and tip is different for the two buckling types, due to the unequal energetic position of the bulk bands in relation to E_F and the resulting difference in the integrated density of states at the setpoint voltage. To compare the band positions of the different buckling types it is necessary to 'adjust' the spectra.

In the first step, we adjust signal height and energetic position of the dI/dV spectra assuming that the bulk bands are identical for negative and positive buckling (Fig. 4.6b-d). To compensate the differing distances, first the dI/dV values of the curve for negative buckling are multiplied with 1.87 matching the height of the dI/dV signal from the surface states, assuming that the differential conductance of the surface states is independent of the buckling type. The bulk bands have an energetic offset of -67,6 meV between the domains with positive and negative buckling. As we use the bulk bands as reference, we shift the dI/dV spectrum from the negatively buckled domain by this value in order to adjust the bulk bands to the same value.

In the second step, the energetic difference $\Delta E_{SCp-SCn}$ between the onset of the SCB of the negatively buckled π-bonded chains and the onset of the SCB of the positively buckled π-bonded chains is determined. This is done via a visual overlay by shifting the spectrum for negative buckling on the voltage scale until the surface conduction bands of both buckling types overlay exactly. The amount of the shifting needed is $\Delta E_{SCp-SCn}$. This proceeding is more accurate than simple metering because there is no need to determine the exact band edge. The energetic difference $\Delta E_{SVp-SVn}$ between the surface valence bands is determined likewise. We find the surface bands of the π-bonded chains with negative buckling within the band gap of the π-bonded chains with positive buckling with $\Delta E_{SVp-SVn}$ = 129 (10) mV and $\Delta E_{SCp-SCn}$ = 99 (10) mV. These

values are in excellent agreement with the calculations by Pötter and Rohlfing where we get $\Delta E^t_{SVp-SVn}$ = 87 mV and $\Delta E^t_{SCp-SCn}$ = 85 mV [31]. While these values can be determined with high precision, the determination of the exact position of the surface bands within the bulk band gap is less exact. This is due to the fact that the band edges of the bulk bands are concealed by the surface bands, and that the onset of tunnelling into the bulk bands is smoothed. Extrapolating the course of the bulk bands in the concealed part, we get an apparent band gap of 1.21 eV which is slightly larger than the literature value E_{GB} = 1.17 eV at 6 K [71]. We extract ΔE_{SVp-BV} = 0.21 eV and ΔE_{SCp-BC} = 0.51 eV from our experimental data for positive buckling. The calculated values ΔE^t_{SVp-BV} = 0.0 eV and ΔE^t_{SCp-BC} = 0.4 eV(E^t_{SV} = 0.0 eV, E^t_{SC} = 0.75 eV, and E^t_{BC} = 1.1 eV) differ significantly from the experimental data [31]. This corresponds to the differences in the surface band gaps, which our experiments yield systematically smaller than found in theory. As mentioned before, this might result from experimental difficulties in determining the center-of-mass of a band energy, from neglect of electron-phonon interaction in our theory, or from n-type doping. Note that the mid-gap energy of 0.36 eV (from our experiment) agrees very well with the calculated mid-gap energy of 0.38 eV.

4.3 Apparent Barrier Height

In this section, I(z,V) measurements and the resulting, voltage dependent ABH(z,V) plots are compared for π-bonded chains with positive and negative buckling. Figure 4.7 presents the results of I(z,V) measurements in two differently buckled domains. Figure 4.7a shows a topography image of two differently buckled domains (left side – positive, right side – negative) separated by a type IV domain boundary without displacement of the chains at the domain boundary, in contrast to the type III boundaries investigated in section 4.1. This kind of domain boundary is very mobile as no breaking of bonds is necessary for movement. The height difference at a set point bias voltage of V_{bias} = -0.5 V is very pronounced (50 pm) due to the availability of SVB states for negative buckling. Single dI/dV spectra confirm the allocation of the buckling types to the domains (Fig. 4.7b).

The voltage range of the ABH measurements (Fig. 4.7c+d) allows consideration of the surface bands and the onset of the bulk bands. The tunnelling current in the surface band gap strongly depends on the tip sample distance and thus on the setpoint. While for a setpoint bias voltage in the band gap regime the tunnelling current is stable enough for measurements, at the setpoint of these ABH measurements of V_{bias} = +1.0 V and I_T = 0.1 nA, the tunnelling current

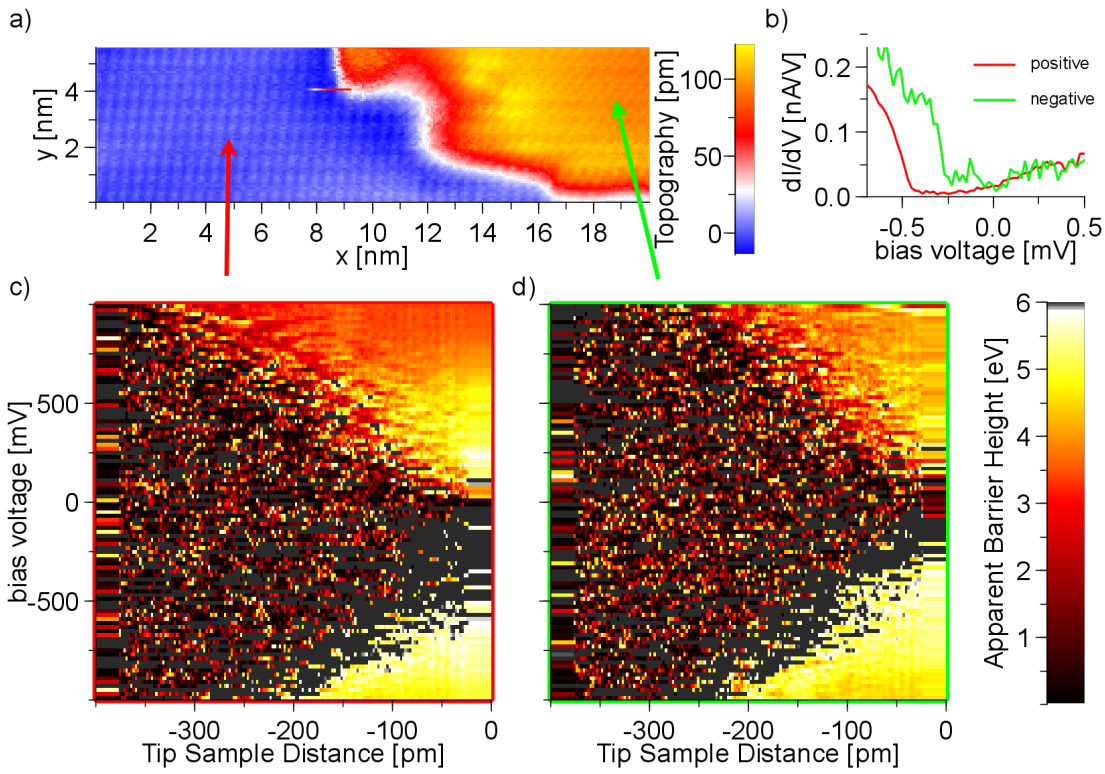

Figure 4.7: *Comparison of ABH values of positively (red) and negatively buckled (green) π-bonded chains:*
(a) Topography image (arrows mark positions of ABH measurements) [V_{bias} = -0.5 V ; I_t = 0.1 nA; T = 5.6 K].
(b) Single dI/dV spectra confirm the assignment of buckling types.
(c+d) ABH(z,V) in the voltage range of the surface band gap and the onset of the bulk bands [Setpoint: V_{bias} = -1.0 V ; I_t = 0.1 nA; T = 5.6 K].

is below the noise level in the surface band gap. All I(z,V) measurements were performed averaging over 10 I(z) measurements at each voltage step. Plots c+d show the ABH values extracted from the I(z,V) measurements by calculating ϕ(z,V) according to equation 3.24. As all considerations take place on the atomic scale, the ABH might be interpreted as inverse decay length of the wave function.

The general behaviour of the ABH measurements is the same for both domains. The lowest value with ∼3.5 eV belongs to the BCB. BVB and SCB show higher values with ∼4.5 eV and the SVB has the highest ABH with ∼5.5 eV. There is a difference of nearly 2.0 eV between SVB and BCB states.

In contrast to the distinct ABH differences in the separate bands for positive buckling, the transitions between the bands are less abrupt in the negatively

buckled domain. The shift in energy between the onsets of bulk band and SVB for positive and negative buckling is due to the different surface band structures (see section 4.2.1).

4.4 Conclusion

Examining domain boundaries with frontally meeting π-bonded chains we confirm the co-existence of positive and negative buckling on Si(111)2$\times$1 at 6 K and prove this co-existence also at room temperature. CITS measurements of multi-domain surfaces demonstrate spatially resolved differences in the electronic structure of different domains. The surface bands of both buckling types are located within the band gap of bulk silicon. Single dI/dV spectra show the different band gaps for positively and negatively buckled π-bonded chains, E_{Gp} = 520 (20) mV and E_{Gn} = 290 (20) mV, in qualitative agreement with other experiments and calculations [6, 27].

The relative positions of the surface bands of differently buckled π-bonded chains were determined. The surface bands of the π-bonded chains with negative buckling lie within the band gap of the π-bonded chains with positive buckling, and the energetic differences are $\Delta_{SVp-SVn}$ = -129 (10) mV and $\Delta_{SCp-SCn}$ = 99 (10) mV. These results are supported by the excellent match with calculations by Pötter and Rohlfing [31].

The voltage dependent ABH(z,V) shows the same major behaviour for both buckling types. The transitions between voltage regimes where surface states dominate the tunnelling process to regimes where the main contribution comes from the bulk bands is smooth in the case of negative buckling while the positively buckled domain shows rather sharp changes in the ABH(z,V).

All in all, positive and negative buckling behave very similar in all investigated properties. The differences are mainly in voltage dependencies caused by the differences in the positions of surface bands.

Chapter 5

Mobile domain boundaries

Domain boundaries on Si(111)-2×1 are stationary in most configurations, but under certain circumstances it is possible to change their position. Especially for domain boundaries of type III this is unexpected – they are mobile and may be moved (reversibly) several nanometres between two scanlines although two bonds per unit cell have to be broken for this re-localisation of the domain boundary. The energy cost for breaking a bond in bulk Si is assumed to be $\sim$ 2.3 eV [72], resulting in a required energy of ~ 14 eV per chain and nm under the assumption that the energy required for breaking a bond in the surface layer is comparable to the case of bulk atoms.

Such a reversible movement of a domain boundary was first observed by Trappmann *et al.* [14] in 1999. A domain boundary was found at different positions in a multi-bias image (Fig. 5.1a). At a sample bias voltage of +1.1 V (forward scan) it is located some nm further to the left than at -1.1 V (backward scan).

This movement of domain boundaries was not further investigated until in 2011 Studer *et al.* proposed a low energy pathway for the movement [15] which is based on a model of the formation of the π-bonded chains from the unreconstructed, buckled surface. According to Northrup and Cohen, this formation has an energy barrier of only 0.03 eV per surface atom [72]. Figure 5.1d shows the five steps required to move a domain boundary by one unit cell. In the first step, the left bond of the five atom ring moves from the surface atom at site 3 to the 'down'-atom at site 2. The former 'up'-atom on site 1 moves downward in step II resulting in two equal rings of six atoms (corresponding to the unreconstructed, buckled surface). In step III, starting from this buckled surface, the bond from former site 4 is re-arranged to the former 'up'-atom (site 1), leading to exchanged positions of five and seven atom ring with respect to step I. In the last step, all atoms relax to the positions of the buckled π-bonded chain reconstruction. Studer assumes a total energy of approximately 0.1 eV per

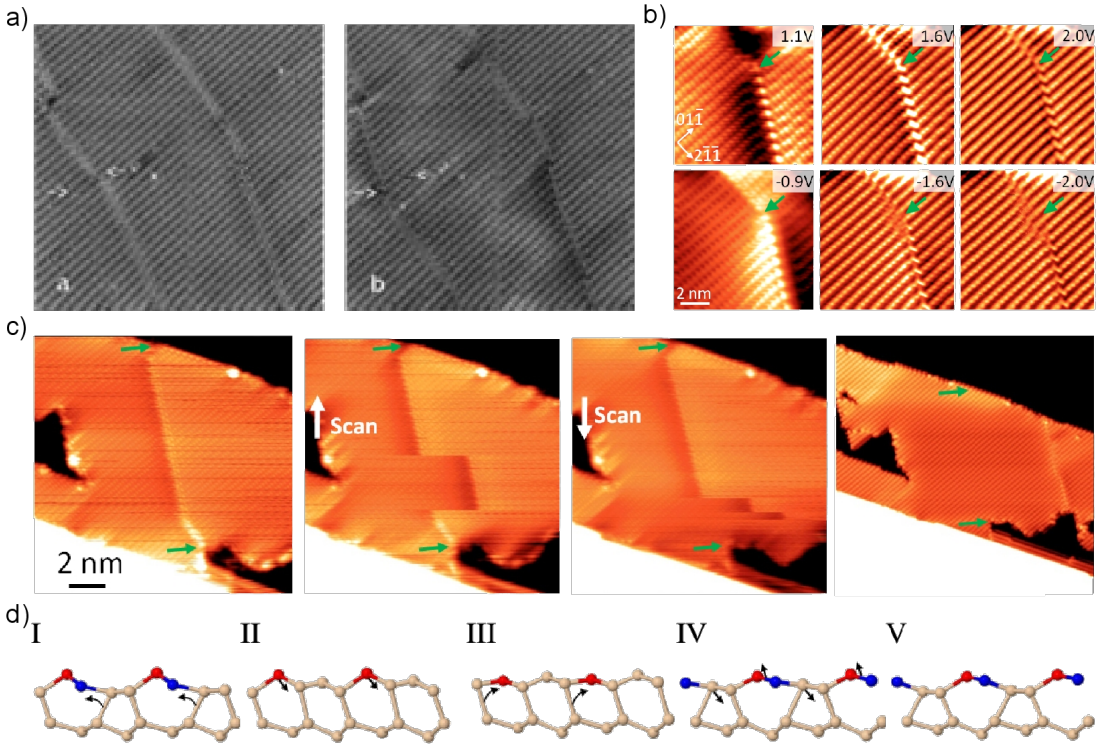

Figure 5.1: *(a) First measurements of mobile domain boundaries on Si(111)-2×1 at different sample bias voltages (left image: V_{bias} = +1.1 V in forward direction (left to right), right image: V_{bias} = -1.1 V in backward direction (right to left)) [250 Å× 250 Å; $N_D = 6 \times 10^{19}$ cm^{-3}] [14].*
(b) Reversible domain boundary movement at different voltages, green arrow indicates same position in all images [V_{bias} = +1.1 V / +1.6 V / +2.0 V / -0.9 V / -1.6 V / -2.0 V; I_t = 300 pA] [42].
(c) Domain boundary movement reducing the boundary length, green arrows mark original position of the domain boundary [42].
(d) Model for the mechanism of the domain boundary movement [42].

surface atom for the whole process [42]. This low energy barrier explains the high mobility of type III domain boundaries.

One cause for movement of domain boundaries is the reduction of energy when the length of the boundary is reduced by the movement (Fig. 5.1c) [15]. But the reason for reversible switching of boundary positions for different bias voltages (Fig. 5.1a+b) remains unclear. Trappmann *et al.* refer to the scan direction, different sample charge or tip-sample distance as possible causes [14]. Studer *et al.* found a boundary that is moved only at high negative voltages (Fig. 5.1b), and they exclude tip-sample distance as possible reason for the movement. They discuss vibrational excitations [73] or the electric field [74] as possible driving forces [15].

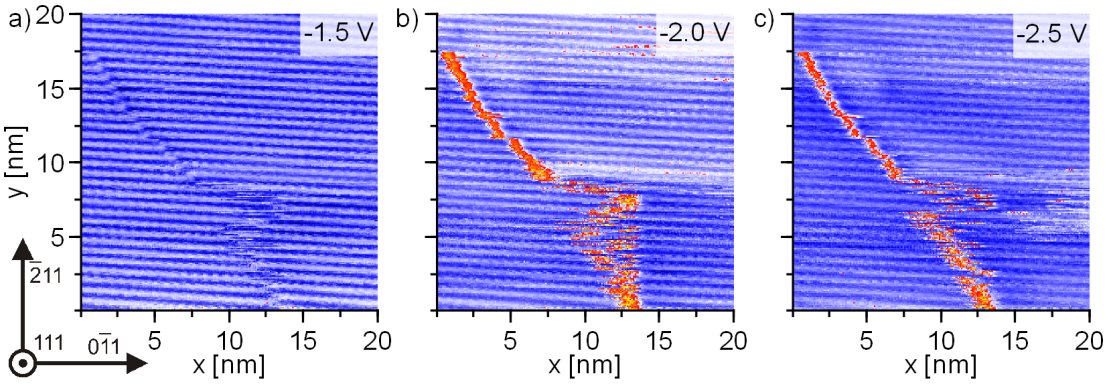

Figure 5.2: *Mobile domain boundary separating equally buckled domains: (a) V_{bias} = -1.5 V, (b) V_{bias} = -2.0 V, (c) V_{bias} = -2.5 V [I_t = 0.1 nA; T = 6 K].*

In this work, mobile domain boundaries were observed in three different general configurations. The first one is similar to the strain induced movement already thoroughly investigated by Studer *et al.* [15]. The domain boundary separates two positively buckled domains and is running approximately in ($\bar{1}$01) -direction (Fig. 5.2). At high negative voltages between -1.5 and -2.5 V the position is becoming unstable in the lower part of the domain boundary.

The second configuration, in which we found highly mobile domain boundaries, is a type IV domain boundary separating one domain with positive buckling and another one with negative buckling without any displacement of the π-bonded chains between the two domains (Fig. 5.3). The mobility of a domain boundary in this configuration is intuitive as not much energy is needed to change from positive to negative buckling because no bonds have to be broken. There is no stable configuration for such domain boundaries except when they are pinned by defects, e.g. P atoms.

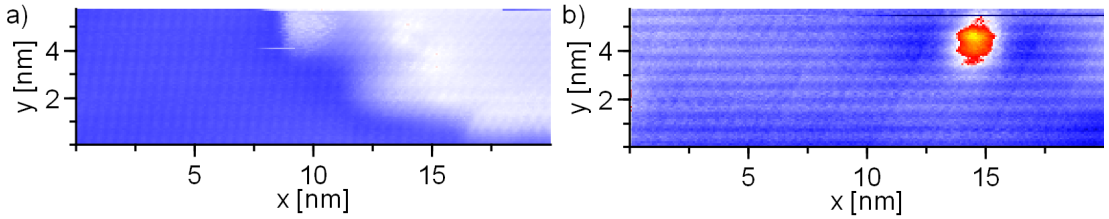

Figure 5.3: *Domain boundary without displacement of π-bonded chains: (a+b) Multi-bias image [V_{bias} = -0.5 V / +1.0 V; I_t = 0.1 nA; T = 6 K]: The domain boundary is only visible at -0.5 V (a). The image at +1.0 V shows no displacement of π-bonded chains (b).*

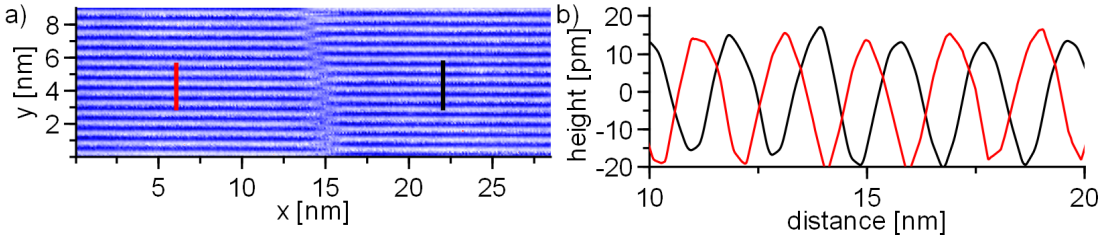

Figure 5.4: *(a) Close view of a mobile domain boundary [V_{bias} = -1.5 V; I_t = 0.1 nA; T = 6 K].*
(b) Comparison of the height profiles from the two domains (black and red line in (a)) indicates different buckling types.

The third configuration, which will be the topic of the main part of this chapter, is also one with differently buckled domains. But in this case, it is a type III domain boundary with a displacement of the π-bonded chains, and they are cut by the boundary. Figure 5.4 shows that the π-bonded chains have a lateral displacement ratio of 2:1 between upper and lower neighbouring chain in the other domain. As explained in chapter 4, this indicates differently buckled π-bonded chains in the two domains. We assume the contrast difference between the two domains at low negative voltages to be due to the different buckling types, as the onset of the SVB is at lower voltages for negative buckling, thus leading to a higher integrated DOS. Strain, as proposed by Studer et al [15], also results in an asymmetric electronic contrast at the domain boundary. Studer *et al.* find that the contrast is reversed when the polarity of the applied bias voltage is changed. In the differently buckled domains investigated in this chapter, the higher contrast is in the same domain for all applied voltages, in contrast to the strain induced signature observed by Studer *et al.*. Thus, we assume the influence of strain to be much smaller than the impact of the buckling type.

In order to determine the trigger for the change in position, we investigated a variety of parameters on two different mobile domain boundaries without changes in the tip configuration during the investigation of one domain boundary (Fig. 5.7 - 5.11). The fast scan direction is always in parallel to the π-bonded chains unless mentioned otherwise.

In our STM measurements, we are able to access several physical properties by varying the respective parameters:

Involved sample states: The sample states which contribute to the tunnelling process depend on the applied sample bias voltage. At high negative voltages of more than -1.0 V BVB states dominate, between -1.0 and -0.5 V (positive buckling) or -0.3 V (negative buckling) SVB states provide the major part, and in

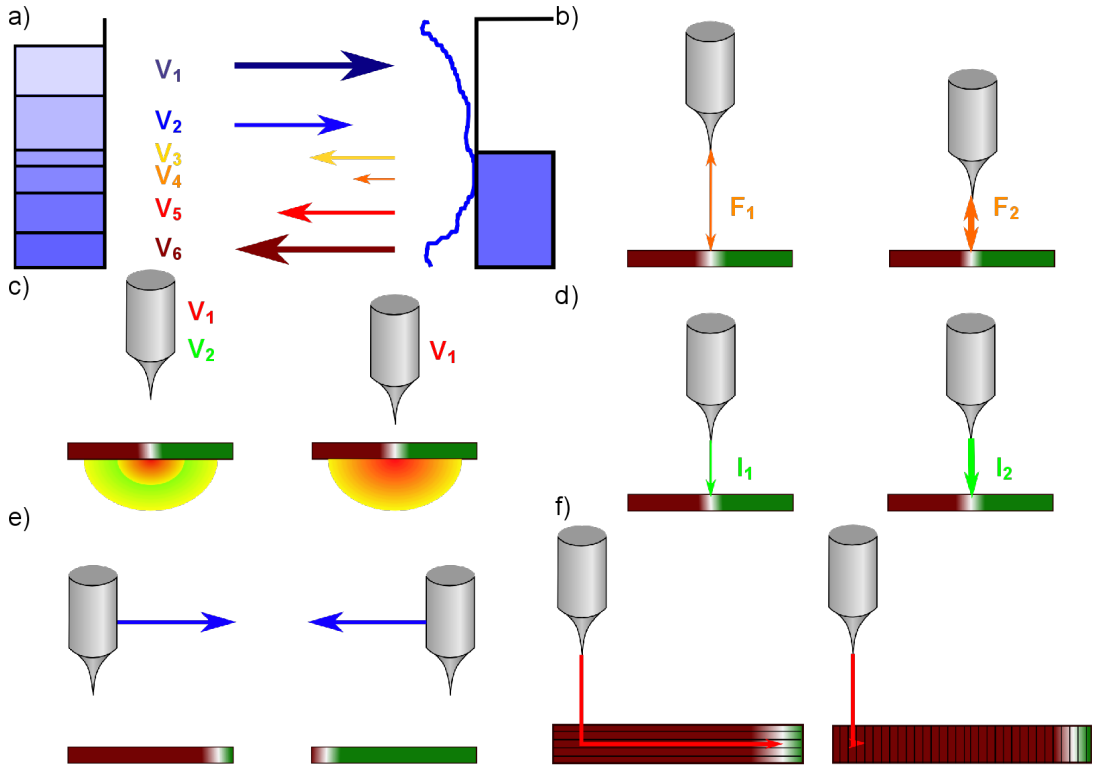

Figure 5.5: *Possible triggers for the domain boundary movement:*
(a) Depending on the applied voltage, different sample states contribute to the tunnelling process.
(b) The influence of atomic forces between tip and sample increases with decreasing tip sample distance.
(c) The strength of the tip induced electric field depends on the applied voltage as well as on the distance between tip and sample.
(d) The amount of involved electrons is higher for decreasing distance between tip and sample.
(e) The scan direction might influence the boundary position if the tip attracts or repulses the boundary.
(f) The angle between scan direction and direction of π-bonded chains indicates whether the trigger is transmitted along the π-bonded chains.

the surface band gap between SVB edge and E_F only electrons tunnelling out of filled SCB states contribute to the tunnelling process. At positive voltages between E_F and approximately 0.8 V tunnelling into SCB states is the major process, while for higher positive voltages BCB states dominate.

Electric field strength: The strength of the electric field induced by the presence of the tip scales linearly with the applied voltage. The effect of a change in the inverse tip sample distance strongly depends on the dimensionality of

the tip sample geometry. If the tip is modelled as a point charge, the electric field strength scales quadratically with the inverse tip sample distance, while modelling the tip as a plate results in a linear scaling.

Atomic forces: The influence of atomic forces between tip and sample may be addressed by varying the tip sample distance.

Tunnelling current: The amount of electrons involved in the tunnelling process is controlled via the tunnelling current. Changes in the tunnelling current are realised by changing the tip sample distance. This causes some difficulties in disentangling effects due to a variation in the tunnelling current from those caused by changes in the tip sample distance.

Tip interaction: Comparison between trace and retrace scan of the same measurement reveals whether the tip domain boundary interaction is repulsive or attractive or none of the two.

Transmission of movement trigger along π-bonded chains: Whether the trigger for the domain boundary movement is transmitted along the π-bonded chains may be investigated by performing measurements where the fast tip movement is parallel to the π-bonded chains and comparing them with measurements where the fast tip movement took place perpendicular to the π-bonded chains.

5.1 Voltage dependence

Figures 5.6 and 5.7 show a series of topography images of a domain boundary between positively (left side) and negatively (right side) buckled π-bonded chains. The domain boundary is running in $(1\bar{1}0)$-direction in the upper and lower part of the investigated area. As there is a displacement between the boundary parts, direction and course of the boundary are not fixed in the middle, where the boundary parts are joined. While upper and lower part of the boundary are stable, the position in the middle part strongly depends on the applied sample bias voltage. At high positive or negative voltages of more then $\pm 1.0\,\mathrm{V}$, the boundary position is fixed in a configuration that allows the boundary to run in $(1\bar{1}0)$-direction for the most part.

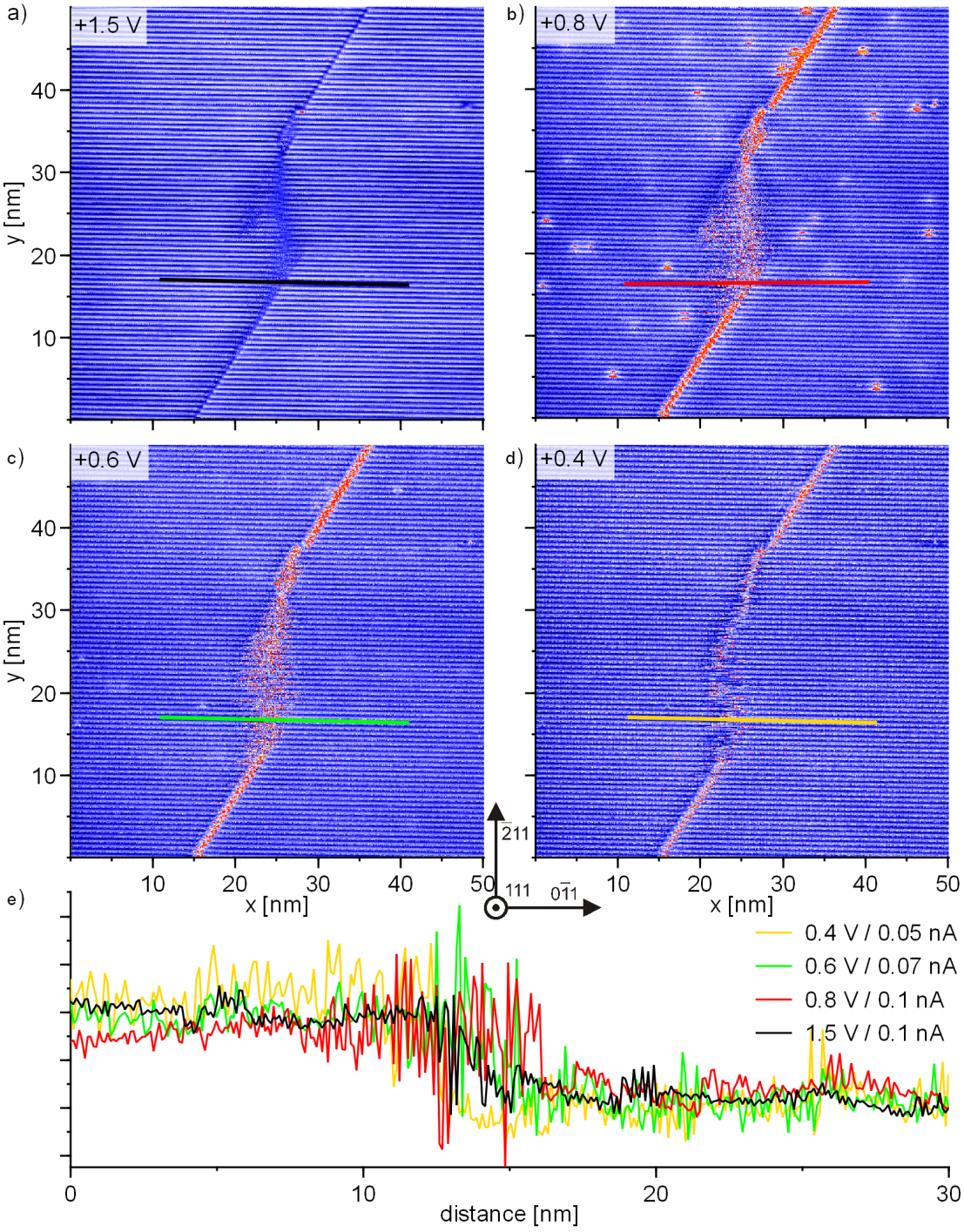

Figure 5.6: *Mobile domain boundary at different positive voltages:*
(a) [V_{bias} = +1.5 V; I_t = 0.1 nA], (b) [V_{bias} = +0.8 V; I_t = 0.1 nA], (c) [V_{bias} = +0.6 V; I_t = 0.07 nA], (d) [V_{bias} = +0.4 V; I_t = 0.05 nA]
(e) Height profiles show the extend of the movement.[all measurements at T = 6 K].

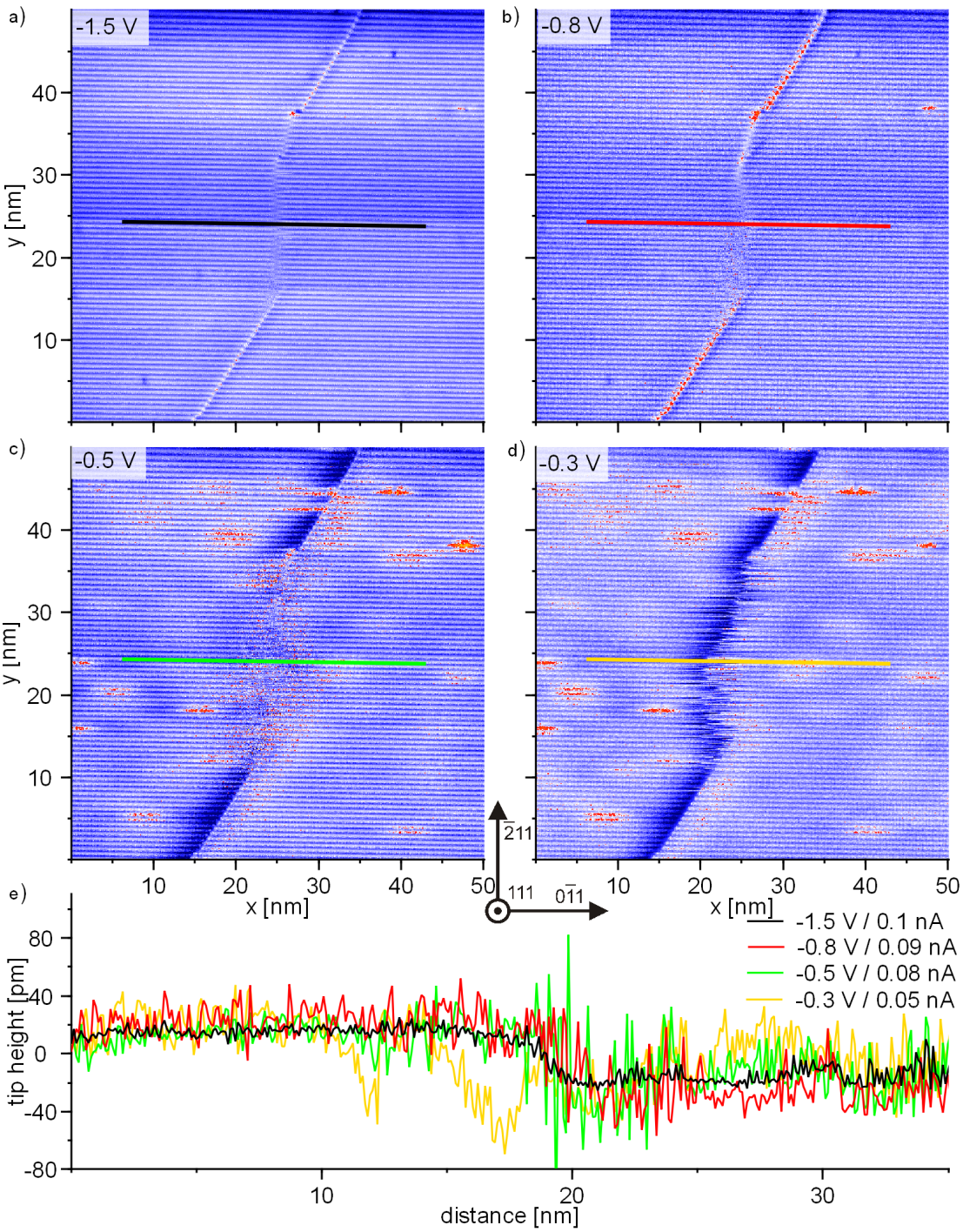

Figure 5.7: *The same mobile domain boundary as in Fig. 5.6 at different negative voltages:*
(a) [V_{bias} = -1.5 V; I_t = 0.1 nA], (b) [V_{bias} = -0.8 V; I_t = 0.09 nA], (c) [V_{bias} = -0.5 V; I_t = 0.08 nA], (d) [V_{bias} = -0.3 V; I_t = 0.05 nA]
(e) Height profiles at different positions show the extend of the movement.[all measurements at T = 6 K].

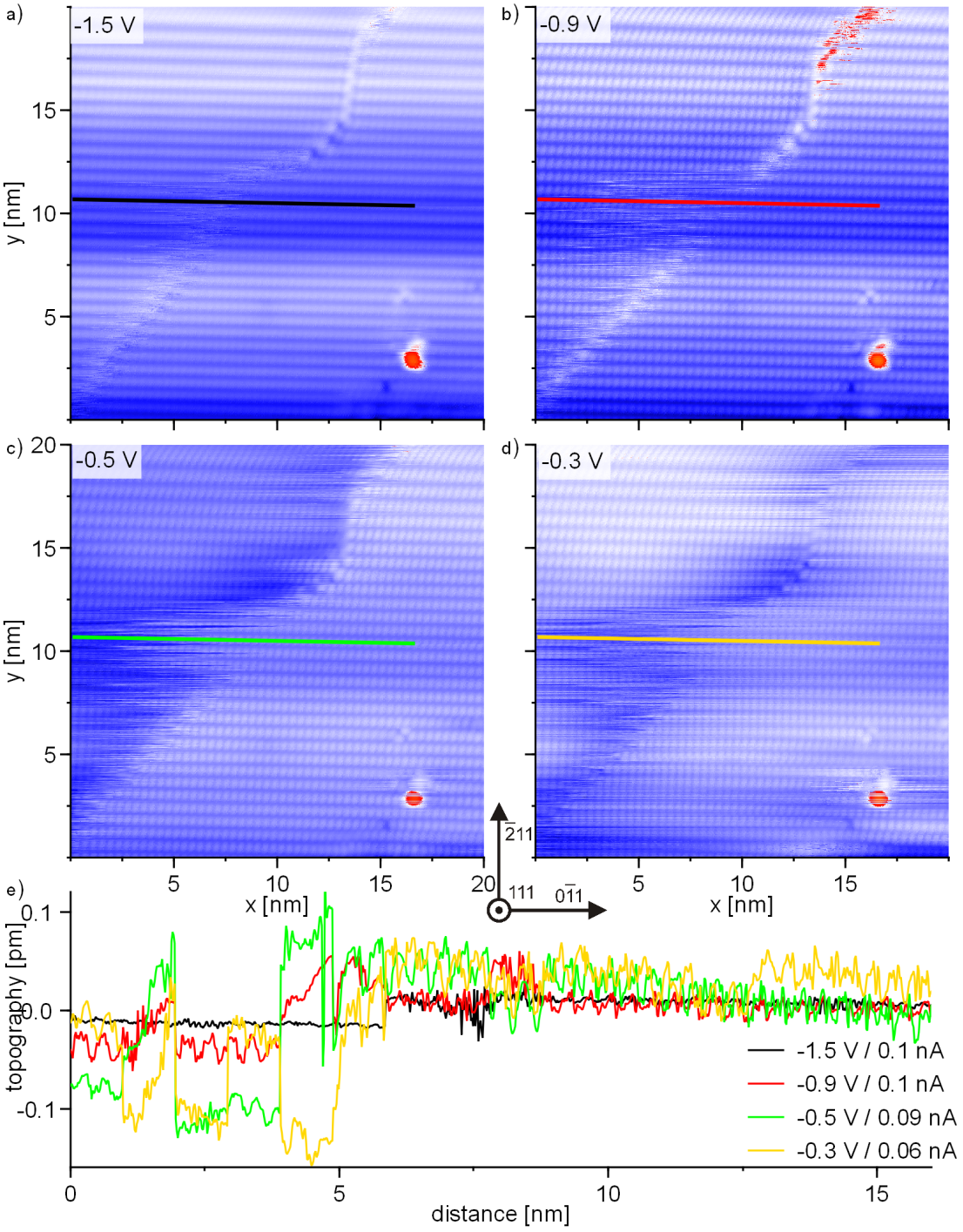

Figure 5.8: *A second mobile domain boundary at different negative voltages:*
(a) [V_{bias} = -1.5 V; I_t = 0.1 nA], (b) [V_{bias} = -0.9 V; I_t = 0.1 nA], (c) [V_{bias} = -0.5 V; I_t = 0.09 nA], (d) [V_{bias} = -0.3 V; I_t = 0.06 nA]
(e) Height profiles show the different extend of the movement [all measurements at T = 6 K].

With decreasing voltage, the boundary starts to flicker between different configurations until at +0.4 V the length of the negatively buckled π-bonded chains is increased up to 4 nm (Fig. 5.6d+e) and at -0.3 V up to 8 nm (Fig. 5.7d+e). The movement of the domain boundary is very fast and happens between two scan lines. The change in position is not triggered in every scan line leading to a seemingly unstable image.

Figure 5.8 shows a multi-bias series at different negative voltages of a second domain boundary. All further investigations were performed at this boundary. In the upper and lower part of the image area, the position of the domain boundary is stable, and the switching occurs only in $\sim$ 10 π-bonded chains in the middle of the image. The buckling of the π-bonded chains is positive on the left domain and negative in the domain at the right side. The domain boundary is at exactly the same position for all voltages in the stable part (Fig. 5.8). The middle part shows the same voltage dependence as the domain boundary in Fig. 5.7 with a length increase of the negatively buckled π-bonded chains of $\sim$ 5 nm (Fig. 5.8e).

5.2 Tip-sample distance and tunnelling current

In order to distinguish whether the movement of the boundary is directly induced by the applied voltage or by the greater proximity of the tip at lower voltages, a multi-current measurement was performed at -0.9 V. Because the movement starts at this voltage, one would expect a stationary boundary for higher distances (lower setpoint currents) and an increase of mobility for lower

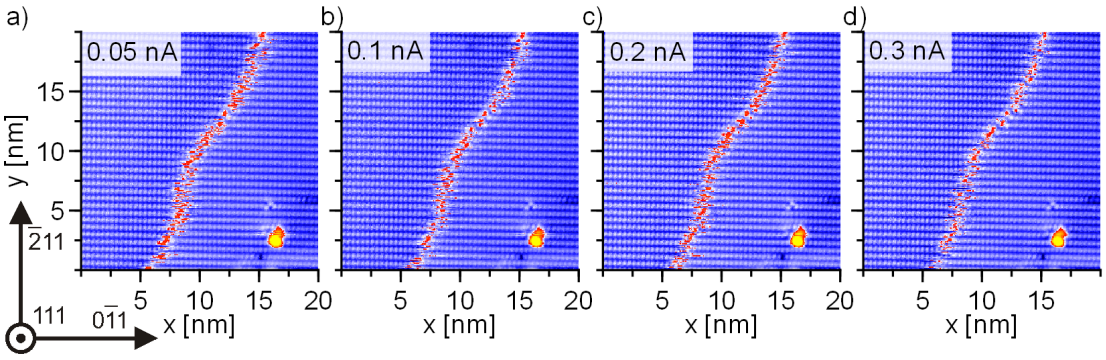

Figure 5.9: *Multi-current series with different setpoint currents at the same bias voltage : (a) I_t = 0.05 nA, (b) I_t = 0.1 nA, (c) I_t = 0.2 nA, (d) I_t = 0.3 nA, [V_{bias} = -0.9 V; T = 6 K].*

distances (higher setpoint currents) if the movement is caused by the proximity of the tip.

Figure 5.9 shows that this is not the case, the domain boundary is at exactly the same position for all distances (setpoint currents). As there is no effect, it is not necessary to disentangle the potential physical causes. This excludes atomic forces between tip and sample as possible cause for the movement as well as a strong dependence on the strength of the electric field. The amount of electrons injected into the π-bonded chain has also no effect on the mobility of the domain boundary.

5.3 Tip movement: for- and backward scan

In the next step, measurements with the tip scanning from the left to the right side (trace) and measurements with the tip scanning from the right to the left side (retrace) at the same bias voltage and setpoint current are compared. All data sets of the multi-bias measurement were obtained in trace as well as in retrace. This allows to investigate the impact of the scan direction on the movement. The tip might repulse the domain boundary. This would lead to a boundary movement in scan direction. If the domain boundary was attracted by the tip, the movement would be in the opposite direction.

While at low negative voltages up to -0.6 V there is no difference in the length or direction of the movement between trace and retrace, at higher negative voltages there is a slight movement of the boundary toward the tip when scanning in trace direction (Fig. 5.10). In the retrace images, the domain boundary is stable, running in $(1\bar{1}0)$-direction. According to this, the tip seems to attract the negatively buckled π-bonded chains but not the chains with positive buckling. The small impact of the scan direction on the boundary position is hidden in the extensive movement at negative voltages below -0.4 V.

5.4 Tip movement: parallel and perpendicular to π-bonded chains

Figure 5.11 shows data sets of a multi-bias measurement where the tip was scanning perpendicular to the π-bonded chains instead of along them, which is the case for the other measurements. The resulting images are very different compared to the measurements parallel to the π-bonded chains (Fig. 5.8). From

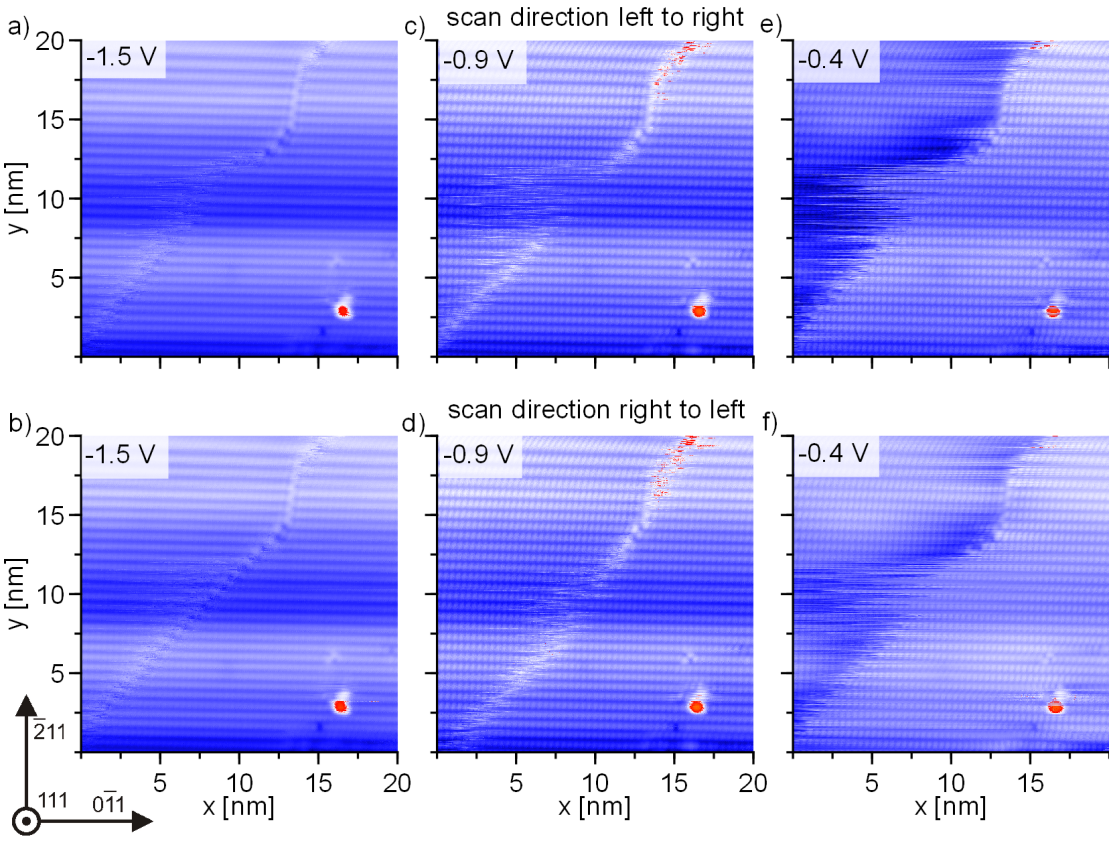

Figure 5.10: *Comparison between trace and retrace movement: (a+c+d) Data sets of multi-bias series with tip scanning from left to right side, (b+e+f) data sets of multi-bias series with tip scanning from right to left side.*
(a+b) [V_{bias} = -1.5 V; I_t = 0.1 nA; T = 6 K], (c+d) [V_{bias} = -0.9 V; I_t = 0.1 nA; T = 6 K], (e+f) [V_{bias} = -0.4 V; I_t = 0.07 nA; T = 6 K].

the jagged looking chains in the middle of the images, it is obvious that the domain boundary is not stationary but moving. But the dependence on the applied voltage is completely absent, all images show the same configuration in every part of the image. When the boundary is at a certain position it stays for some scan lines and during all consecutive scans at different voltages, performed in each line, until it moves to a different position. Considering the results from the voltage dependent measurements scanning parallel to the chains, we conclude that the boundary movement occurs during the measurements at low voltages and that the different boundary positions are present in the data sets at higher voltages due to the longer time the boundary stays at one position.

This behaviour leads to the assumption that the movement of the domain boundaries is initiated by excitations via the tip which are transmitted within the π-bonded chains but not perpendicular to them.

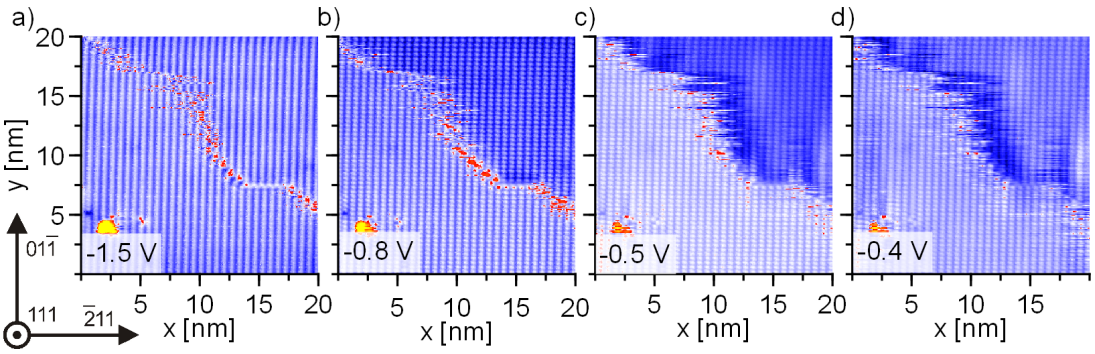

Figure 5.11: *Data sets with tip scanning perpendicular to the π-bonded chains: (a) [V_{bias} = -1.5 V; I_t = 0.1 nA; T = 6 K], (b) [V_{bias} = -0.8 V; I_t = 0.1 nA; T = 6 K], (c) [V_{bias} = -0.5 V; I_t = 0.09 nA; T = 6 K], (d) [V_{bias} = -0.4 V; I_t = 0.07 nA; T = 6 K].*

5.5 Conclusion

By performing a series of measurements at mobile domain boundaries, varying several parameters, we were able to gain further information on the cause of the movement:

- The addressed sample states are crucial for triggering the movement (voltage dependence). Only if the major contribution to the tunnelling current comes from the surface states, the movement occurs.
- The movement of the domain boundaries is always in favour of the negatively buckled domain. The impact is strongest for low negative voltages above the SVB edge of the positively buckled π-bonded chains but below the edge of the SVB of negatively buckled chains (voltage dependence).
- The length scale of the movement comes up to several nanometres (low negative voltage).
- Atomic forces between tip and sample do not trigger the movement (tip sample distance via setpoint current).
- The **strength** of the electric field induced by the tip has no significant influence (no dependence on tip sample distance). This is presumably due to the fact that the field is easily screened by the metallic surface.
- The movement is not influenced by the amount of current into the π-bonded chains (no current dependence).

- The movement is not simply initiated by the tip pushing or pulling the domain boundary (comparison trace vs. retrace measurements).

- The excitation is carried within the π-bonded chains and suppressed perpendicular to them (comparison scan direction parallel vs. perpendicular to π-bonded chains).

It is obvious that the tip induces the movement of the domain boundary. The length scale on which the movement occurs corresponds to the typical radius of our STM tips [61]. Thus the **presence** of the electric field of the tip is presumed to reach the π-bonded chains on the other side of the domain boundary at this distance although the actual tunnelling is restricted to the atom directly beneath the tip.

The fact that switching to negative buckling seems to be preferable at voltages which address the **surface band gap** of the **positively buckled** π-bonded chains but the **surface states** of the **negatively buckled** π-bonded chains might be explained by the higher LDOS of negatively buckled π-bonded chains at these voltages due to the availability of surface states. A similar effect is reported by Bussetti *et al.* [6] who find negative buckling only at Si(111)-2$\times$1 samples with high negative doping. They assume that the occupation of normally empty states due to the abundance of dopant electrons makes the formation of negatively buckled Si(111)-2$\times$1 favourable. In accordance with this explanation, we assume that the movement of the domain boundaries occurs in order to increase the share of negatively buckled π-bonded chains and thus provide surface states available for tunnelling in the energetic region of the applied bias voltage.

Note that this movement of a domain boundary in order to enlarge a negatively buckled domain is favourable only for very special configurations of the domain boundary. The major part of domain boundaries with a displacement of the π-bonded chains is stable.

Chapter 6

Signatures induced by P-atoms

In this chapter, signatures induced by single P atoms and correlations between them are investigated. There is a large variety of configurations in which P atoms can be found in Si(111)-2×1: First of all, there are four different sites where P atoms can be positioned in the surface unit cell which have to be considered separately for the two buckling types (Fig. 6.1a). In addition, the environment of the P atoms, especially the length of the π-bonded chains plays an important role. As depicted in Fig. 6.1b, there are several configurations which reduce the chain length on one or both sides: up- and downward surface steps and all kinds of domain boundaries. Measurements on 'quasi-free' π-bonded chains are only possible in the absence of these defects. There also may be signatures of P atoms located in subsurface layers (Fig. 6.1c), as already reported for Sb and Bi in Si(111)-2×1 [42]. The fourth kind of configuration are P atoms in such small distances that they influence each other (Fig. 6.1d). In this case, a distinction has to be made between correlations of P signatures in the same π-bonded chain ($(0\bar{1}1)$-direction) or in neighbouring π-bonded chains ($(\bar{2}11)$-direction). In addition, the influence may be different depending on the layer of the P atom (surface or subsurface) or for more than two signatures.

6.1 P-atoms at different surface sites in p- and n-buckled Si(111)-2×1

In this section, P atoms at different surface sites and the impact of the buckling type on the signatures induced by P atoms is investigated. P atoms in positively buckled π-bonded chains were thoroughly treated by J. K. Garleff in [43,68]. But up to now, no such study exists for negative buckling.

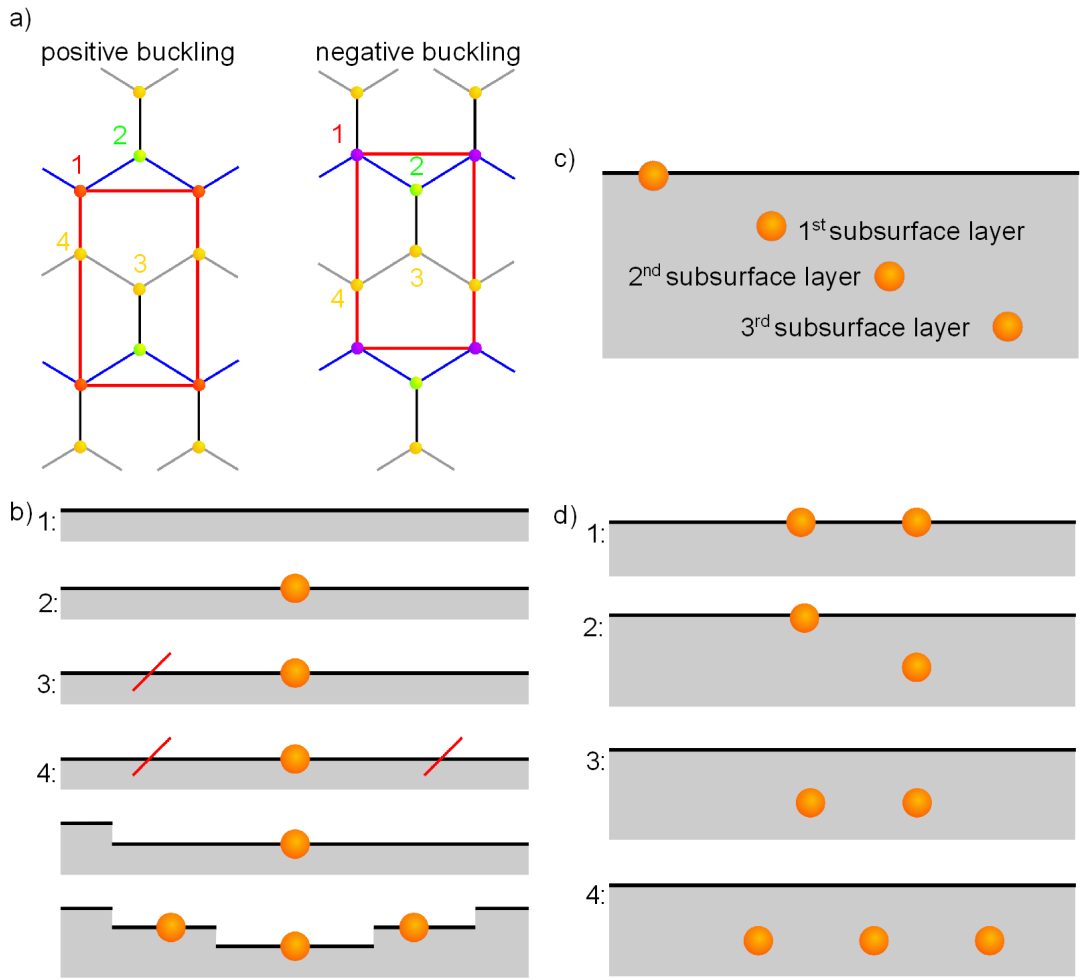

Figure 6.1: *P atom configurations:*
(a) Four sites in the unit cell of Si(111)-2×1 with positive (left side) and negative (right side) buckling.
(b-d) black line – π-bonded chain, grey area – bulk Si, orange ball – P atom, red line – domain boundary.
(b) Surface configurations: (1) free Si(111)-2×1 surface, P atoms in infinite (2) π-bonded chains, restricted by one (3) or two (4) domain boundaries, and limited on only one side by a step (5) or on both sides by different surface step configurations (6).
(c) P atoms in the surface layer and 1-3 layers beneath the surface.
(d) Different configurations of P atoms which might influence each other: both P atoms in surface layer (1), one P atom in the surface, the other in a subsurface layer (2), both atoms in subsurface layers (3) and more than two P atoms (4).

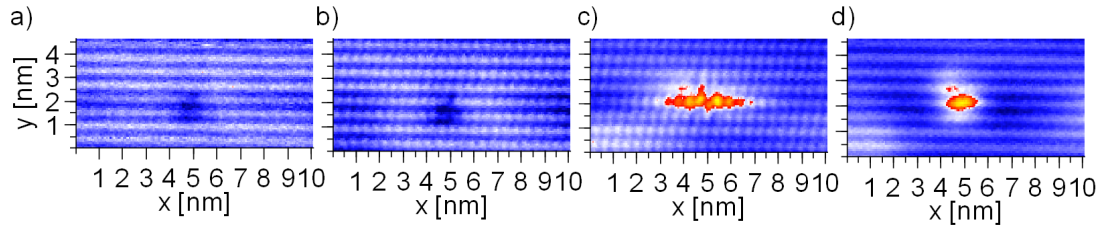

Figure 6.2: *P atoms in positively buckled π-bonded chains at different bias voltages [I_t = 0.1 nA; T = 6 K]: (a) V_{bias} = -2.0 V, (b) V_{bias} = -1.0 V, (c) V_{bias} = -0.5 V, (d) V_{bias} = +1.0 V.*

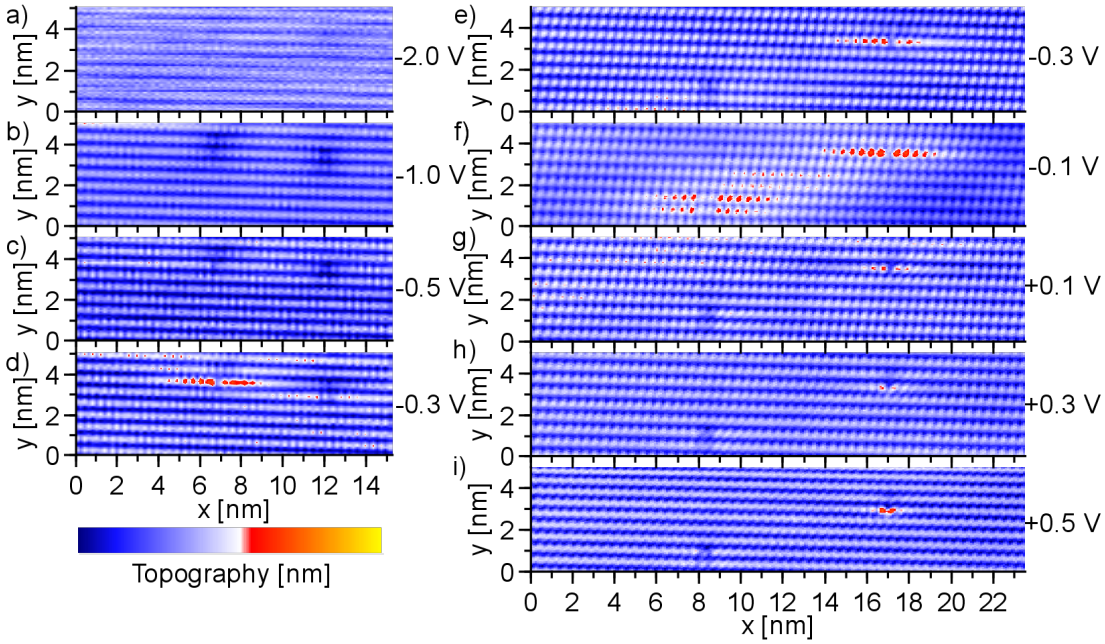

Figure 6.3: *P atoms in negatively buckled π-bonded chains at different bias voltages [I_t = 0.1 nA; T = 6 K]: (a) V_{bias} = -2.0 V, (b) V_{bias} = -1.0 V, (c) V_{bias} = -0.5 V, (d) V_{bias} = -0.3 V, (e) V_{bias} = -0.3 V, (f) V_{bias} = -0.1 V, (g) V_{bias} = +0.1 V, (h) V_{bias} = +0.3 V, (i) V_{bias} = +0.5 V, and (j) V_{bias} = +1.0 V.*

6.1.1 Voltage dependent signature

The signature of P atoms in Si(111)-2×1 strongly depends on the applied sample bias voltage (Fig. 6.2 and 6.3). This voltage dependence is similar for both buckling types although the exact voltage values differ. For high negative voltages, down to a threshold voltage (V_T), the P atom appears as a depression in topography images (Fig. 6.2a+b and 6.3a-c). At negative voltages smaller than V_T a highly anisotropic contrast enhancement appears which is restricted to one single or two adjacent π-bonded chains and extends about 10 nm along the

chains (Fig. 6.2c and 6.3d-f). V_T differs between positive and negative buckling. Positive buckling shows V_{Tp} = -0.5 V (Fig. 6.2b+c) which is higher than the value for negative buckling where we find V_{Tn} = -0.3 V (Fig. 6.3c+d). These values for V_T coincide with the upper edge of the SVBs for the two buckling types.

At low positive voltages between +0.1 V and +0.5 V, when electrons tunnel from the tip into the SCB, the anisotropic contrast enhancement disappears and gives way to signatures which depend on the binding site of the P atom (Fig. 6.3g-i). P atoms on sites between π-bonded chains (signatures in the lower left of Fig. 6.3e-i) show a depression similar to the signature at high negative voltages. P atoms in the π-bonded chain have a signature that evolves from the anisotropic contrast enhancement to one located only at the P atom site (upper right of Fig. 6.3e-i) going from low to higher positive voltages. At high positive voltages of +1.0 V and more, when the main contribution to the tunnelling current comes from electrons tunnelling into BCB states, P atoms show as protrusion localized at the P atom site (see Fig. 6.2d).

The voltage dependence of the anisotropic contrast indicates that the origin of this contrast might be scattering of electrons near the SCB minimum (at $\bar{J}$ point) which is just below E_F for both buckling types due to the high n-type doping [37]. This assumption is supported by DFT calculations by M. Rohlfing which show a strong localisation of the defect state at the site of the P atom within 1-2 angstrom. Apparently, the charge of the additional electron (from the P atom) is strongly localised at the P atom and does not spread out along the Pandey chain (Fig. 6.4). This results in a neutral charge state of substitutional P atoms in the Si(111)-2×1 surface [45]. The strong localisation of the defect state within one surface unit cell excludes the interpretation of the 10 nm long contrast as a signature of the additional electron charge at the P atom site.

6.1.2 Phosphorus atoms at different binding sites

As already described in section 2.1, the Si(111)-2×1 reconstruction offers four different binding sites in the surface unit cell (Fig. 6.5a+g). P atoms may replace a Si at all four sites. Additionally, there might be new reconstructions which reduce energy as found for Sb and Bi in Si(111)-2×1 [42]. At low temperature, different contrast patterns show up in STM images for voltages above V_T and low negative voltages between V_T and E_F (Fig. 6.5). While in positive buckling the two distinctive contrasts are best observed at -1.0 V and -0.5 V, these contrasts appear at -0.5 V and -0.3 V for negative buckling. Assignation of P induced contrast patterns in STM images to the four binding sites is done by simple geometric considerations.

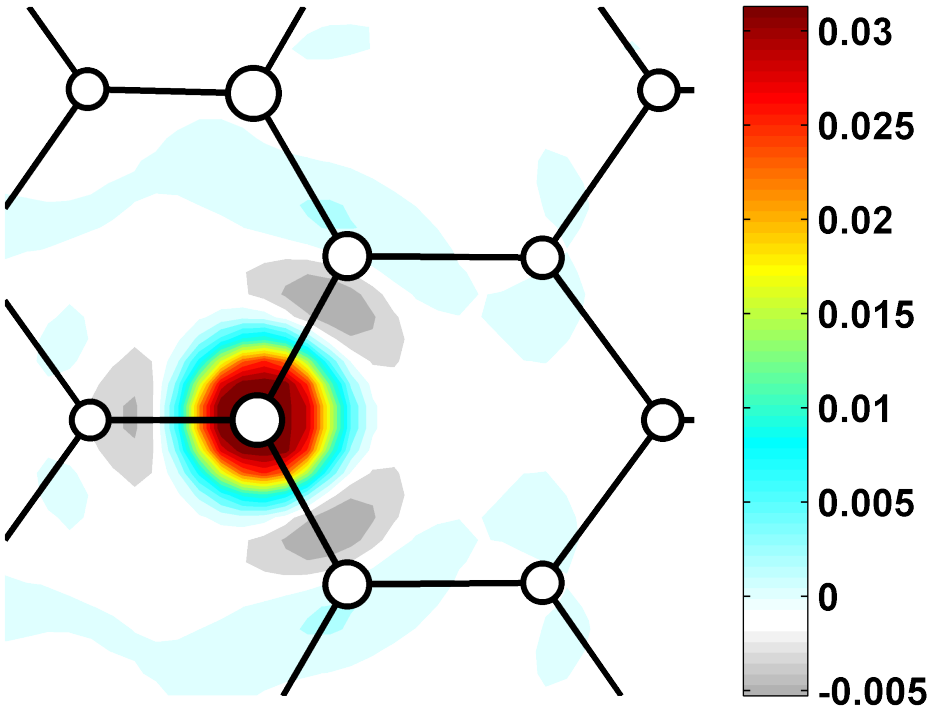

Figure 6.4: *Calculated difference $\Delta\rho$ (in arbitrary units) in the electronic charge density between the surface with and without a P atom on site 1. For better visibility, the 3D $\Delta\rho(x,y,z)$ has been integrated along the surface normal (z), yielding a two-dimensional (2D) $\Delta\tilde{\rho}(x,y)$ along the surface [45].*

The sites have different mirror symmetries. The mirror axis in $(\bar{2}11)$-direction (perpendicular to the chains) is on the up-atom for site 1 and 4 (red arrows in Fig. 6.5) and on the down-atom for site 2 and 3 (green arrows in Fig. 6.5). The distinction between P atoms in the π-bonded chain and P atoms in the second layer is done by comparing multi-bias images of $|V_{bias}| > |V_T|$ and $|V_{bias}| < |V_T|$. The contrast pattern for $|V_{bias}| > |V_T|$ (localised depression) is in the same π-bonded chain as the anisotropic contrast enhancement appearing for $|V_{bias}| < |V_T|$ when the P atom is located in the π-bonded chain (site 1 and 2). For site 1 and 2 the contrast enhancement is restricted to one π-bonded chain (black arrows in Fig. 6.5). For P atoms located between the π-bonded chains (site 3 and 4) there is a small crosstalk on one adjacent

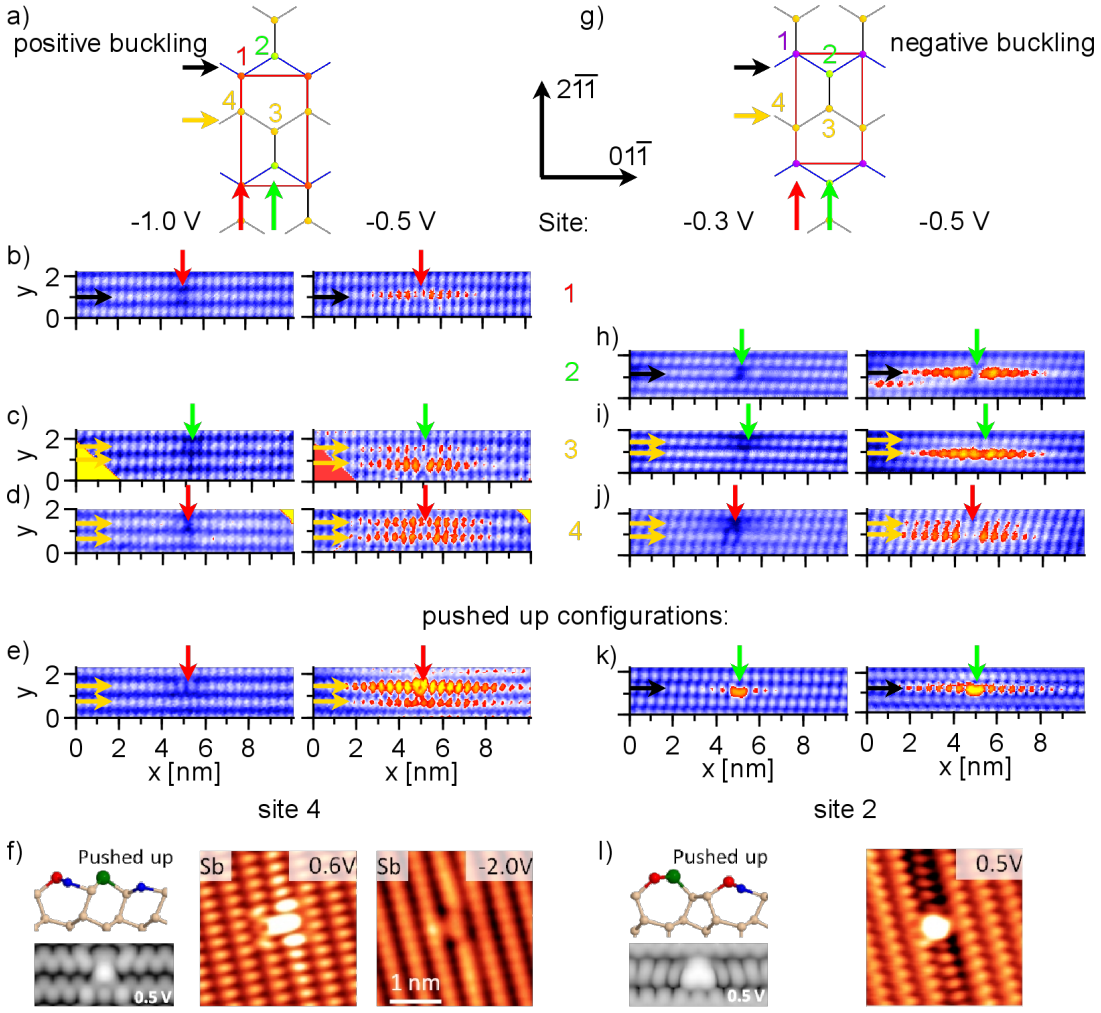

Figure 6.5: *P atoms in positively (a-f) and negatively (g-l) buckled π-bonded chains at different binding sites and for $|V_{bias}| > |V_T|$ and $|V_{bias}| < |V_T|$ [$I_t = 0.1\,nA$; $T = 6\,K$]. Data for positive buckling taken from [68]:*
(a+g) Model of the surface unit cell, illustrating site 1-4.
(b) P atom at site 1, (h) P atom at site 2, (c+i) P atom at site 3 and (d+j) P atom at site 4.
(e) P atom in positively buckled π-bonded chain at site 4 in pushed up reconstruction.
(f) Model and LDOS distribution via DFT calculations and STM measurements for Sb at site 4 in pushed up reconstruction [42].
(k) P atom in negatively buckled π-bonded chain at site 2 in pushed up reconstruction.
(l) Model and LDOS distribution via DFT calculations and STM measurements for Sb at site 2 in pushed up reconstruction [42].

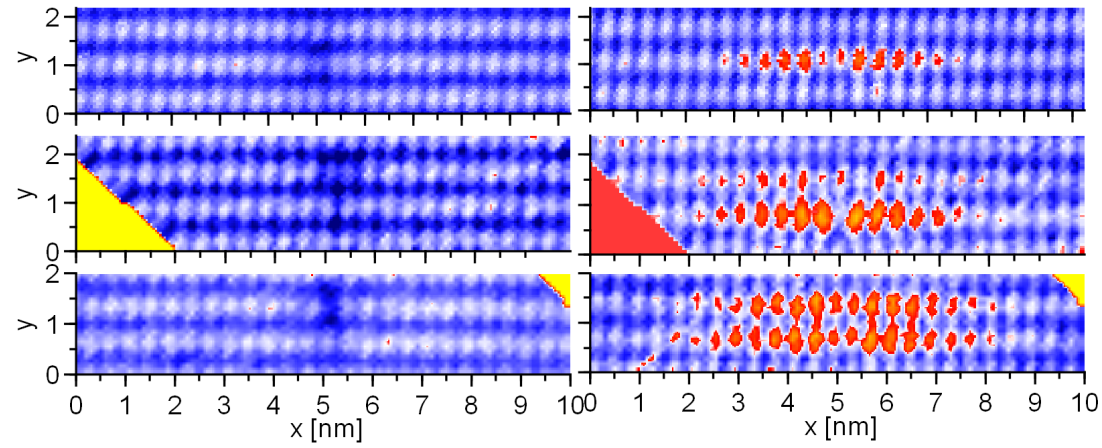

Figure 6.6: *Enlarged STM images of P atoms in positively buckled π-bonded chains (left side – V_{bias} = -1.0 V, right side – V_{bias} = -0.5 V, [I_t = 0.1 nA; T = 6 K]) Raw data taken from [68]:*
(a) P atom at site 1, (b) P atom at site 3 and (c) P atom at site 4.

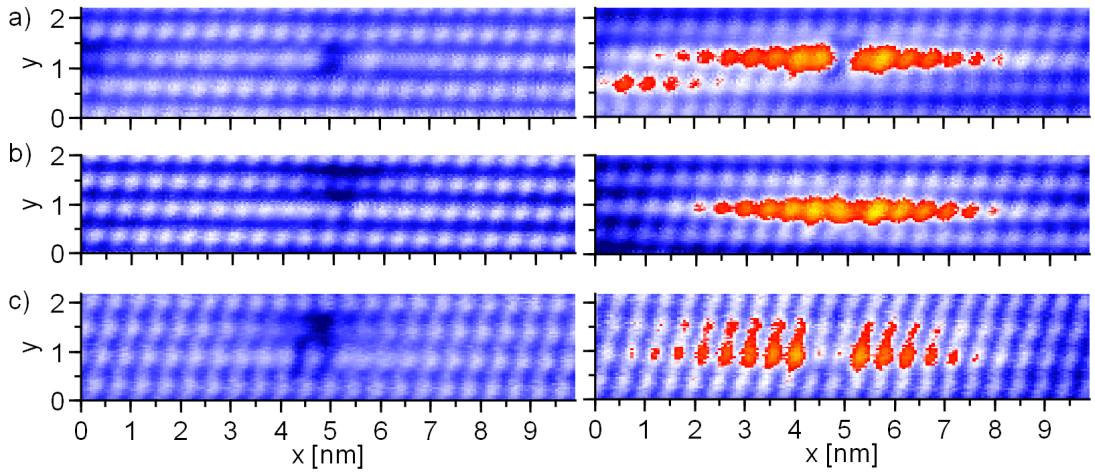

Figure 6.7: *Enlarged STM images of P atoms in negatively buckled π-bonded chains (left side – V_{bias} = -0.5 V, right side – V_{bias} = -0.3 V, [I_t = 0.1 nA; T = 6 K]):*
(a) P atom at site 2, (b) P atom at site 3 and (c) P atom at site 4.

chain (yellow arrows in Fig. 6.5). The depression for $|V_{bias}| > |V_T|$ is located in this adjacent chain for both sites. According to these considerations, we are able to assign all P induced signatures to P atoms at site 1-4 (Fig. 6.5b-e and h-k, 6.6, and 6.7).

Garleff *et al.* found four different contrast patterns induced by P atoms in positively buckled π-bonded chains. They were able to assign three of those contrast patterns to P atoms at site 1 (up-atom in π-bonded chain), site 3 (second layer atom next to down atom), and site 4 (second layer atom next to up-atom) (see Fig. 6.5b-d and 6.6) while the fourth contrast was not fully understood [43]. Those contrast patterns were also observed during this work.

P atoms on site 1 show an extended contrast along one π-bonded chain with a slightly reduced intensity on the two atoms in the middle at -0.5 V and a depression in the same chain at an 'up'-atom site for -1.0 V. The symmetry axis perpendicular to the chain of the elongated contrast is crossing an 'up'-atom (Fig. 6.5b and 6.6a). On site 2, the features should also be located in the same chain for both voltages but the mirror axis should cross a 'down'-atom. Such a contrast was neither found by Garleff *et al.* [43] nor in this work. For P atoms an site 3 and 4, the contrast enhancement at -0.5 V extends on two neighbouring chains. This contrast is stronger in one chain with only a small cross-talk on the other for site 3. The mirror axis crosses the 'down' atom and at -1.0 V a depression is visible in the chain which shows the weaker contrast at -0.5 V (Fig. 6.5c and 6.6b). P on site 4 leads to equally strong contrasts in the adjacent chains at -0.5 V and a strong depression at an 'up'-atom site in one of the chains at -1.0 V. The symmetry axis crosses an 'up'-atom (Fig. 6.5d and 6.6c).

The mirror axis in $(\bar{2}11)$-direction of the fourth signature (Fig. 6.5e) is at the 'up'-atom, thus the P atom must be located either at site 1 or 4. P. Studer [42] compared this P induced contrast pattern with one he found for Sb and Bi on site 4 and found a remarkable agreement (Fig. 6.5f). As Sb and Bi on site 4 form a new reconstruction where the donor atom is pushed out of the surface, the suggestion is obvious that this fourth P induced signature in positively buckled π-bonded chains is a P atom on site 4 in this pushed up reconstruction.

Investigating the contrast patterns of P atoms in negatively buckled domains, we also found four different signatures (Fig. 6.5h-k and 6.7). These contrasts patterns can be assigned to substitutional P atoms on site 2, 3, and 4. A signature fulfilling the geometric requirements of a P atom on site 1 was not found.

Apart from the different voltages at which the contrast patterns occur, the signatures for P atoms at site 3 and 4 are identical for positive (Fig. 6.5c+d and 6.6b+c) and negative (Fig. 6.5i+j and 6.7b+c) buckling of the π bonded chains. The signature of a P atom on site 2 shows a distinct indention at the P site at

-0.5 V, and the anisotropic contrast enhancement visible at -0.3 also is strongly reduced at the P site and at the two neighbouring atoms (Fig. 6.5h and 6.7a). A comparison for site 1 and 2 is not possible, as site 1 was only found in positively buckled domains while site 2 could only be observed in negatively buckled areas.

The fourth signature is also a P atom at site 2, but with an altered configuration. At higher negative voltages, a protrusion highly located between two up-atoms is visible. At -0.3 V, the same protrusion is still visible and in addition there is also an anisotropic contrast. But the maxima are shifted increasingly to the up-atom sites with decreasing distance to the P atom (Fig. 6.5k). Comparison with STM and DFT data for Bi and Sb in Si(111)-2×1 (Fig. 6.5l) [15] leads to the conclusion that this altered signature might be caused by an upward buckling of the P atom. According to calculations by Studer *et al.*, which compare the total energies of the normal and the altered configuration, the upward buckling of a P atom on site two even is slightly favourable, leading to an energy gain of 0.04 eV [42].

6.1.3 Defect induced states

The spectroscopic signature of P atoms in Si(111)-2×1 is dominated by the long range signature of electrons scattered at this defect. The additional charge located directly at the site of the P atom (Fig. 6.4a) does not give rise to a localised feature visible in dI/dV data. The spectroscopic signature is identical for P atoms on all sites, according to J. K. Garleff [68]. This is plausible because the scattering behaviour of electrons is determined by the characteristics of the SCB and not by the defect at which they are scattered. A comparison for P atoms on different sites in negative buckling is not possible in this work due to the lack of dI/dV data. But assumedly the behaviour is similar to P atoms in positively buckled Si(111)-2×1 and thus the spectral signature the same for all sites.

Figure 6.8 shows data of dI/dV(x,y,V) measurements via lock-in technique of an upward buckled P atom on site 2 in negatively buckled π-bonded chains (c+e) and dI/dV(x,y,V) data obtained by numerical derivation along a positively buckled π-bonded chain with a P atom on site 3 (d+f). The black dI/dV curves were taken directly above the P atoms, the blue curves shows the signature of a defect-free, π-bonded chain, and the yellow curves were taken next to the P atoms, showing a combination of LDOS signatures from black and blue curves. The spectrum above the P atom shows a strongly enhanced LDOS at -0.25 V while the LDOS is strongly diminished at -0.37 V for negative buckling. For positive buckling, the enhancement is located at the same energetic position [68]

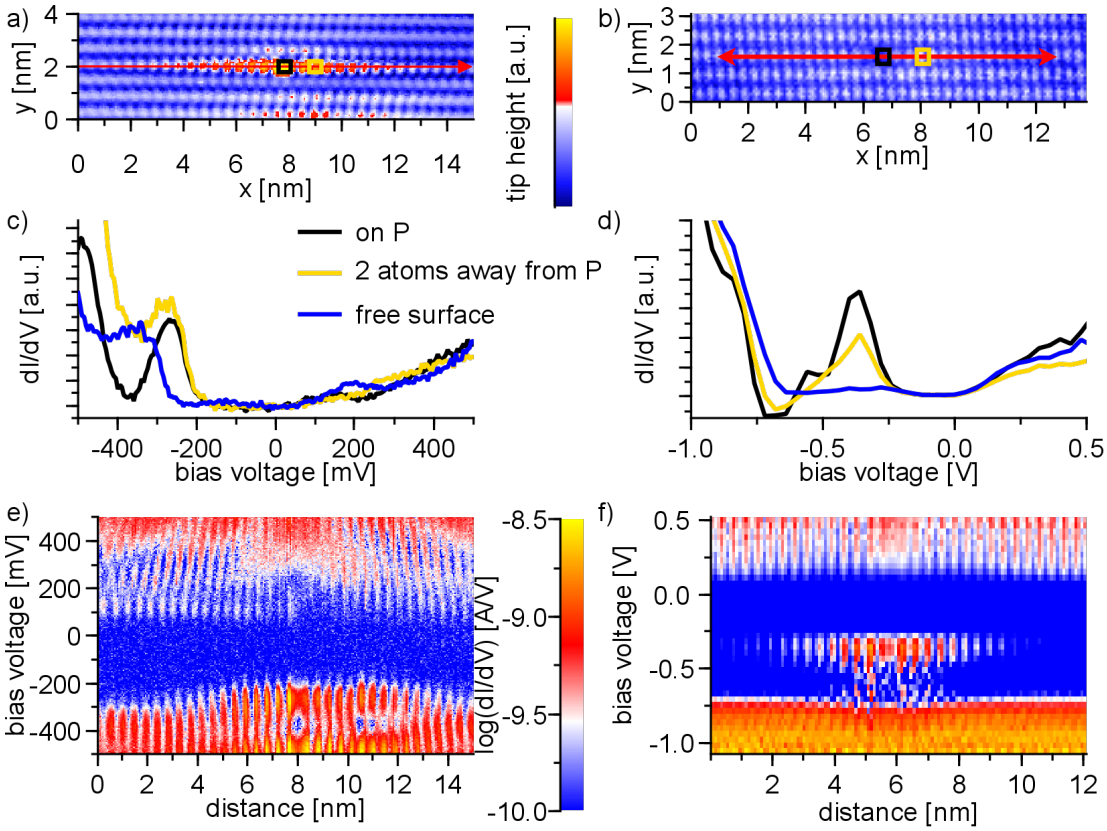

Figure 6.8: *Spectroscopy of phosphorus atoms in negatively (a+c+e) and positively (b+d+f) buckled π-bonded chains. Data for positive buckling taken from [68]:*
(a) Topography image of P atom at site 2 (pushed up) in negatively buckled π-bonded chain [V_{bias} = -0.5 V; I_t = 0.1 nA; T = 6 K].
(b) Topography image of P atom at site 3 in positively buckled π-bonded chain [V_{bias} = -1.0 V; I_t = 0.4 nA; T = 8 K].
(c+d) Single dI/dV spectra of P-atom (black), next to P-atom (yellow), and of the free surface (blue).
(e+f) Spatial profiles of the dI/dV(x,y,V) data set along chain with P-atom [Set-point: (c+e) V_{bias} = +0.5 V; I_t = 0.1 nA; T = 6 K; (d+f) V_{bias} = -1.0 V; I_t = 0.4 nA; T = 8 K].

in relation to E_F and thus to the SCB minimum. The reduction of LDOS is found at -0.7 V. The energetic position of the LDOS reduction is below the upper edge of the SVB for both buckling types.

Figure 6.8e+f shows a spatial profiles of the dI/dV(x,y,V) data sets along a π-bonded chain with an pushed up P atom on site 2 (e) and a P atom on site 3 (f). The spectroscopic signature at -0.25 V is extended on a length of about 8 nm with a smooth transition between the signature of the P atom and that of the free π-bonded chain, similar to the topographic contrast at low negative voltages for both buckling types. This elongation confirms that the signature is not caused by

the defect states of the P atom itself, as these are highly localised. The origin of this signature will be discussed in more detail after the introduction of P induced signatures under different conditions (long π-bonded chains, subsurface P atoms).

The high resolution of the spatial profile of the lock-in dI/dV data set in figure 6.8e offers the possibility to investigate the positions of the LDOS maxima at different voltages with respect to the lattice. According to Garleff *et al.* [19], in undisturbed π-bonded chains the LDOS maximum is located at the 'up'-atom for all negative voltages and for positive voltages above +0.2 V. At low positive voltages, the available states are in the SCB and are located at the 'down'-atom [19]. This can be seen in the spatial profile of a dI/dV(x,y,V) data set along a π-bonded chain with a P atom on site 2 in the pushed up reconstruction for positions more than 4 nm from the P atom site. At positive voltages between 0.10 V and 0.15 V, the LDOS maxima are shifted by half a unit cell with respect to the positions at negative or high positive voltages of more than +0.40 V. At the site of the P atom these LDOS maxima are displaced by half a unit cell away from the P atom toward the adjacent 'up'-atoms. This displacement is getting smaller with increasing distance from the P atom until at a distance of 4 nm the LDOS maxima at +0.1 V are positioned at the 'down'-atom site again (Fig. 6.8e). The LDOS maxima at higher positive voltages, positioned at 'up'-atom sites, show no such shift. This indicates that the shift is not caused by different positions of 'up'- and 'down'-atoms which could be induced due to strain at the P atom site, but assumedly by the upward buckling of just the P-atom. This alters the bonding configuration and can influence the electronic structure.

6.2 Phosphorus atoms in quasi-infinite π-bonded chains

Up to now, all investigations were performed in relatively small domains, resulting in lengths of the π-bonded chains between 10 to 100 nm. One reason for this is the fact that the preparation of surface areas without steps or domain boundaries is difficult, and even with an improved technique chance plays an important role. Figure 6.9 shows large scale images of different surface structures. In areas with very high step density the π-bonded chains are too short (<10 nm) for analysis as no assignment of signatures to their origin is possible (Fig. 6.9a). In areas with broader terraces, the length of the π-bonded chains strongly depends on the cleavage direction. For cleavage in $(\bar{1}10)$-direction, the chains are parallel to the long step edges, thus chain lengths of a few hundred nanometres are possible (Fig. 6.9b), but the resulting domains are strongly influ-

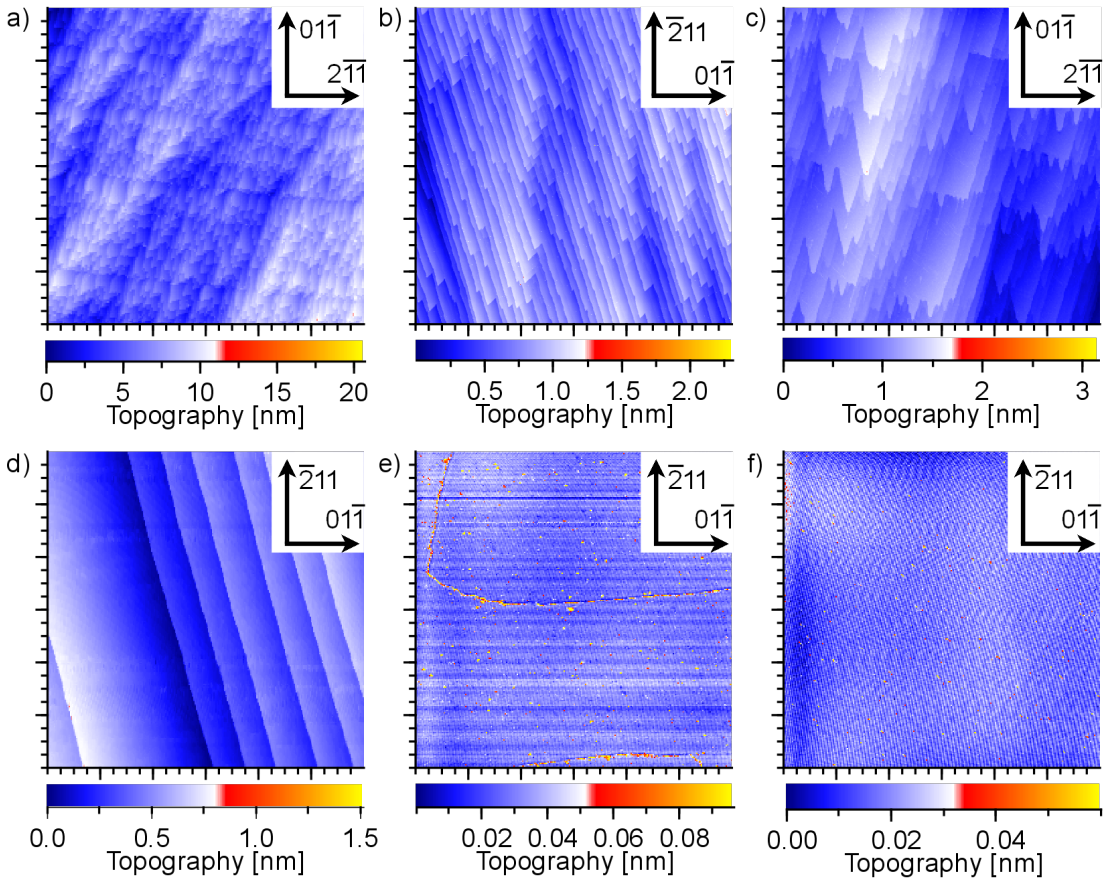

Figure 6.9: *Different surface structures [600 nm×600 nm; V_{bias} = -2.0 V ; I_t = 0.1 nA; T = 5.6 K]:*
(a) Area with very high step density.
(b) Area with broader terraces, cleavage in ($\bar{1}10$)-direction.
(c) Area with broader terraces, cleavage in ($\bar{2}11$)-direction.
(d) Area with few steps.
(e) Flat area with two domain boundaries.
(f) Area without steps or domain boundaries.

enced by their small width. Cleavage in ($\bar{2}11$)-direction results in chains which run in an angle toward the step edges, and thus the π-bonded chains are much shorter (Fig. 6.9c). Areas with few surface steps allow the investigation of long π-bonded chains in large domains (Fig. 6.9d) and in areas without surface steps (Fig. 6.9e+f) only the presence of domain boundaries might influence the chain length.

In this section, large areas without surface steps or domain boundaries are investigated (Fig. 6.9f). The size of the domains exceeds several μm^2, controlled by executing larger movements ($\approx$ 0.5 μm) of the scan head and performing

a quick examination of the largest possible scan area (600 nm×600 nm). Due to the higher contrast domain boundaries and adsorbates are clearly visible even in large scans (Fig. 6.9e). All large domains investigated in this section are positively buckled.

The signature of P atoms in topography images at different surface sites is the same in long π-bonded chains as in shorter ones for -1.0 V and -0.5 V (Fig. 6.10 (long chains) and 6.5(short chains)), but the spectroscopic signature (Fig. 6.11) differs significantly from that described by J. K. Garleff [68] and also from the signature found for P atoms in negatively buckled π-bonded chains. The dI/dV signature of P atoms in shorter π-bonded chains shows a cigar-shaped enhancement in the spatial profile of the dI/dV(x,y,V) data set with a length of ∼10 nm, corresponding to the contrast pattern at -0.5 V, and the maximum at -0.25 V (Fig. 6.8).

In contrast to this, Fig. 6.11 shows signatures of P atoms located in quasi-infinite π-bonded chains. The data was obtained by a dI/dV(x,y,V) measurement via lock-in technique. The topography images at -0.5 V show signatures of P atoms in the surface layer, one at site 1 (Fig. 6.11a) and the other at site 3 (Fig. 6.11b). In contrast to P atoms in shorter chains, where the maximum of the dI/dV signature is always found deep in the surface band gap, the maximum is located at -0.10 V for P atoms on site 1 and 3 in long chains (Fig. 6.11c+d+f). Figures 6.11e+g show the spatial profiles of the dI/dV data set (d+f) after subtraction of an average spectrum of the free surface. At the position of the P atom, the additional signal is reduced for positive voltages lower than +0.2 V and all negative voltages in the range of the measurement. The main difference between the signatures of a P atom on site 1 vs. site 3 is that at site 1, there is a voltage range of ∼100 mV where the dI/dV signal is decreased compared to the free surface around zero bias voltage for positive and negative voltages. This suggests that the LDOS decrease around zero bias is caused by the structural change due to the P atom located in the π-bonded chain and not a general feature of P atoms in Si(111)-2× 1. In addition, all features are a bit weaker for site 3.

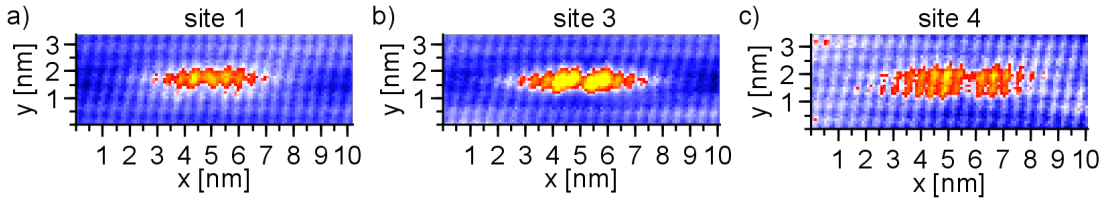

Figure 6.10: *P atoms in the surface layer of a large free area [V_{bias} = -0.5 V; I_t = 0.1 nA; T = 5.6 K]: (a) Site 1, (b) site 3, (c) site 4.*

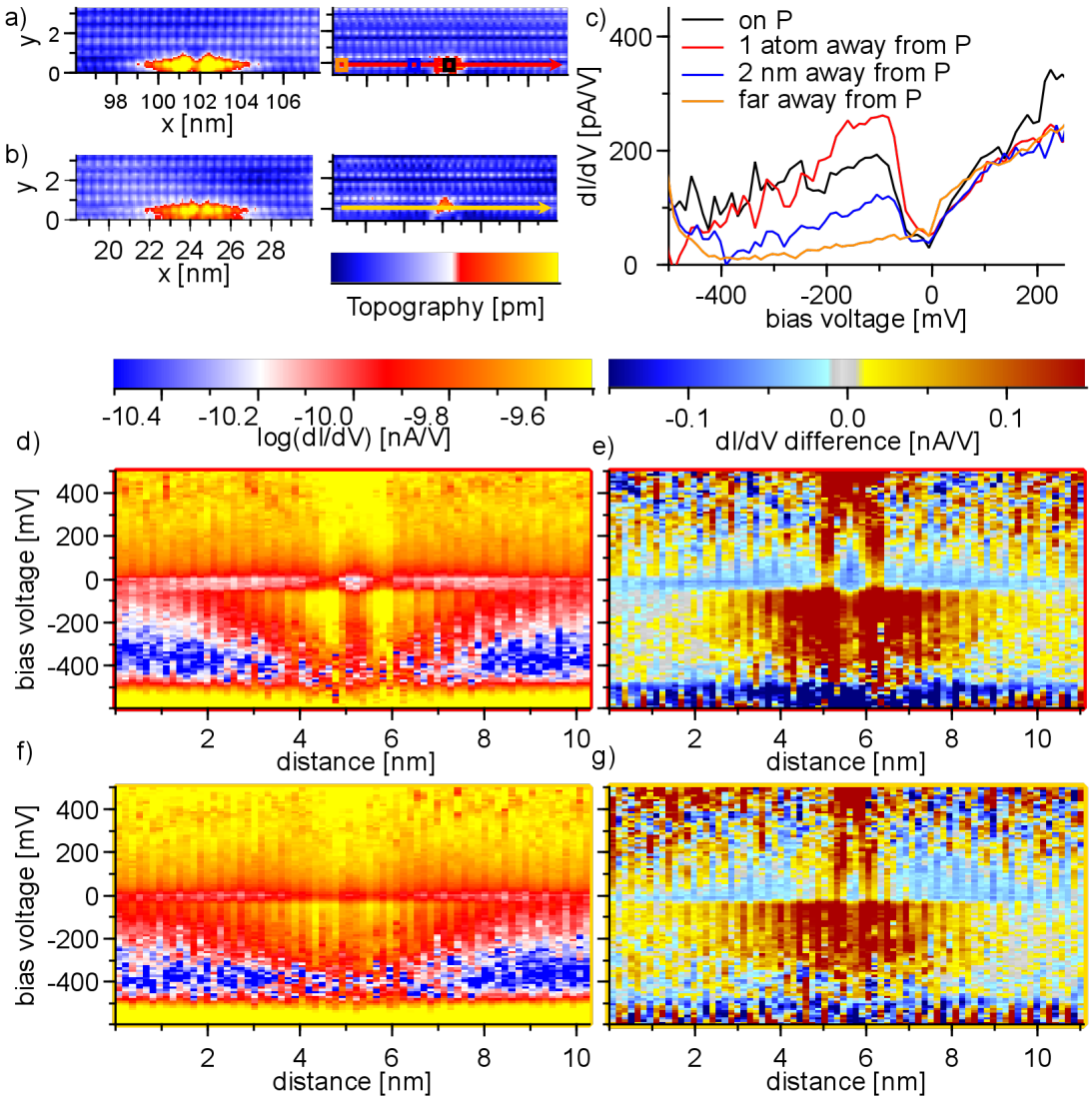

Figure 6.11: *dI/dV measurement of P atoms in long π-bonded chains.*
(a+b) Topography images showing signatures of P atoms on site 1 (a) and site 3 (b). Left side – topography image of P induced contrast [V_{bias} = -0.5 V; I_t = 0.1 nA; T = 5.6 K], right side – topography image at the stabilization setpoint of the dI/dV measurement (black, red, blue, and orange squares mark positions of single dI/dV spectra (c) and yellow and red lines mark the positions of the spatial profiles of the dI/dV(x,y,V) data set (d+e).) [V_{bias} = +0.5 V ; I_t = 0.1 nA; T = 5.6 K].
(c) Single dI/dV spectra on the P atom site (black), on neighbouring atom (red), 2 nm away from P atom (blue), and far away from P atom (orange).
(d+e) Spatial profile of the dI/dV(x,y,V) data set (d) and after subtraction of an average spectrum (e) of a P atom on site 1 (yellow line in a).
(f+g) Spatial profile of the dI/dV(x,y,V) data set (f) and after subtraction of an average spectrum (g) of a P atom on site 3 (red line in b).

The increase of the dI/dV signal at low voltages is very sharp while the decrease is gradual, resulting in a signature which is asymmetric concerning the voltage dependence but symmetric in distance from the P atom (Fig. 6.11c). Figures 6.11e+g show that the change induced by the presence of P atoms is a significant increase of LDOS signal at the lower edge of the SCB and below the SCB at a length of about 7-8 nm in π-bonded chain direction while the LDOS signal in the SCB above E_F is decreased. These signatures stunningly resemble the spectroscopic signature of bound states caused by single metal atoms on 2D metal surfaces [75,76] or impurities in a 2D-metal [77,78]. The attractive potential of the adatom or impurity results in a bound state which is split off from the bottom of the SCB and energetically lies just below the SCB. The interpretation of the P induced signature as a bound state will be resumed in more detail after the consideration of signatures induced by subsurface P atoms.

6.3 Phosphorus in subsurface layers

Large scale multi-bias measurements (200 nm$\times$200 nm) with atomic resolution reveal additional signatures to those of P atoms in the surface layer (Fig. 6.12). These signatures show the same voltage dependence as the substitutional P atoms in the surface but they are weaker and spread out over several adjacent π-bonded chains. The length of the contrasts in π-bonded chain direction at -0.5 V is $\sim$10 nm for all signatures. At a voltage of +1.0 V, these signatures strongly resemble the contrast pattern of subsurface Sb atoms beneath Si(111)-2$\times$1 as described by P. Studer [42]. This indicates that the signatures might be interpreted as P atoms in subsurface layers.

Statistical analysis of the multi-bias images gives a count of the different signatures. The resolution of the images is just at the limit to resolve atoms which, in some cases, is to inaccurate for an exact determination of the P site of the atoms within the surface. There are 76 adsorbates, 56 signatures of pushed-up P atoms at site 4, 11 P atoms on site 1, 34 P atoms on site 3, 33 P atoms on site 4, and 20 P atoms located in the surface layer but without definite assignment to a surface site. All together there are $\sim$145 P atoms in the surface layer in the investigated area of 200 nm$\times$200 nm (black circles in Fig. 6.12). This is more than the 100 P atoms one would expect for the nominal doping level of the sample of $6\cdot10^{18}$ cm^{-3} Si crystal. Thus the real doping level of this sample region is presumably higher than the nominal on of the Si crystal. An estimate is a real doping level of $1.15\cdot10^{19}$ cm^{-3}.

Concerning the signatures of subsurface P atoms, one can distinguish three slightly different contrast types and assign them to three subsurface layers. In

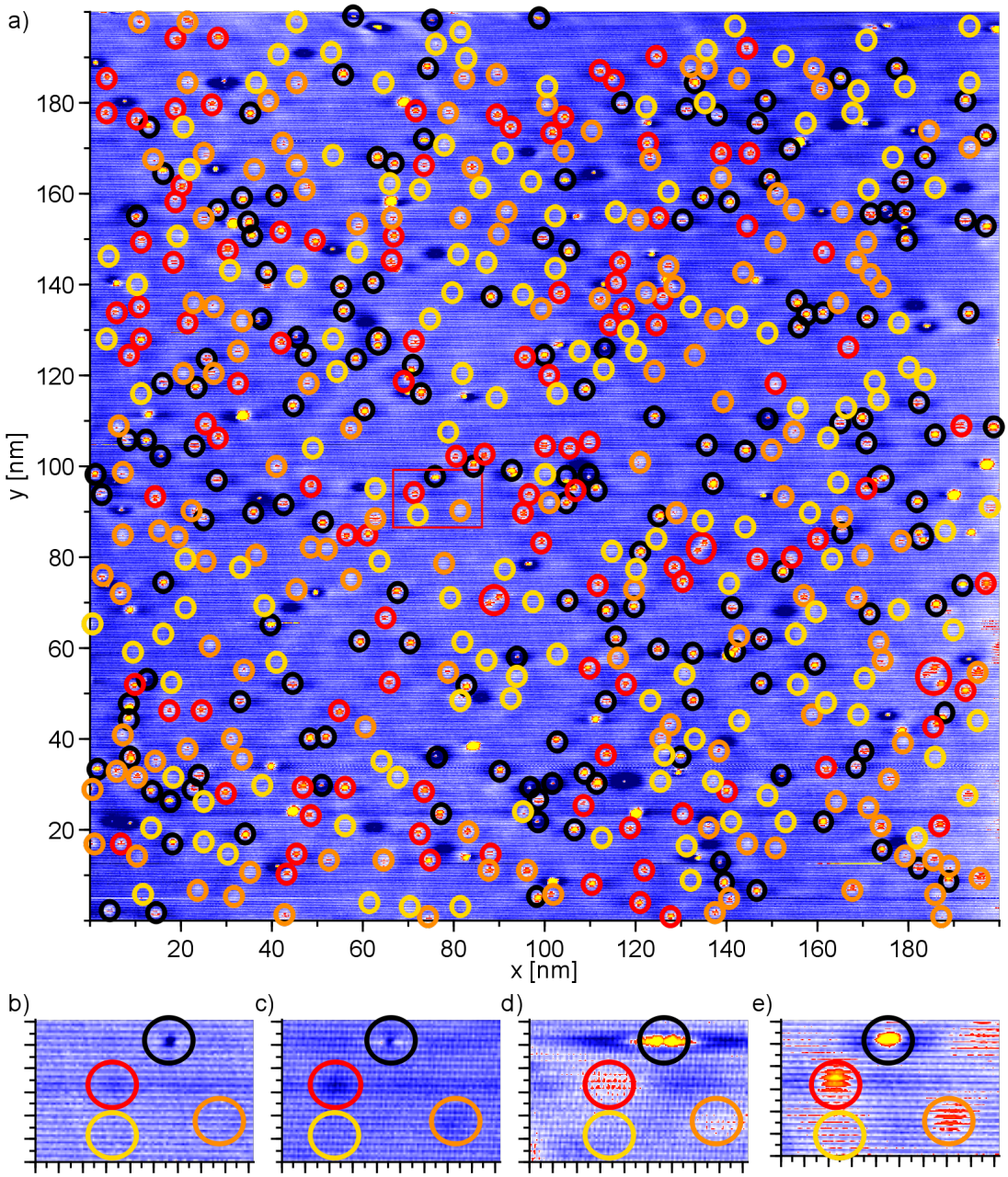

Figure 6.12: *Topography images from a 200 nm×200 nm multi-bias data set with atomic resolution (black circles - P atoms in surface layer, red circles - P atoms in first subsurface layer, orange circles - P atoms in second subsurface layer, yellow circles - P atoms in third subsurface layer) [I_t = 0.1 nA; T = 5.6 K]:*
(a) Whole image at V_{bias} = +1.0 V. Red rectangle marks position of zoomed area. (b-e) Enlarged area with P atoms in the four different layers: (b) V_{bias} = -2.0 V, (c) V_{bias} = -1.0 V, (d) V_{bias} = -0.5 V, (e) V_{bias} = +1.0 V.(The entire topography images for all bias voltages may be found in chapter Appendix)

the first layer beneath the surface, P atoms show as a slight indention at -2.0 V (in contrast to the distinct indention at surface sites) and an elongated contrast at -0.5 V, which is restricted to one to three π-bonded chains. In some cases, a depression above the P site is visible, similar to the signatures of P atoms in the surface layer. At +1.0 V the protrusion is weaker and less localised than for surface P atoms but it is still very distinct (red circles in Fig. 6.12).

The signature of second layer subsurface P atoms may only be guessed at -2.0 V while it is still well visible at-0.5 V and +1.0 V. In comparison to first layer subsurface P atoms the signatures are again fainter and less localised (orange circles in Fig. 6.12).

The third type of signature, assigned to P atoms located three layers beneath the surface, shows as a slight, spread out protrusion at -0.5 V and +1.0 V. At -0.5 V this protrusion is still elongated with a length of $\sim$10 nm in direction along the π-bonded chains (yellow circles in Fig. 6.12).

The count of these three signatures confirms the assignment to the three subsurface layers as there are 125 of the first, 140 of the second, and 144 of the third kind of signature.

Figure 6.13 shows data of a lock-in dI/dV(x,y,V) measurement which allows the comparison of the spectroscopic signature of two P atoms in different layers beneath the surface to the signature of a P atom on site 3 within the surface. The topography image at -0.5 V (Fig. 6.13a) shows the distinct signature of the surface P atom at the right side of the image and two different subsurface signatures. At the left side, there is a weak signature, in the middle a more distinct contrast enhancement. Figure 6.13c shows a spatial profile of the dI/dV(x,y,V) data set resolving the spectral signatures of the P atom in the surface layer and the two subsurface P atoms. While the surface P atom induces a maximum LDOS at -60 mV, the LDOS maximum is at -30 mV and there is no signal reduction at the site of the P atom in the spectroscopic signature of the two subsurface P atoms (Fig. 6.13e). The spatial profile of the dI/dV data set after subtraction of an average profile without P signature (Fig. 6.13d) shows that the LDOS increase in the SCB below E_F is mirrored by an LDOS decrease in the SCB above E_F. The energetic position of the LDOS maximum for subsurface P atoms is well within the SCB in contrast to P atoms in the surface layer, where the maximum is at the bottom of the SCB. In accordance with the interpretation of the surface P atom signature as localised bound state split off from the bottom of the SCB, the signature of subsurface P atom is interpreted to be caused by a localised resonance in the SCB which will be described in more detail in section 6.4. Except for a lower intensity of the LDOS signal at the P atom in the deeper subsurface layer, there is no difference in the spectroscopic signature of P atoms in different subsurface layers.

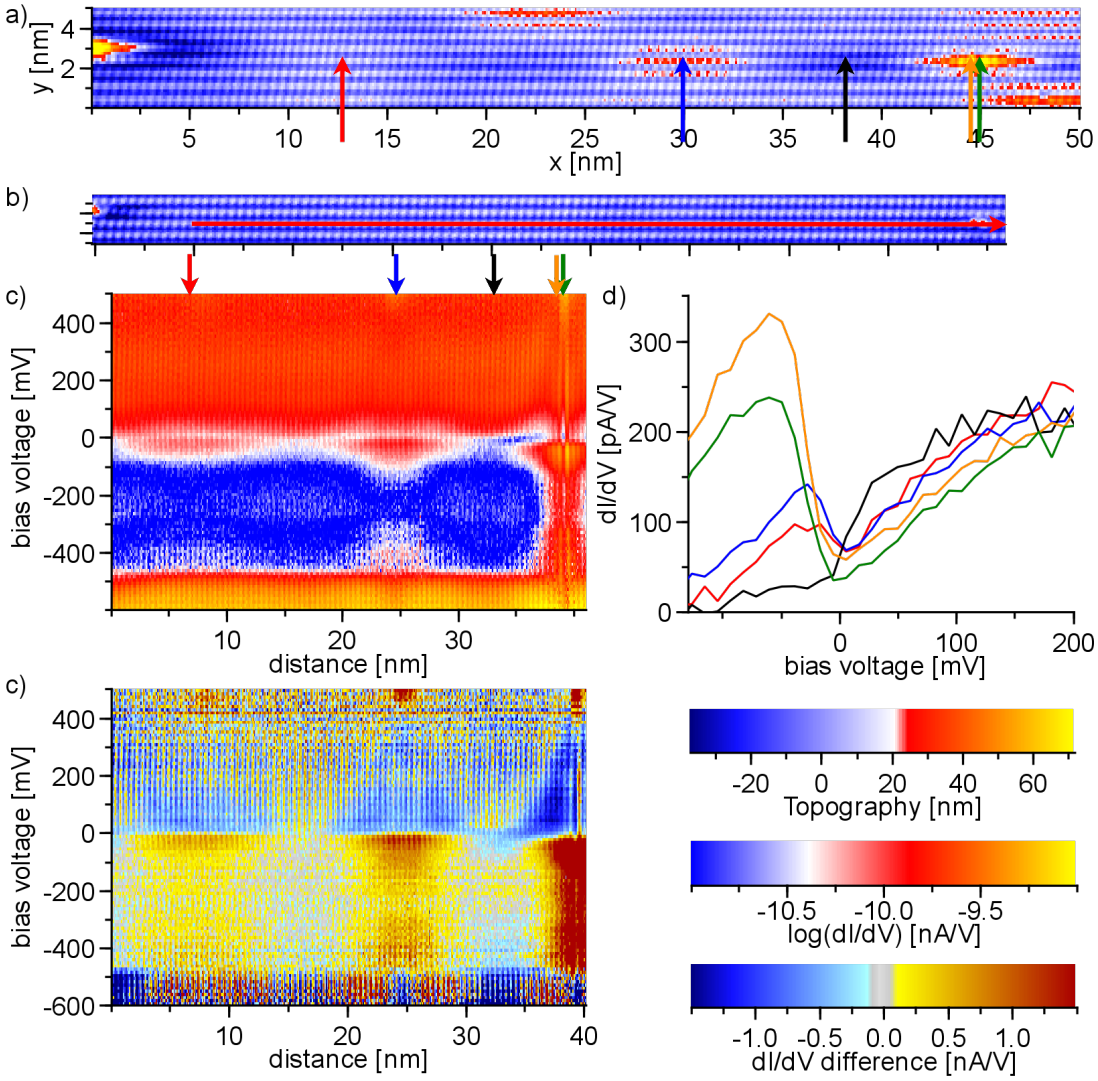

Figure 6.13: *dI/dV measurement of one P atom in the surface layer next to two subsurface P atoms:*
(a) Topography image showing two signatures of subsurface P atoms and one signature of a P atom on site 3 [V_{bias} = -0.5 V; I_t = 0.1 nA; T = 5.6 K].
(b) Topography image at the stabilisation setpoint of the dI/dV measurement (red line marks the position of the spatial profile of the dI/dV(x,y,V) data set (c)) [V_{bias} = +0.5 V ; I_t = 0.1 nA; T = 5.6 K].
(c+d) spatial profile of the dI/dV(x,y,V) data set (c) and after subtraction of an average spectrum (d) along the π-bonded chain with the three P signatures.
(e) Single dI/dV spectra at the positions marked by the black (position without additional features), red (subsurface P atom in deeper layer), blue (subsurface P atom in high layer), orange (atom next to surface P atom), and green arrows (surface P atom at site 1).

In between the P signatures, the LDOS in the surface band gap is vanishing slowly without a gap at zero bias voltage. This shows that the subsurface P atoms do not electronically cut the π-bonded chains, in contrast to P atoms at surface sites [41]. This also shows that the reduced LDOS at the P signatures is not due to a Coulomb gap as it is found in short π-bonded chains.

6.3.1 Charge state

In contrast to the substitutional P atoms at surface sites, which are in a neutral charge state [68, 79], P atoms in the 9 nm deep space charge layer are ionised and thus have a positive charge. While the contrast patterns at $\pm$1.0 V and -2.0 V agree with the expected signature of a screened positive charge [42], the elongated protrusion at -0.5 V is harder to explain.

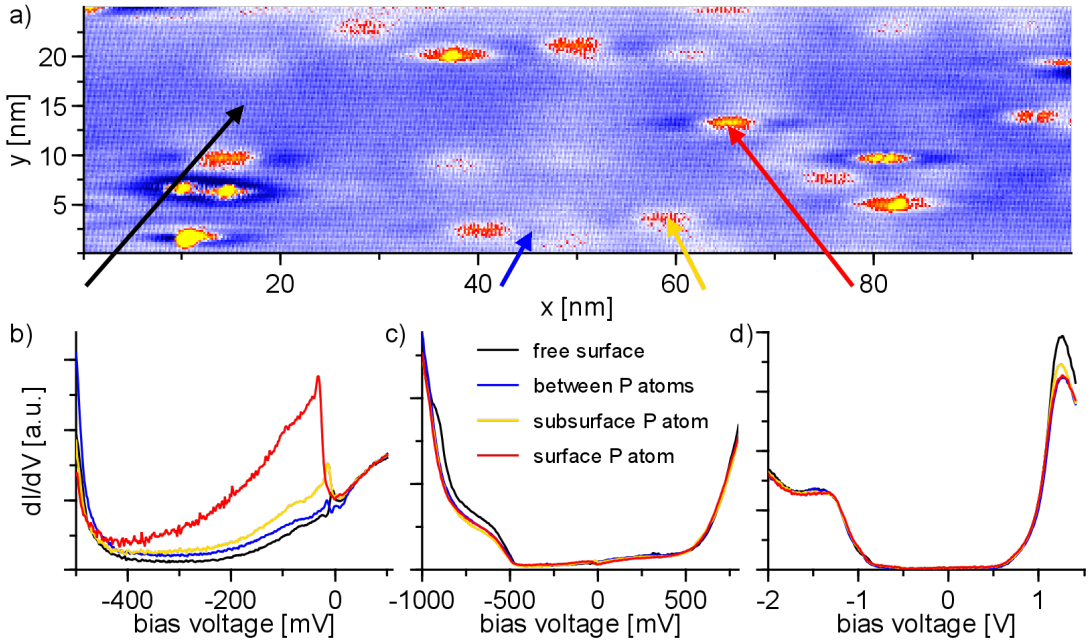

Figure 6.14: *Spectroscopic signature of free surface (black), indented position near P atom (blue), subsurface P atoms (yellow), and P atoms at surface sites (red):*
(a) Topography image (arrows mark positions of dI/dV spectra) [V_{bias} = -0.5 V ; I_t = 0.1 nA; T = 5.6 K].
(b) dI/dV spectra in the voltage range of the surface band gap.
(c) dI/dV spectra in the voltage range of the bulk band gap.
(d) dI/dV spectra including peaks from the bulk bands.

First of all, one would assume the signature of a Coulomb potential to exhibit an isotropic dependence on distance to the charge resulting in a disk-like contrast as found for Sb and Bi in Si(111)-2×1 [42] and also for ionised donors in GaAs [80, 81].

The charge state of different sample positions can be compared by considering their spectral signatures. An additional, localised charge changes the position of E_F in the surface bands. In our measurements, this would be observable as a shift of the energetic positions of all dI/dV signatures as the sample is assumed to be in equilibrium and E_F constant. In figure 6.14, spectroscopic signatures of free surface, P atoms in the surface layer, subsurface P atoms, and positions with a slight indention in the vicinity of P atoms are compared for the voltage regions of gap states, surface bands, and bulk bands. The spectroscopic signature of subsurface P atoms is similar to that of P atoms in the surface for all measured voltage ranges (Fig. 6.14b-d). The main difference is the height of the distinctive dI/dV signature in the surface band gap which is larger for P atoms in the surface layer. Although the peak intensity of the peak at +1.25 V is decreased for all signatures near or above a P atom, there is no peak shift for bulk or surface bands compared to the free surface which would be expected for a charged defect. This indicates that either the charge of the ionised P atoms is effectively screened by the metallic surface or that the binding energy of P atoms in the first subsurface layers is enhanced, resulting in a neutral charge state as for the surface P atoms.

The effect of screening of the positive charge might be estimated by applying the *mirror charge model*. In this model, the effect of a positive charge in front of a metal plate at distance z_0 is described by assuming a second, negative charge behind the metal plate at distance -z_0 (Fig. 6.15a). According to [82] the induced charge density $\rho(d)$ in the metal plate is:

$$\rho(d) = \frac{\epsilon\epsilon_0 \Delta F}{\Delta F}\left(-\frac{2q\, z_0}{4\pi\epsilon\epsilon_0\sqrt{z_0^2+d^2}^3}\right) = -\frac{q\, z_0}{2\pi\sqrt{z_0^2+d^2}^3} \tag{6.1}$$

with: $d = \sqrt{z_0^2+d^2}$

: distance in the plane of the metal plate

$\epsilon\epsilon_0$: dielectric constant

ΔF : small area of metal plate

q : charge

z_0 : distance between charge and metal plate

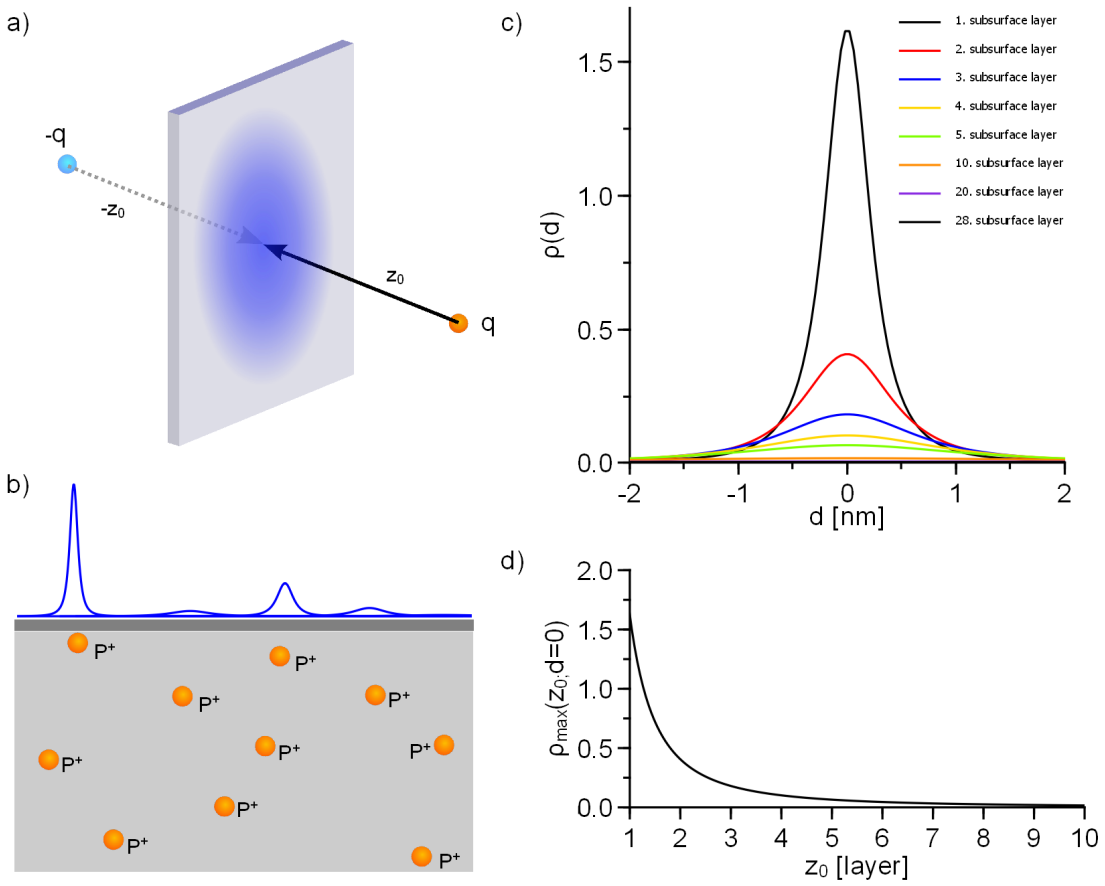

Figure 6.15: *Mirror-charge model:*
(a) Single charge q in front of a metal plate with distance z_0.
(b) Ionised P atoms beneath Si(111)-2×1.
(c) Distribution of induced charge density ρ(d) for different for P atoms in different subsurface layer, according to the mirror-charge model.
(d) Decrease of ρ_{max}(d=0,z_0) for increasing distance z_0 between charge and metal plate.

The situation of the charged P atoms beneath the metallic Si(111)-2×1 surface is comparable, as the P atoms in the space charge layer are surrounded by a dielectricum without free charge carriers (Fig. 6.15b). Figure 6.15c shows the amount and distribution of the induced negative charge in the surface layer for ionised P atoms in several subsurface layers. The maximum charge density is quickly decreasing, and the induced charge is located in larger areas for increasing z_0. Thus, a visible effect is expected only for P atoms located in a few upper layers which is in very good agreement with the results of the count of different signatures. Within the mirror-charge model, the impact of the screening charge is restricted on two π-bonded chains for the first layer and growing more

spread out for lower layers, in accordance with the measured signatures at -2.0 V and $\pm$1.0 V.

These length scales only explain the extend of signatures at high voltages and for -0.5 V the width of the signatures perpendicular to the chains, but not the longer length scale in direction parallel to the π-bonded chains. One explanation could be that the surface area necessary to provide the charge of one electron is larger than the extend of the calculated charge density, as the Si(111)-2$\times$1 surface is no ideal metal with infinite electron density. The additional electrons of all P atoms in the 9 nm wide space charge layer fill SCB states. According to:

$$N_{e^-\text{-SCB}} = n_P \cdot \Delta V \tag{6.2}$$

$$= 1 \cdot 10^{19}\text{cm}^{-3} \cdot 9\text{nm} \cdot 0.665\text{nm} \cdot 0.384\text{nm} = 0.023 \tag{6.3}$$

with: n_P : doping level

there are $N_{e^-\text{-SCB}} = 0.023$ elemental charges per surface unit cell. Thus, $\sim$50 unit cells are necessary to screen one ionized P atom. This corresponds to a length of 19.2 nm if only one π-bonded chain is affected, 9.6 nm for two and 6.4 nm for three involved π-bonded chains. The strong dependence on the number of π-bonded chains excludes the induced screening charge as explanation for the anisotropy of the signatures at -0.5 V because they all have the same length of $\sim$10 nm.

At voltages between E_F and the SVB edge, electrons tunnelling out of the filled states of the SCB provide the main contribution to the tunnelling current. Figure 6.17a shows the DOS for the two surface states [83]. A summation of the DOS of the SCB up to 0.023 e^- per unit cell results in a band filling of 69 meV.

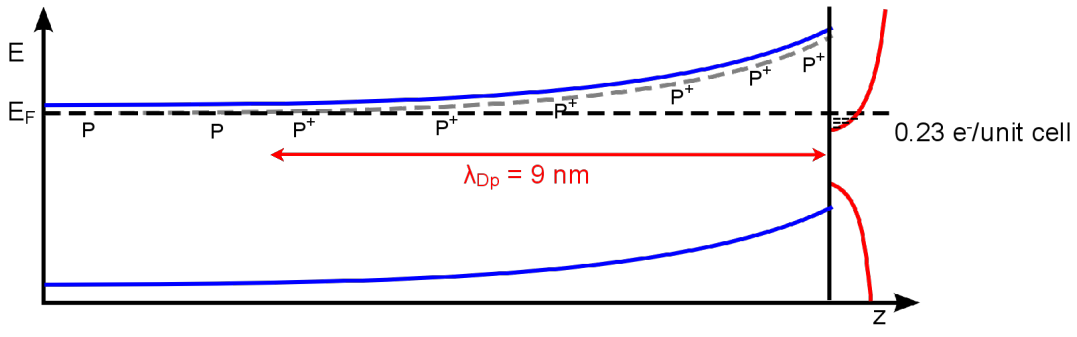

Figure 6.16: *Electrons from the ionised P atoms in the 9 nm deep space charge layer fill the SCB with 0.23e^- per unit cell.*

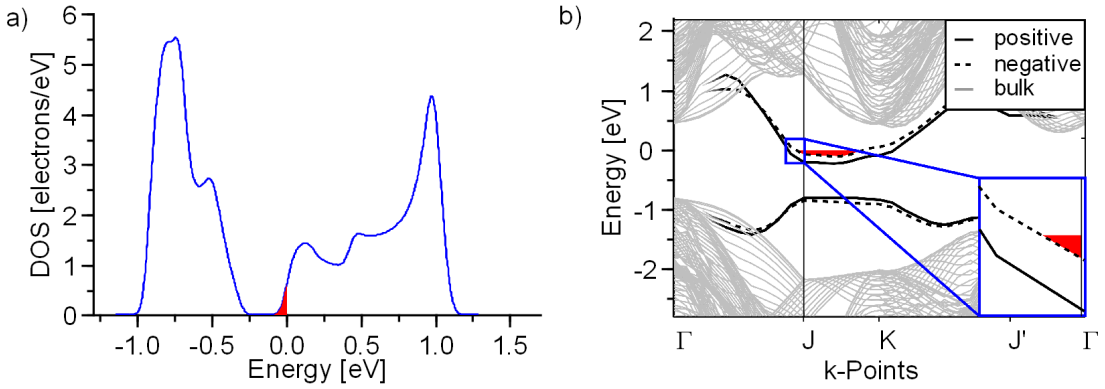

Figure 6.17: *Filling of the SCB with electrons from P atoms in the space charge layer (red):*
(a) DOS of the surface bands [83].
(b) electronic surface dispersion of Si(111)-2×1 [31].

The dispersion of the SCB in π-bonded chain direction is high, confining the electrons to $k_{||} = 0.052\frac{\pi}{a} = 0.43\,\mathrm{nm}^{-1}$ for this small band filling (Fig. 6.17b). This corresponds to a wave length $\lambda_{||} = 7.4\,\mathrm{nm}$. Perpendicular to the π-bonded chains there is nearly no dispersion, allowing for small wavelengths.

According to these considerations, the surface band structure must be taken into account in order to explain the anisotropic contrast at -0.5 V, as well as the localized, isotropic signatures at $\pm$1.0 V and -2.0 V. The positive charges of the P ions in the space charge layer induce a negative screening charge in the surface layer. As the minimal wavelength of electrons at E_F (Fermi wavelength (λ_F)) is λ_F=7.4 nm in ($\bar{2}11$)-direction (parallel to the π-bonded chains), the additional charge is not distributed isotropically but elongated along the chains for electrons tunnelling out of filled SCB states.

6.4 P atoms induce bound states

Bound states occur when the attractive potential of a defect (adatom or impurity) leads to a strong localisation of charge carriers in a system of otherwise delocalised charge carriers, resulting in a reduction of the total energy of the combined system. The formation of such states was observed for single metal adatoms on 2-dimensional metal surfaces [75, 76] and also for impurities in a 2D-metal [77, 78]. Figure 6.18a shows dI/dV spectra of single Ag and Co adatoms on Ag(111) investigated by Limot *et al.*. The upper spectrum was taken on a free Ag(111) surface, and the main feature is the step-like onset of the surface state band. In the two lower spectra, taken directly above single

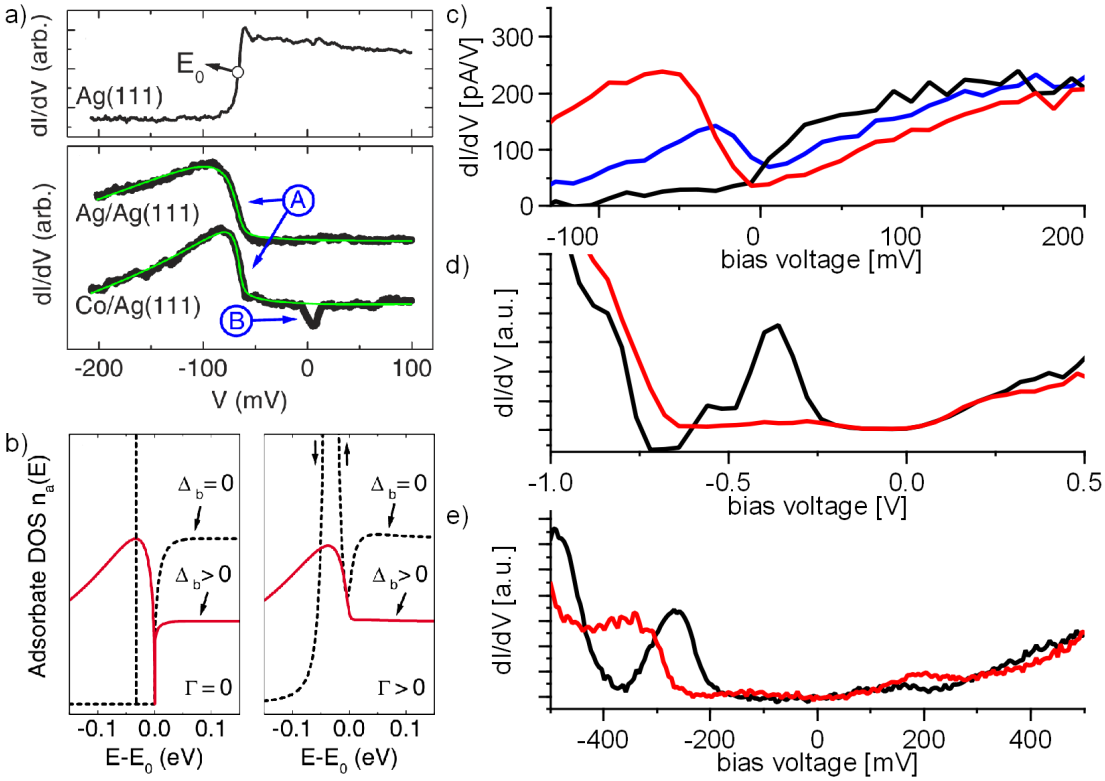

Figure 6.18: *(a) Single dI/dV spectra at a free silver (Ag)(111) area (upper spectrum) and at single Ag and cobalt (Co) adatoms on Ag(111) [75].*
(b) Modelled adatom DOS interacting with a surface-state DOS - right image including lifetime effects: dashed lines – without coupling to bulk states; solid lines – with coupling to bulk states [75].
(c) Single dI/dV spectra at a surface P atom at site 1 (red), at a subsurface P atom (blue), and at a position without additional features (black) in quasi-free π-bonded chains [V_{bias} = -0.5 V ; I_t = 0.1 nA; T = 5.6 K].
(d+e) Single dI/dV spectra of a P atom (black) and the free surface (blue) in domains with positive (d) and negative (e) buckling type [Setpoint: (d) V_{bias} = -1.0 V; I_t = 0.4 nA; T = 8 K; (e) V_{bias} = +0.5 V; I_t = 0.1 nA; T = 6 K].

Ag and Co adatoms, this step-like feature is suppressed. Instead a new peak directly below the surface state with a steep onset near the SCB minimum and a gradual decrease to lower energies appears. Limot *et al.* exclude magnetic effects and atomic orbitals of the adsorbates as potential origins of the new state. They conclude that the coupling of an energy level of the single adsorbate atoms to the SCB results in a bound state directly beneath the lower edge of the surface-state conduction band. This explanation is confirmed by modelling the interaction between a single adsorbate level and bulk and surface states (Fig. 6.18b). The result is an adsorbate DOS n_a(E) which is in excellent agreement with their measurements [75].

There is also an excellent agreement of these measurements and calculations with the single dI/dV spectra of P atoms at surface sites in free π-bonded chains (red line in Fig. 6.18c). The DOS of the SCB is decreased near the lower band edge, and below the SCB minimum a new, localised state occurs. As the only condition for the appearance of such a bound state is the coupling of an energy level of the adsorbate or impurity to the SCB [75], this description may well be applied to a P atom, which leads to a localised potential in the metallic Si(111)-2$\times$1 surface.

The coupling of the potential of a P atom in a subsurface layer to the surface state is weaker, and instead of a split-off bound state a localised resonance appears in the lower part of the SCB (blue line in Fig. 6.18c). These resonances occur if there is an attractive potential coupled to a metallic surface which is not strong enough to cause a bound state but nevertheless localises the electrons near the impurity in the conduction band. This is caused by resonant scattering of electrons at the impurity [84].

The signatures induced by P atoms located at surface sites in shorter π-bonded chains (l$\approx$20-50 nm) may also be interpreted as split-off, localised bound state, but in this case the bound state is split-off from the SVB instead of the SCB for positive as well as negative buckling of the π-bonded chains (Fig. 6.18d+e). In the case of short π-bonded chains the surface states are significantly influenced by different kinds of surface defects, e.g. step edges, domain boundaries and adsorbates. The Coulomb gap which is found at E_F for shorter π-bonded chains [41] results in a lack of available SCB states near the SCB edge, and thus it prevents the coupling between the attractive potential of the P atom and the SCB. Instead of a donator-like bound state near the SCB an acceptor-like bound state near the SVB appears.The effect of a coupling between the attractive potential of the P atom and the SVB is comparable to the coupling to the SCB, as already observed and calculated for impurities in a 2D metal [78]. The reason for the identical spatial extend of the donator- and acceptor-like bound states, especially in direction parallel to the π-bonded chains, lies in the 'mirrored' dispersion of SCB and SVB at their minimum, respectively maximum, at the k-point $\bar{J}$.

6.5 Influence of P atoms on each other

When a many-particle system becomes denser, correlations between adjacent particles get stronger. There are many different consequences which may result therefrom, e.g. contrast patterns which may no longer be described as a simple superposition of two single particle contrast patterns or changes in the energetic positions of defect induced states. In order to consider potential correlations

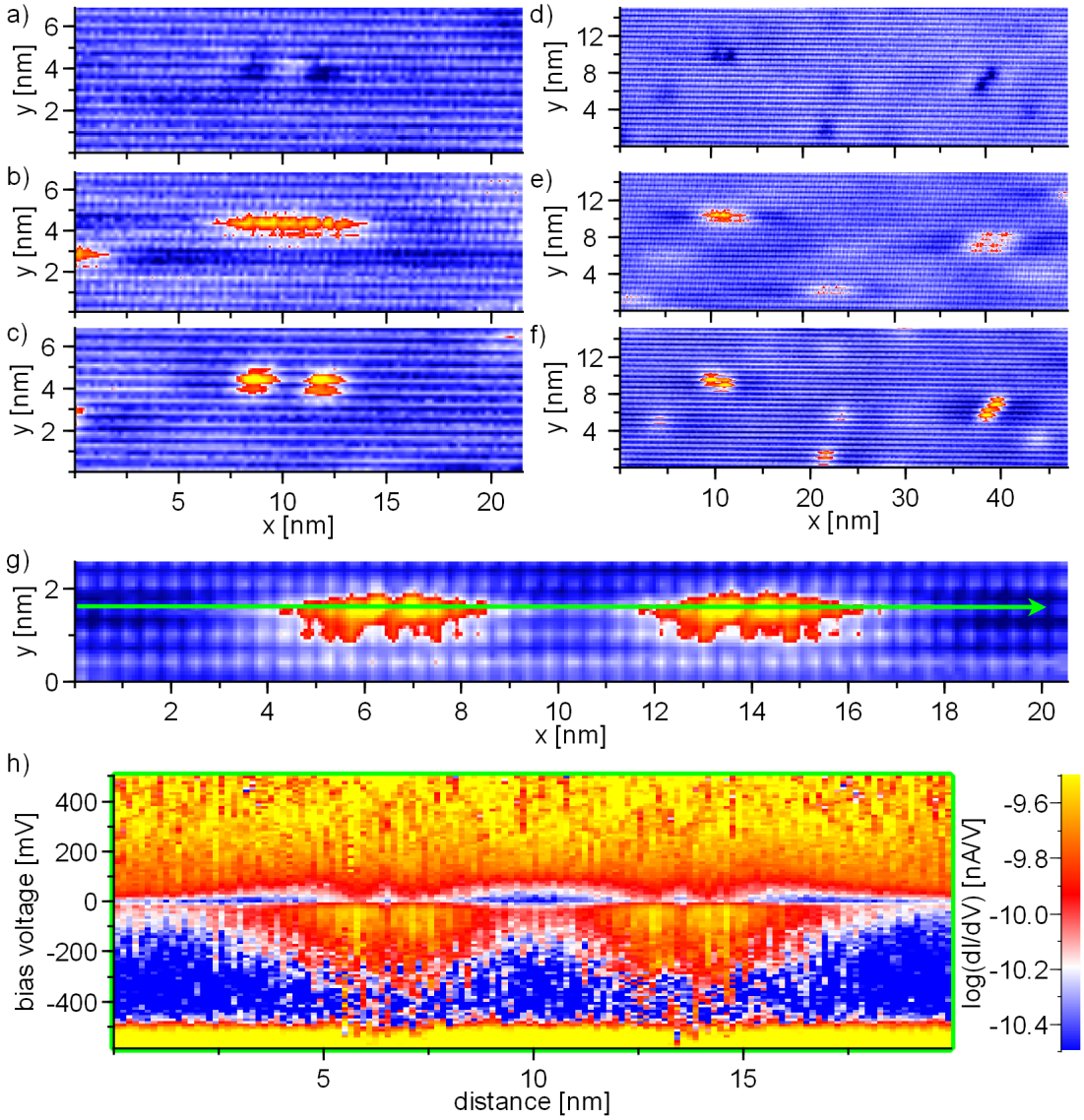

Figure 6.19: *(a-c) P atoms at site 1 or site 3 in the same π-bonded chain with a distance of less than 5 nm at V_{bias} = -1.0 V (a), V_{bias} = -0.5 V (b), and V_{bias} = +1.0 V (c) [I_t = 0.1 nA; T = 5.6 K].*
(d-f) P atoms at site 1 and site 4 in the same π-bonded chain with a distance of less than 5 nm (upper left side) and in different π-bonded chains above each other with one empty π-bonded chain in between at V_{bias} = -1.0 V (d), V_{bias} = -0.5 V (e), and V_{bias} = +1.0 V (f) [I_t = 0.1 nA; T = 5.6 K].
(g+h) dI/dV measurement of two P atoms at site 3 in a distance of less than 7 nm: (g) Topography image (green line – position of the spatial profile of the dI/dV(x,y,V) data set (h)) [V_{bias} = -0.5 V (left image); I_t = 0.1 nA; T = 5.6 K].
(h) Spatial profile of the dI/dV(x,y,V) data set (green line in g).

between P atoms in the surface layer and also below the surface, the positioning of signatures relative to each other is investigated. Special attention is on P atoms with low distances along π-bonded chains as the long Fermi wavelength in π-bonded chain direction may have an effect.

At first, two P atoms in the surface layer are considered. Topography images show no lower limit to the distance between surface atoms, neither in the same π-bonded chain nor in two neighbouring chains (Fig. 6.19a-f), and the resulting contrast pattern is a superposition of two single contrasts. This indicates that the signatures of P atoms in the surface layer are independent of each other. An investigation of the spectroscopic signature of two P atoms in the same π-bonded chain at a distance of 7 nm (Fig. 6.19g+h) supports this assumption. The P atoms are both positioned at site 3 in the surface layer, and a comparison with the signature of a single site 3 P atom (6.11), obtained during the same measurement without any tip change, leads to the conclusion that the electronic structure of signatures induced by P atoms in the surface layer is not influenced by the proximity of a second P atom in the surface layer.

The situation is different when signatures induced by P atoms in subsurface layers are concerned: A close comparison of multi-bias topography images with V_{bias} = -0.5 V and $V_{bias} = \pm 1.0$ V (6.19) reveals that there is a threshold distance (d_T) with $d_T \approx 10$ nm for two subsurface signatures along the π-bonded chains at -0.5 V. For $d<d_T$, signatures which appear at ± 1.0 V are suppressed at -0.5 V (red circles in Fig. 6.20). The case of correlations between three P atoms in subsurface layers is depicted in the yellow framed area of figure 6.20. At +1.0 V, the distance between the middle and the left one is smaller than the minimal distance ($d_1<d_T$) while the distance between middle and left P signature is larger ($d_2>d_T$). At a voltage of -0.5 V, the signature in the middle is shifted to fit d_T. This behaviour was found only in π-bonded chain direction and for subsurface P atoms, while no such shifting is found perpendicular to the π-bonded chains or for P atoms at surface sites.

The phenomenon of suppressed or shifted signatures at -0.5 V may be explained by the high value for $\lambda_{||}$ calculated in section 6.3.1. For distances below $\lambda_{||}$, the wave functions of electrons in SCB states may not have two maxima, and the resonance is suppressed or shifted laterally to fit $\lambda_{||}$. The fact that P atoms in the surface layer show simple superpositions of the contrast patterns indicates that a major contribution to the P induced contrast is independent of the restriction of $\lambda_{||}$ in the case of surface atoms.

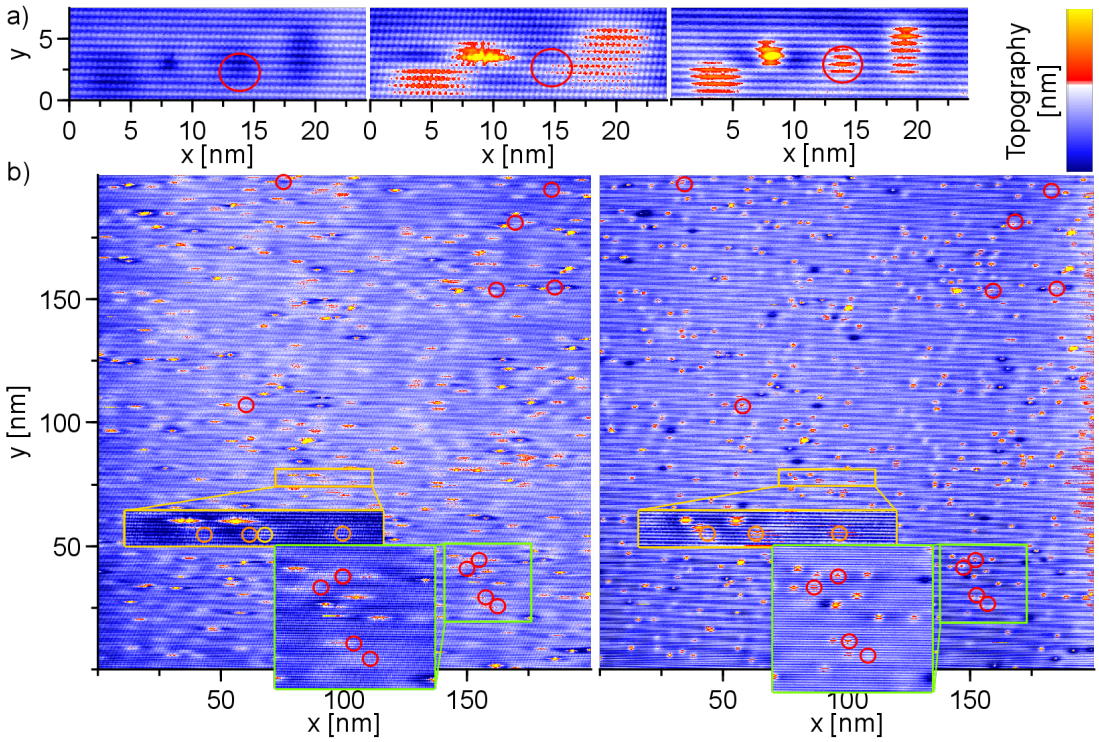

Figure 6.20: *Signatures which are visible at ±1.0 V are suppressed at -0.5 V if the distance in π-bonded chain direction is shorter than ∼10 nm. Red circles mark positions of suppressed signatures.*
(a-c) High resolution images at -1.0 V (a), -0.5 V (b), and +1.0 V (c).
(d+e) Large scale images at -0.5 V (d) and +1.0 V (e). The green and yellow framed insets show enlarged images of he framed areas. In the green framed area, the signatures are suppressed at -0.5 V while the yellow framed area shows a shifted signature at -0.5 V (orange circles mark the position of the signatures at +1.0 V, the yellow circle marks the shifted position)(The entire topography images for all bias voltages may be found in chapter Appendix).

6.6 Apparent Barrier Height

Figure 6.21 presents the results of a series of I(z,V) measurements at different positions. At each voltage step, an average over 10 I(z) measurements is taken for all measurements. ϕ(z,V) is calculated from the I(z,V) measurements according to equation 3.24 for plots b-m. For the free surface, the indented position next to P atoms, a subsurface P atom, and a P atom in the surface layer, ABH values are determined in three different voltage ranges. The range from -2.0 V to +1.5 V mainly presents signatures from the bulk states. Surface state signatures show in the voltage range between -1.0 V and +0.7 V and gap states dominate in the range from -0.5 V to +0.1 V.

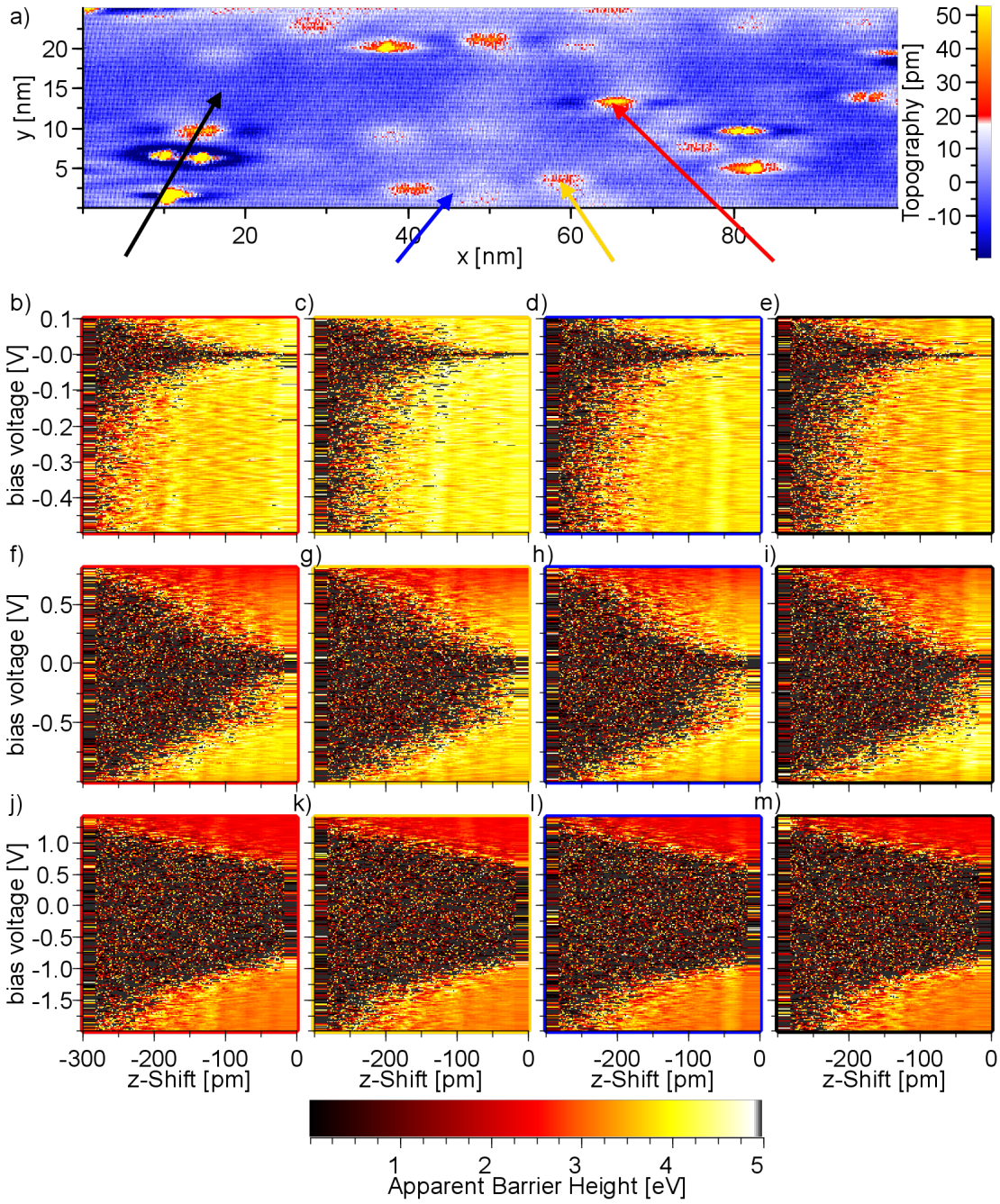

Figure 6.21: *Comparison of ABH(z,V) values of free surface (black), position with reduced height near P atom (blue), subsurface P atoms (yellow), and P atoms at surface sites (red):*
(a) Topography image (arrows mark positions of ABH measurements) [V_{bias} = -0.5 V ; I_t = 0.1 nA; T = 5.6 K].
(b-e) ABH(z,V) in the voltage range of the surface band gap.
(f-i) ABH(z,V) in the voltage range of the bulk band gap.
(j-m) ABH(z,V) with major contribution from the bulk bands.

The characteristics of the voltage dependence of these ABH measurements are the same as for the comparison of a positively and a negatively buckled domain (Fig. 4.7), although the actual ABH values are lower. This may be due to the fact that the measurements were performed on different samples with different tips. The ABH is very sensitive to the tip configuration.

The main results of the ABH measurements are the same for all positions. The BCB shows the lowest value with $\sim$2.5 eV, next come BVB and SCB with $\sim$3.5 eV and SVB with $\sim$3.9 eV. The highest ABH values and thus the shortest decay lengths are found for states in the band gap, there is a difference of nearly 2.0 eV between gap states and BCB. The gap states are also the only part of the investigated voltage range that shows a difference between the positions. Subsurface P atoms show an ABH of $\sim$4.5 eV while the ABH of the free surface is only $\sim$3.5 eV in the band gap. Directly above the surface P atom and at the indented position near a P atom the ABH values are slightly above respectively below 4.0 eV.

6.7 Conclusion

The signatures of substitutional P atoms in Si(111)-2$\times$1 have been investigated for different configurations. P atoms at each of the four different sites of the Si(111)-2$\times$1 surface unit cell exhibit distinct contrast patterns at -1.0 V and -0.5 V for positive buckling. The assignment of the contrast patterns to the sites is possible because of geometric relations. These distinct contrast patterns are identical for positively and negatively buckled π-bonded chains except for the voltages at which the contrast patterns occur. For negative buckling the voltages are -0.5 V and -0.3 V. Two contrast patterns of P atoms in pushed-up reconstructions instead of substitutional sites were identified by comparison with measurements and DFT calculations for Sb and Bi in Si(111)-2$\times$1, where signatures of such pushed-up reconstructions are commonly found [42]. The contrast patterns are also the same for free π-bonded chains and for short ones with defects in the vicinity.

In defect-free areas, signatures induced by P atoms positioned up to three layers beneath the Si(111)-2$\times$1 surface are found. The signatures generally resemble the signatures induced by P atoms in the surface but they are more diffuse.

The origin of the P induced contrast pattern was further investigated using dI/dV measurements. As the contrast pattern at voltages in the surface band gap is extended over a length of $\approx$10 nm, it cannot be a defect state of the P atom, because the defect states are highly localised on a distance of less than one

unit cell [45]. Comparison with studies on single metal atoms on metal surfaces with a dominating surface state [75,76] and impurities on 2D-metals [77,78] leads to the conclusion that these extended contrast are caused by bound states which result from a coupling of the defect states to the surface states. This is also the cause for the anisotropic form of the signatures, as the surface band structure allows only electrons with large wave length of $\approx$8 nm in π-bonded chain direction to occupy the lowest part of the SCB and the upper part of the SVB. Disorder leads to the formation of a Coulomb gap due to the reduced length of the π-bonded chains, which in turn causes a change in the nature of the bound state. As coupling to the SCB is suppressed by the presence of the Coulomb gap, the potential of the P atom couples to the SVB, instead.

Chapter 7

Summary

In order to characterize dopant atoms and surface defects in the Si(111)-2×1 surface, it is essential to thoroughly understand the pure surface itself. While the electronic structure of the surface unit cell, including the LDOS distributions of empty and occupied states, is described in great detail in references [19] and [68], an important question remained unanswered: What is the impact of the buckling type on the topographic and electronic structure of the Si(111)-2×1 surface? Once this is understood, one can investigate surface defects, such as domain boundaries, and dopant atoms. Considering the dopant atoms, it is necessary to understand the way they are placed in the surface (substitutional or in a new reconstruction or interstitial), their distribution (statistical or clusters) and their electronic signature. After these questions are answered for individual dopant atoms in an otherwise defect-free surface, correlations between two or more dopant atoms and the impact of disorder, such as surface steps, domain boundaries and adsorbate atoms, may be considered.

In this thesis, three different aspects of the Si(111)-2×1 surface are investigated in more detail: positive and negative buckling of the π-bonded chains, mobility of domain boundaries and signatures of P atoms, which are present due to the n-type doping of the samples. In the first part, domain boundaries are utilised in order to determine whether two Si(111)-2×1 domains are buckled differently considering distances between the 'up'-atoms of frontally meeting π-bonded chains of the two domains. dI/dV measurements at 6K of domains with long, defect-free π-bonded chains of both buckling types do not only show the band gap of π-bonded chains with positive (E_{Gp} = 520 (20) mV) and negative buckling (E_{Gn} = 290 (20) mV), but permit also the determination of the relative energetic positions of the surface bands of the two buckling types. The results of these measurements are in excellent agreement with DFT-calculations by M. Pötter and M. Rohlfing [31].

The tip induced movement of domain boundaries between positively and negatively buckled domains is treated in the second part of this thesis. At low positive and negative voltages, the position of a domain boundary may be reversibly altered by up to 8 nm in favour of the domain with negative buckling. The movement is largest in voltage regions where surface states are available for π-bonded chains with negative buckling but not for positively buckled π-bonded chains. The extent of movement is not influenced by the amount of tunnelling current or the tip sample distance. As a comparison of measurements with the tip scanning parallel to the π-bonded chains to measurements with a perpendicular scan direction indicates, the trigger for the movement is transmitted along the π-bonded chains and suppressed perpendicular to them.

The last and major part of this thesis is concerned with the signatures of the dopant P atoms. These atoms are located, statistically distributed, at substitutional sites in bulk and surface. The Si(111)-2$\times$1 surface offers four different sites, and all signatures of P atoms in the surface layer can be assigned to one of these sites. P atoms induce the same contrast pattern for positive and negative buckling, except for the voltage values at which the contrast patterns occur. These depend on the surface states which are at different energetic positions for the two buckling types. We investigated π-bonded chains with a length from 10 nm up to more than 1 μm. In these limits, the chain length does not affect the topographic contrast patterns of the signatures induced by P atoms at the different surface sites.

Signatures of P atoms beneath the Si(111)-2$\times$1 surface are attributed to three subsurface layers. This is supported by counts of signatures which show even numbers for signatures of P atoms in the surface layer and in the each of the three subsurface layers, as can be expected from a large number of statistically distributed donor atoms.

The origin of the contrast patterns at low negative voltages, which extend over 8 nm in π-bonded chain direction, cannot be the defect state of the P atoms alone, as this defect state is highly localised within less than one surface unit cell [45]. The comparison of dI/dV measurements of P induced signatures to dI/dV spectra of single metal atoms on metal surfaces shows that the origin of these signatures are bound states which split-off from the surface states. As electrons at the band edges of the surface states must have a minimal wavelength of $\lambda_{||} = 7.4$ nm in π-bonded chain direction, the bound states also show this spatial extension.

We can distinguish between three cases where a bound state (or resonance) occurs: The potential of P atoms located in the surface layer of free π-bonded chains causes a bound state which splits-off from the SCB and is located directly beneath the surface band minimum. The potential of subsurface P atoms is

weaker and results in a surface state resonance in the lower part of the SCB. The third case are P atoms in the surface layer of short π-bonded chains. Their potential also induces a bound state, but this bound state is split-off from the SVB instead of the SCB, due to the presence of a Coulomb gap at E_F which prevents the coupling between the potential of the P atom and the SCB.

Appendix

In this appendix, additional and larger STM images are shown. Due to their size, STM images for only one or two bias voltages of a large-scale multi-bias were presented in the main part of the thesis.

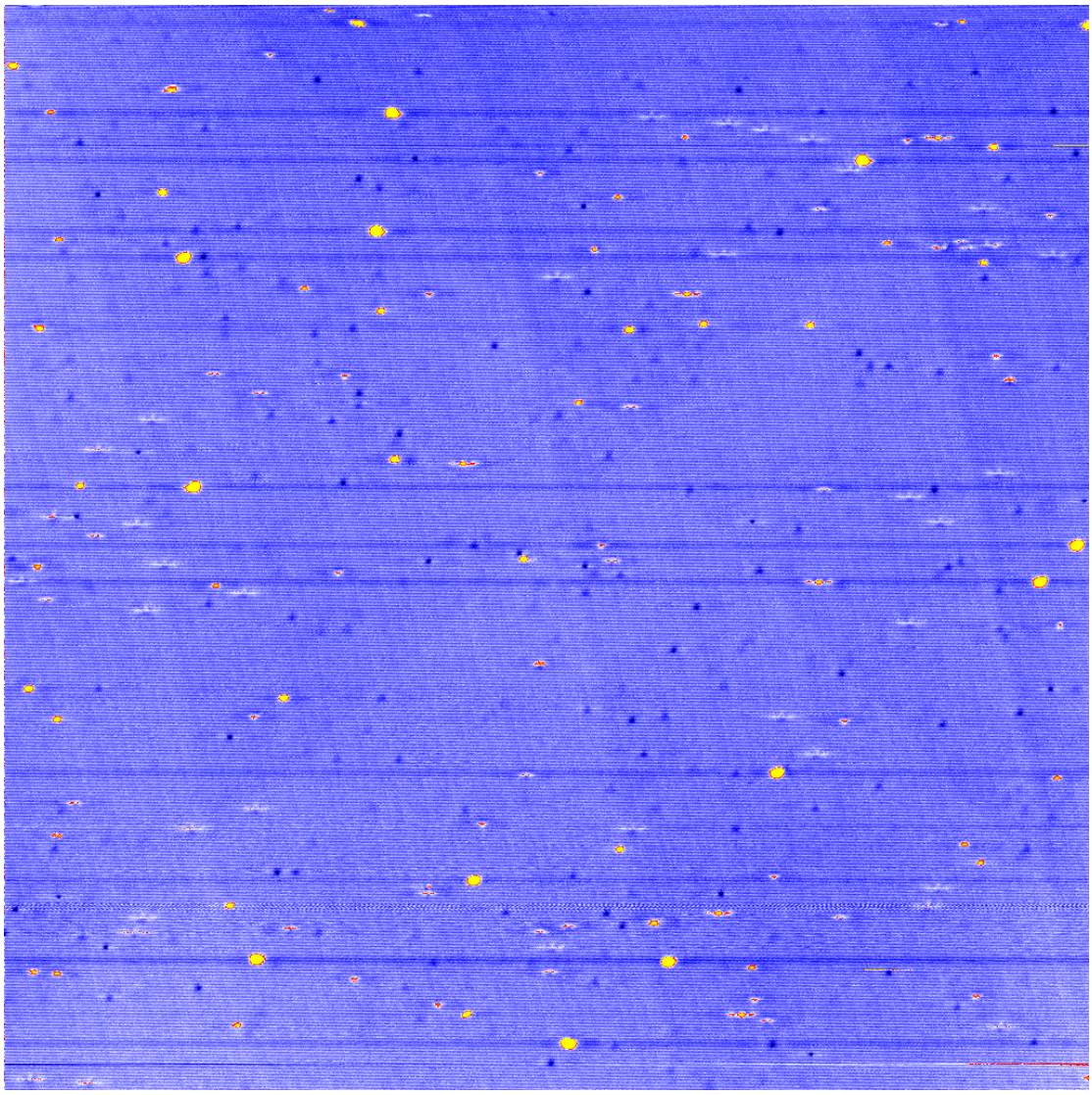

Figure 7.1: *Entire topography image at V_{bias} = -2.0 V from a 200 nm×200 nm multi-bias data set with atomic resolution – corresponds to Fig. 6.12b*

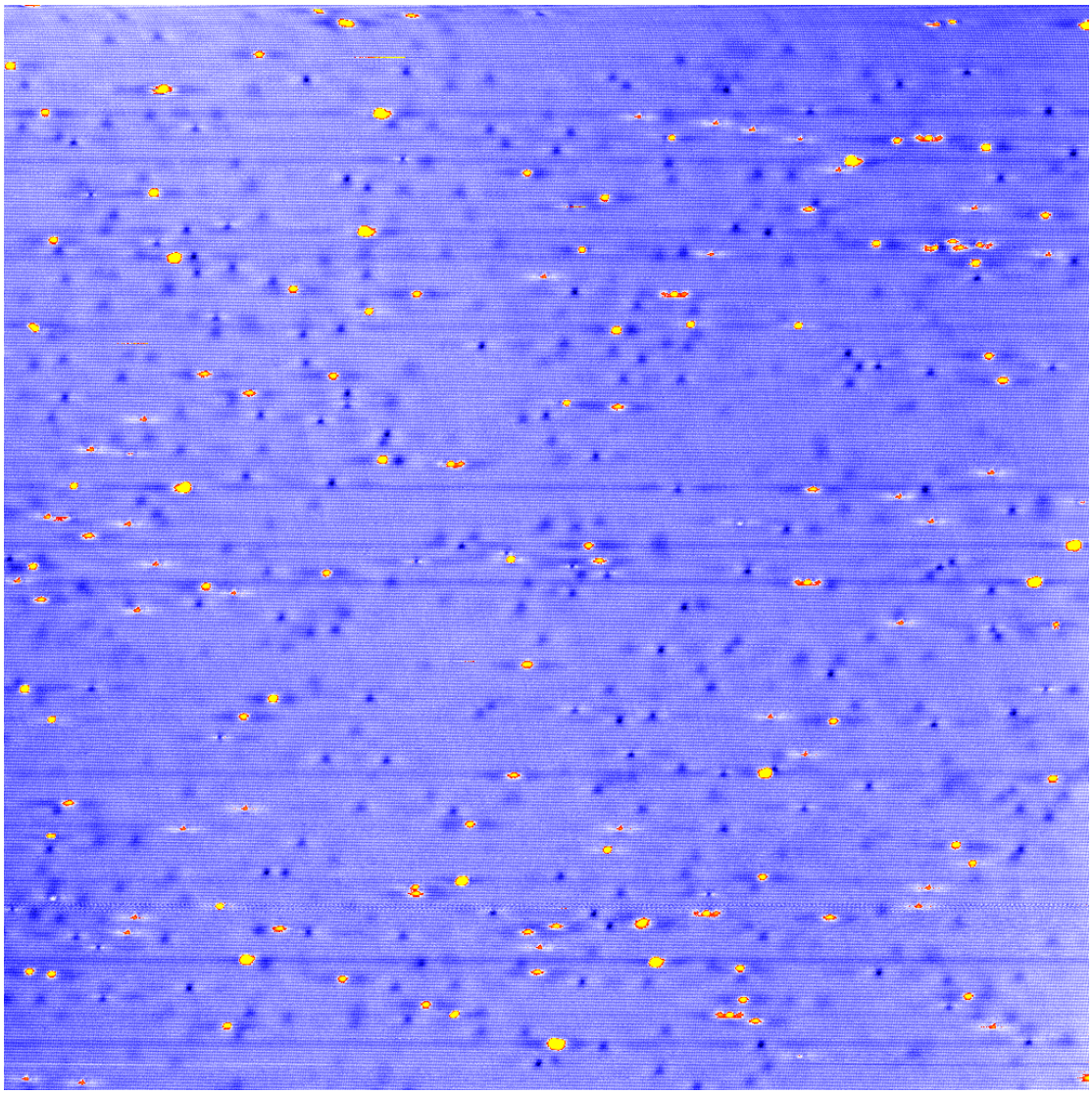

Figure 7.2: *Entire topography image at V_{bias} = -1.0 V from a 200 nm×200 nm multi-bias data set with atomic resolution – corresponds to Fig. 6.12c*

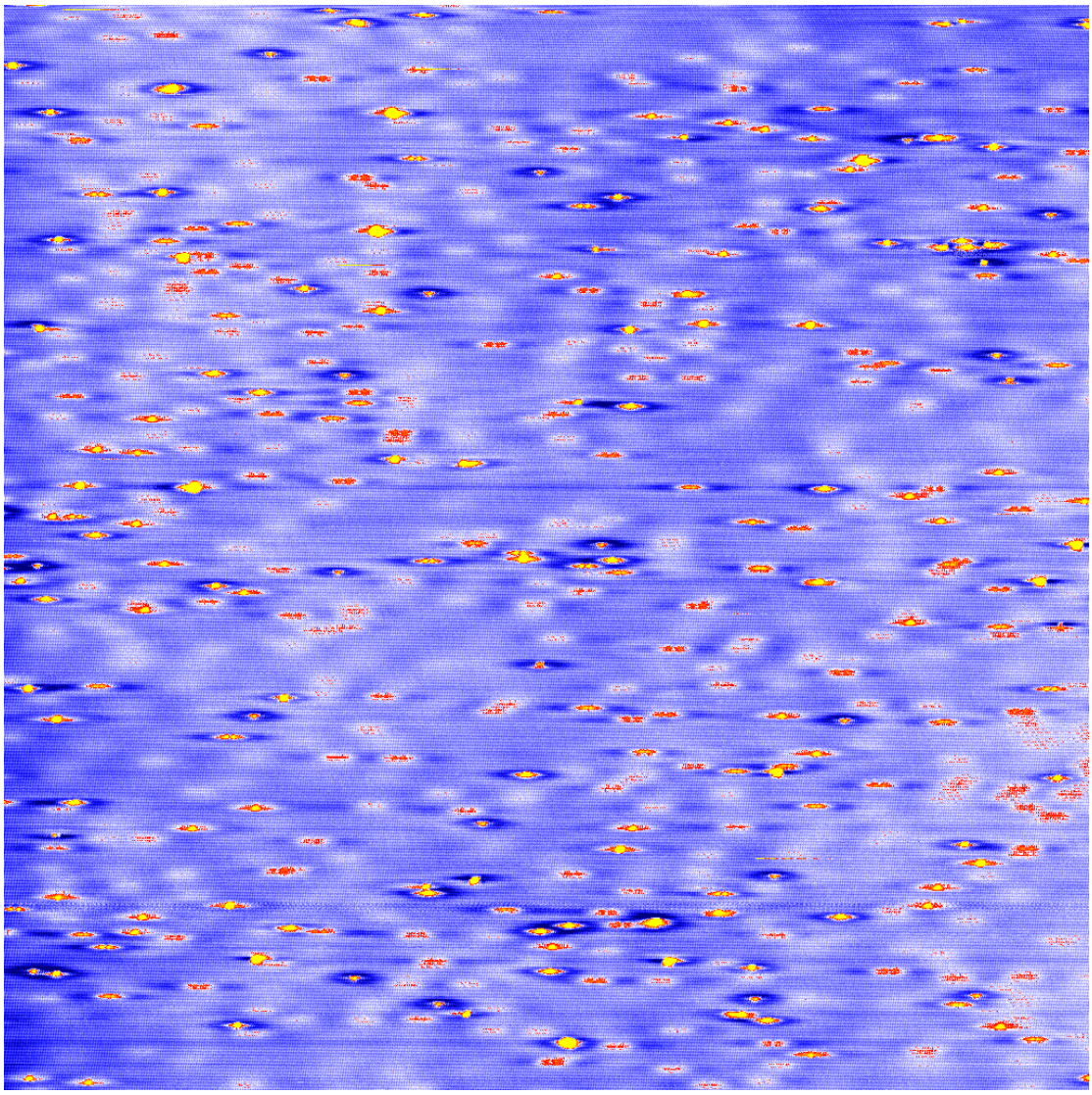

Figure 7.3: *Entire topography image at V_{bias} = -0.5 V from a 200 nm×200 nm multi-bias data set with atomic resolution – corresponds to Fig. 6.12d*

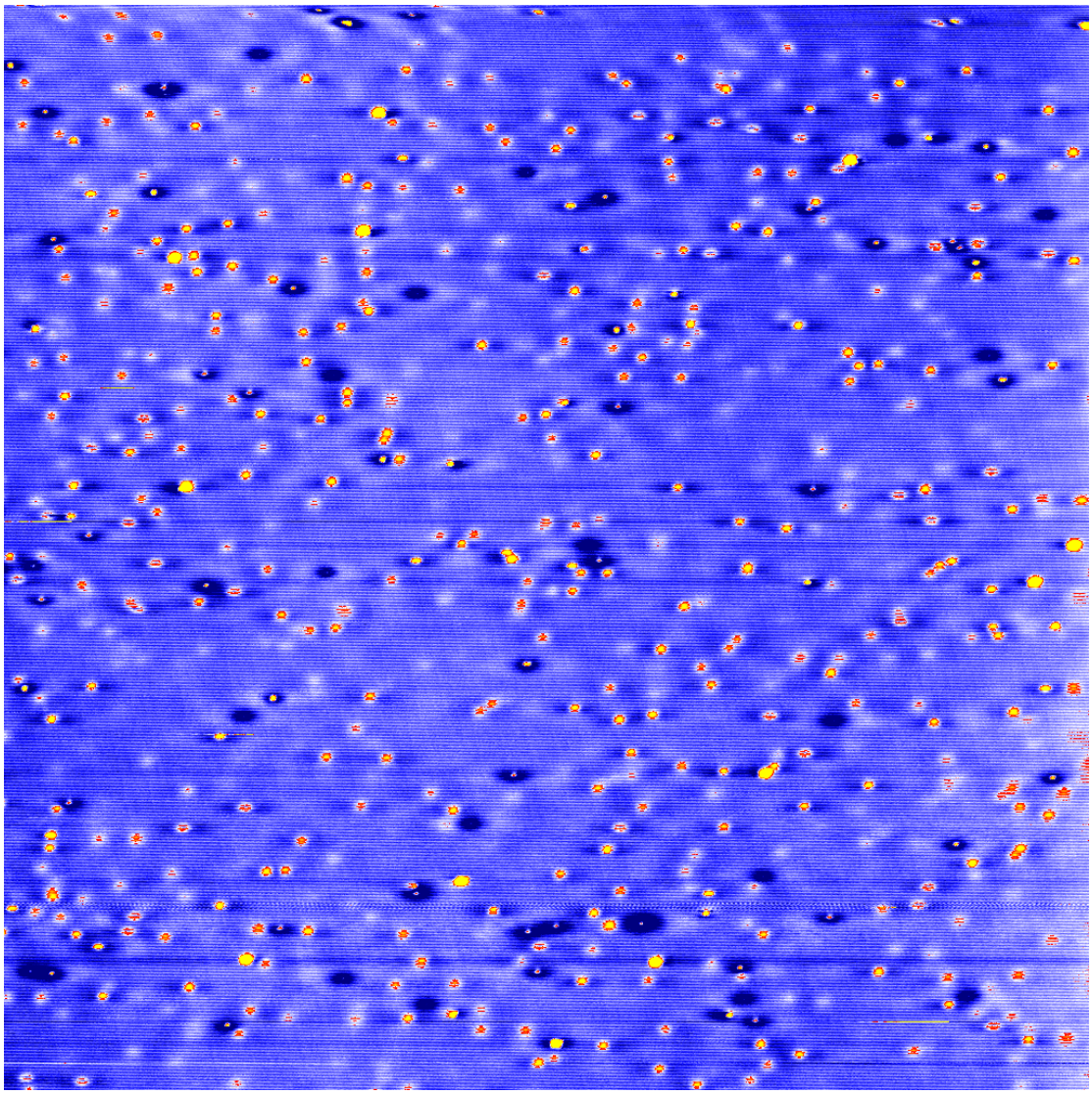

Figure 7.4: *Entire topography image at V_{bias} = +1.0 V from a 200 nm×200 nm multi-bias data set with atomic resolution – corresponds to Fig. 6.12e*

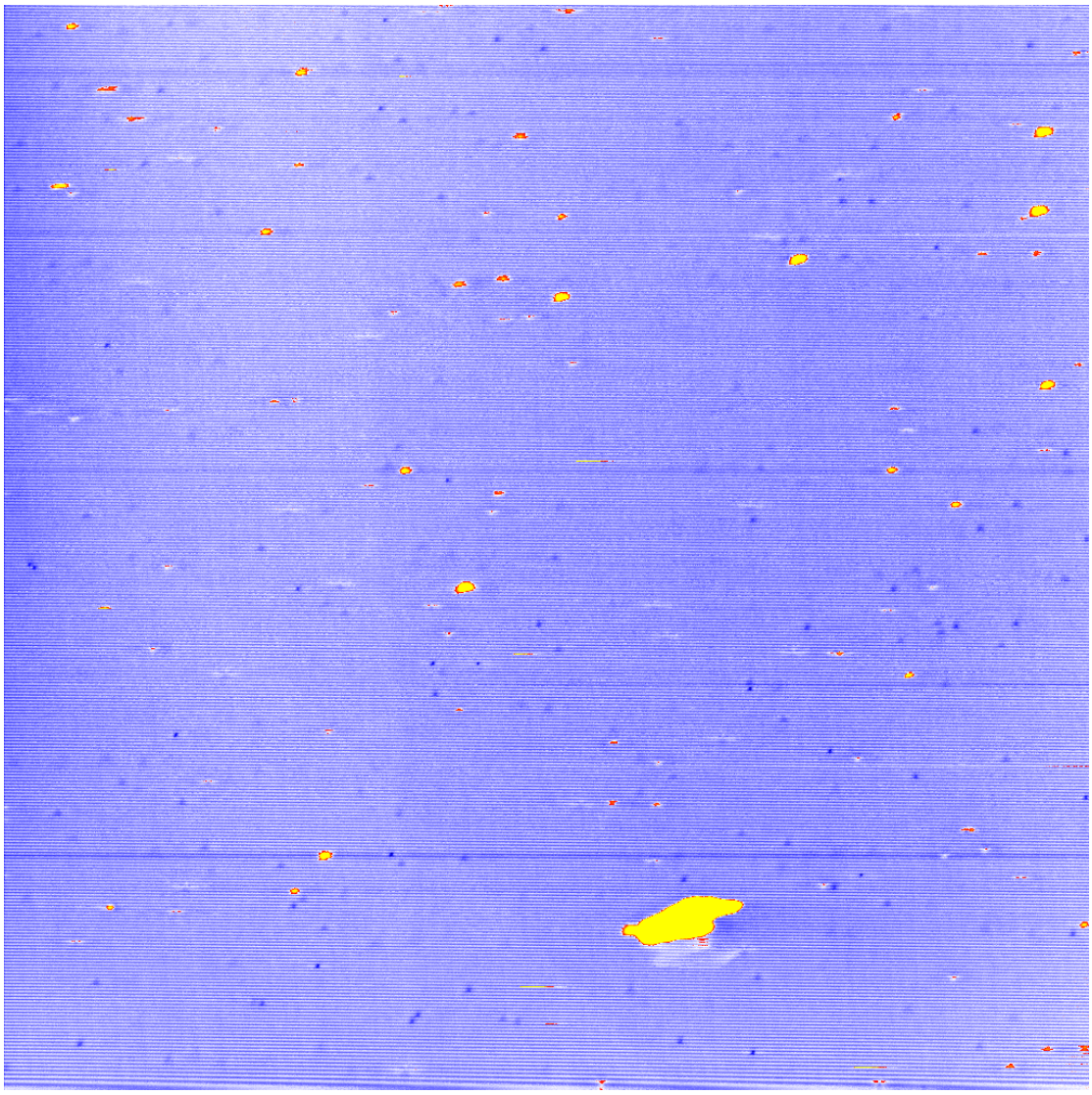

Figure 7.5: *Additional topography image at V_{bias} = -2.0 V from a 200 nm×200 nm multi-bias data set with atomic resolution – same data set as Fig. 6.20d+e*

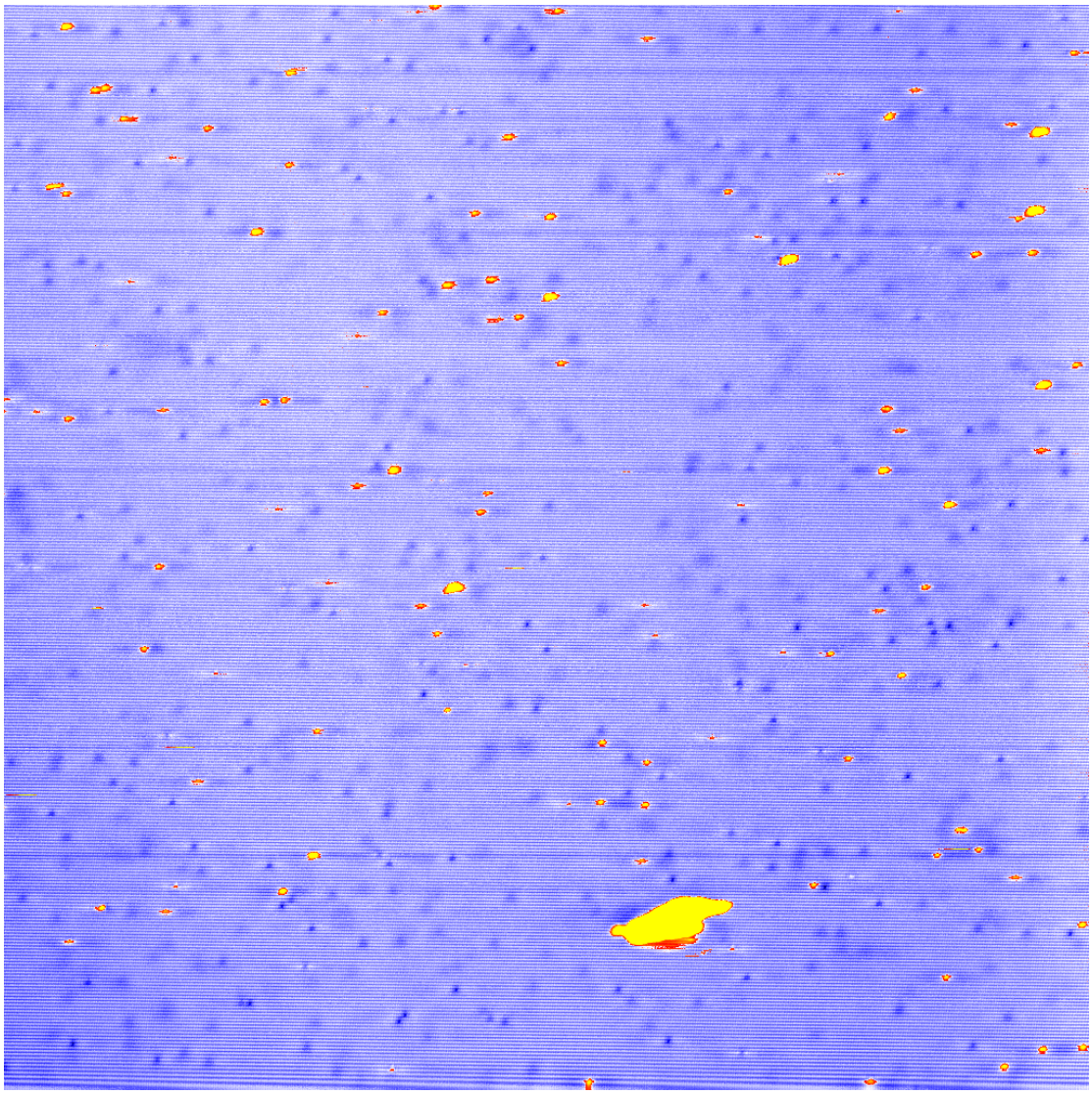

Figure 7.6: *Additional topography image at V_{bias} = -1.0 V from a 200 nm×200 nm multi-bias data set with atomic resolution – same data set as Fig. 6.20d+e*

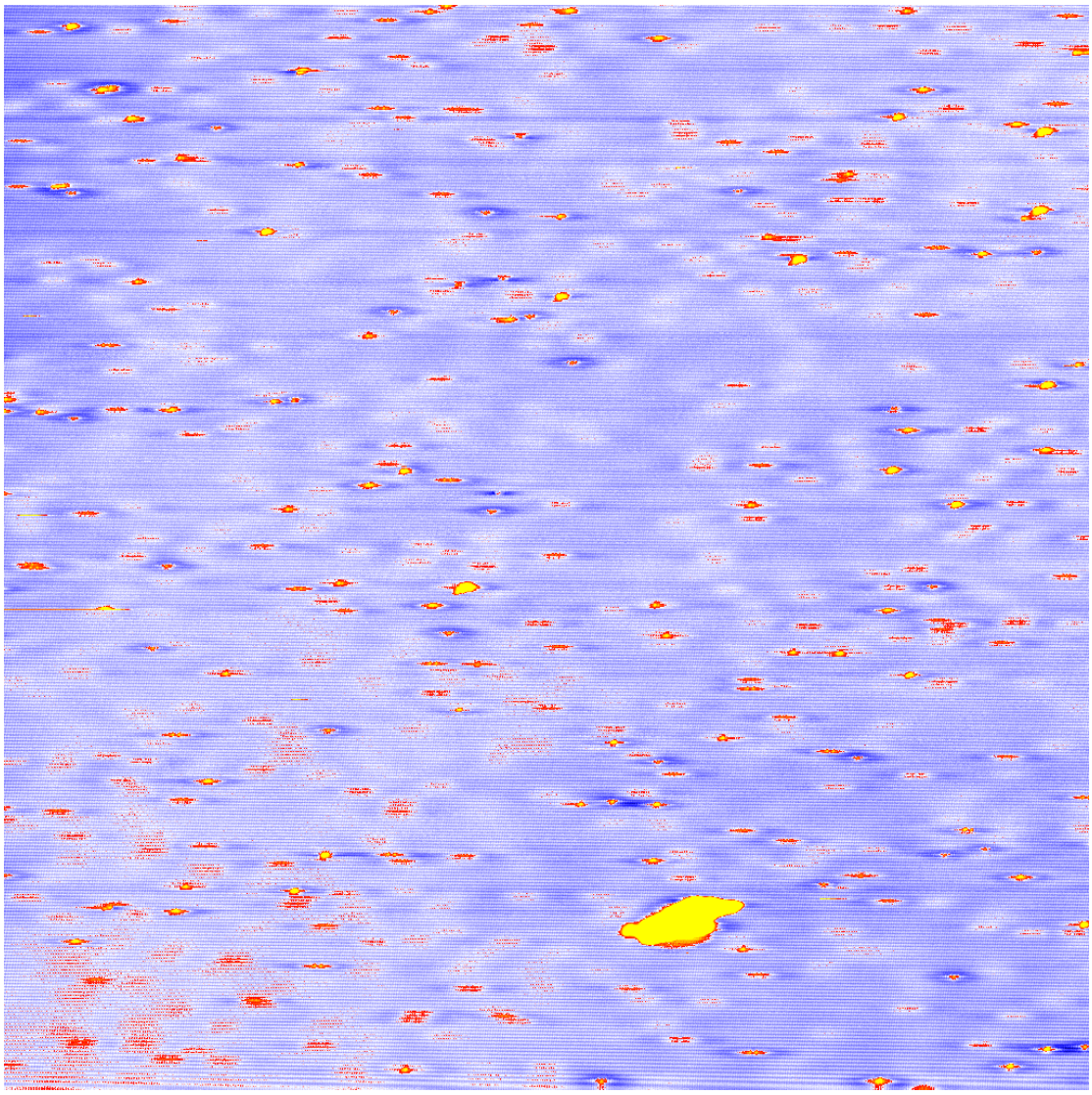

Figure 7.7: *Enlarged topography image at V_{bias} = -0.5.0 V from a 200 nm×200 nm multi-bias data set with atomic resolution – corresponds to Fig. 6.20d*

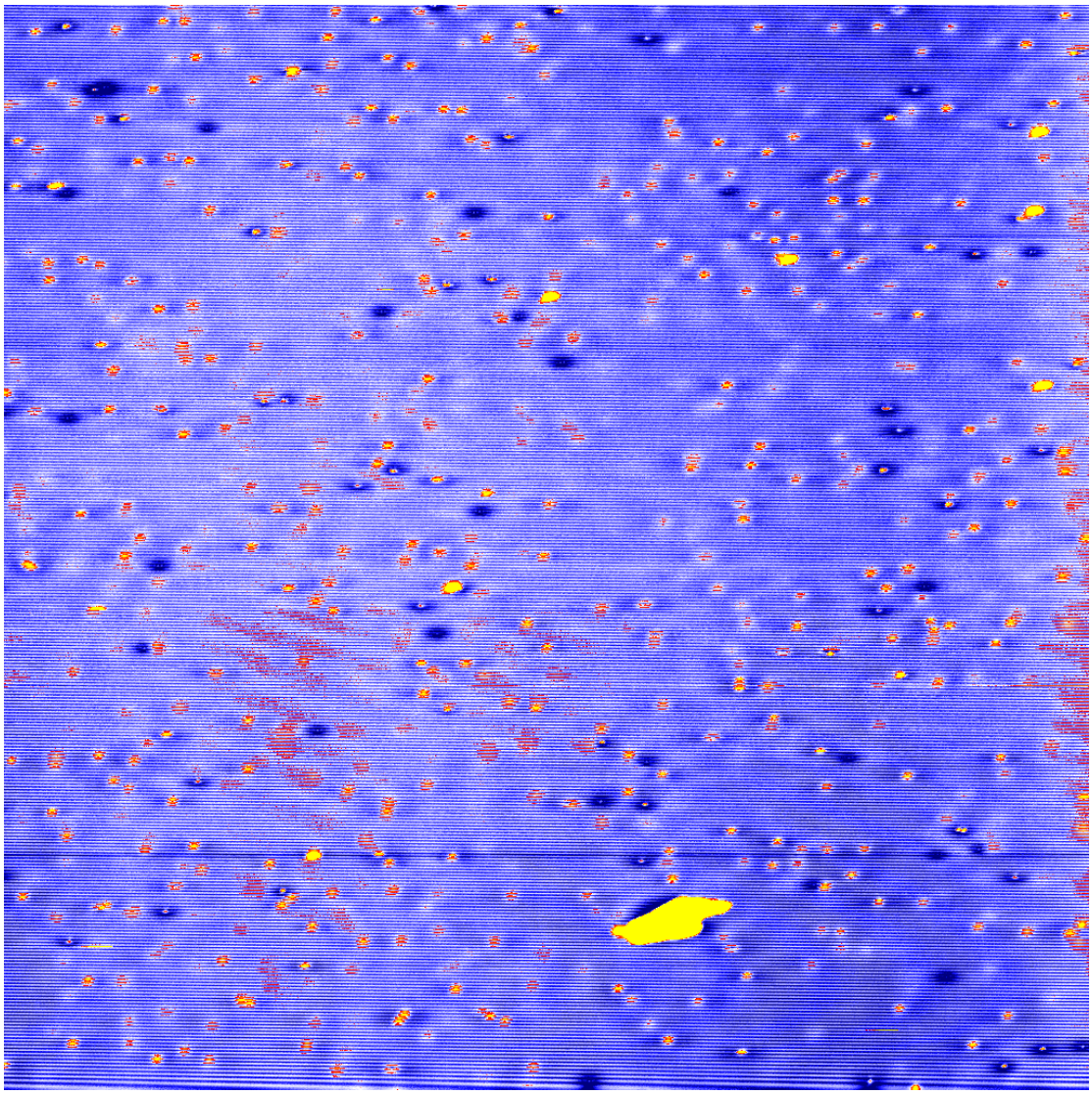

Figure 7.8: *Enlarged topography image at V_{bias} = +1.0 V from a 200 nm×200 nm multi-bias data set with atomic resolution – corresponds to Fig. 6.20e*

Abbrevations

Si	silicon
Ge	germanium
P	phosphorus
B	boron
As	arsenic
Ag	silver
Co	cobalt
Sb	antimony
Bi	bismuth
GaAs	gallium-arsenide
AlAs	aluminum-arsenide
PtIr	platinum-iridium
KOH	potassium hydroxide
W	tungsten
$\mathbf{H_2}$	hydrogen
$\mathbf{H_2O}$	water
$\mathbf{WO_4^{2-}}$	tungsten oxide
LHe	liquid helium
$\mathbf{LN_2}$	liquid nitrogen
n-type	doping with negative charge carriers
p-type	doping with positive charge carriers
STM	scanning tunnelling microscopy
AFM	atomic force microscopy
MFM	magnetic force microscopy
KPFM	Kelvin probe force microscopy
LEED	low energy electron diffraction
RHEED	reflection high energy electron diffraction
LEEM	low energy electron microscopy
FIM	field ion microscopy
SEM	scanning electron microscopy
ARPES	angle resolved photo electron spectroscopy
DFT	density functional theory
CITS	current imaging tunnelling spectroscopy
$\mathbf{V}_{bias}$	sample bias voltage
$\mathbf{I}_T$	tunnelling current

N_D	doping concentration
T	temperature
RT	room temperature
LT	low temperature
LDOS	local density of states
DOS	density of states
BVB	bulk valence band
BCB	bulk conduction band
SVB	surface valence band
SCB	surface conduction band
dI/dV	differential conductivity
ABH	apparent barrier height
E_F	Fermi energy
λ_F	Fermi wavelength
$\lambda_{\|\|}$	Fermi wavelength parallel to π-bonded chains
$k_{\|\|}$	reciprocal vector corresponding to $\lambda_{\|\|}$
E_G	width of the band gap
λ_D	Debye length
ρ	charge density
d_T	threshold distance
V_T	threshold voltage
DAS	dimer-adatom-stacking fault
1D	one-dimensional
2D	two-dimensional
3D	three-dimensional
4D	four-dimensional
PI	proportional-integral
UHV	ultra-high vacuum
'GoeSTM'	'Göttinger STM Tool for Measurements'
I/O-card	in- and output card
DSP	digital signal processor
DAC	digital analogous converter
ADC	analogous digital converter

Bibliography

[1] J. A. STROSCIO, R. M. FEENSTRA, and A. P. FEIN, *Phys. Rev. Lett.* **57**, 2579 (1986).

[2] R. M. FEENSTRA, W. A. THOMPSON, and A. P. FEIN, *Phys. Rev. Lett.* **56**, 608 (1986).

[3] R. M. FEENSTRA and J. A. STROSCIO, *Phys. Rev. Lett.* **59**, 2173 (1987).

[4] R. FEENSTRA, J. A. STROSCIO, and A. FEIN, *Surface Science* **181**, 295 (1987).

[5] G. BINNIG, H. ROHRER, C. GERBER, and E. WEIBEL, *Physical Review Letters* **49**, 57 (1982).

[6] G. BUSSETTI, B. BONANNI, S. CIRILLI, A. VIOLANTE, M. RUSSO, C. GOLETTI, P. CHIARADIA, O. PULCI, M. PALUMMO, R. DEL SOLE, P. GARGIANI, M. G. BETTI, C. MARIANI, R. M. FEENSTRA, G. MEYER, and K. H. RIEDER, *Phys. Rev. Lett.* **106**, 067601 (2011).

[7] I. APPELBAUM, T. WANG, S. FAN, J. D. JOANNOPOULOS, and V. NARAYANAMURTI, *Nanotechnology* **12**, 391 (2001).

[8] K. SAGISAKA, D. FUJITA, and G. KIDO, *Phys. Rev. Lett.* **91**, 146103 (2003).

[9] D. RIEDEL, M. LASTAPIS, M. G. MARTIN, and G. DUJARDIN, *Phys. Rev. B* **69**, 121301 (2004).

[10] Y. TAKAGI, Y. YOSHIMOTO, K. NAKATSUJI, and F. KOMORI, *Surface Science* **559**, 1 (2004).

[11] K. SAGISAKA and D. FUJITA, *Phys. Rev. B* **71**, 245319 (2005).

[12] K. SEINO, W. G. SCHMIDT, and F. BECHSTEDT, *Phys. Rev. Lett.* **93**, 036101 (2004).

[13] J. NAKAMURA and A. NATORI, *Phys. Rev. B* **71**, 113303 (2005).

[14] T. TRAPPMANN, C. SÜRGERS, and H. v. LÖHNEYSEN, *Applied Physics A: Materials Science & Processing* **68**, 167 (1999), 10.1007/s003390050872.

[15] P. STUDER, S. R. SCHOFIELD, G. LEVER, D. R. BOWLER, C. F. HIRJIBEHEDIN, and N. J. CURSON, *Phys. Rev. B* **84**, 041306 (2011).

[16] G. L. PEARSON and J. BARDEEN, *Phys. Rev.* **75**, 865 (1949).

[17] H. VON LÖHNEYSEN, *Royal Society of London Philosophical Transactions Series A* **356**, 139 (1998).

[18] T. TRAPPMANN, C. SÜRGERS, and H. LÖHNEYSEN, *EPL (Europhysics Letters)* **38**, 177 (1997).

[19] J. K. GARLEFF, M. WENDEROTH, K. SAUTHOFF, R. G. ULBRICH, and M. ROHLFING, *Phys. Rev. B* **70**, 245424 (2004).

[20] K. TAKAYANAGI, Y. TANISHIRO, M. TAKAHASHI, and S. TAKAHASHI, *Journal of Vacuum Science & Technology A* **3**, 1502 (1985).

[21] C. KITTEL, *Einführung in die Festkörperphysik*, R Oldenbourg Verlag, Wien, 1996.

[22] G. BINNIG, H. ROHRER, C. GERBER, and E. WEIBEL, *Phys. Rev. Lett.* **50**, 120 (1983).

[23] R. WIESENDANGER, *Scanning Tunneling Microscopy and Spectroscopy - Methods and Applications*, Cambridge Unversity Press, Cambridge, 1994.

[24] K. C. PANDEY, *Phys. Rev. Lett.* **47**, 1913 (1981).

[25] F. J. HIMPSEL, P. M. MARCUS, R. TROMP, I. P. BATRA, M. R. COOK, F. JONA, and H. LIU, *Phys. Rev. B* **30**, 2257 (1984).

[26] M. ROHLFING and S. G. LOUIE, *Phys. Rev. Lett.* **83**, 856 (1999).

[27] S.-H. LEE and M.-H. KANG, *Phys. Rev. B* **54**, 1482 (1996).

[28] T. K. A. SPAETH, Rastertunnelmikroskopuntersuchungen zum Vorwärts- und Rückwärtsbuckling auf der Silizium(111)-2x1-Oberfläche, Master's thesis, Georg-August-Universität Göttingen, 2010, Diplomarbeit.

[29] S. NIE, R. M. FEENSTRA, J. Y. LEE, and M.-H. KANGA, *Journal of Vacuum Science and Technology A* **22**, 1671 (2004).

[30] M. ROHLFING, M. PALUMMO, G. ONIDA, and R. DEL SOLE, *Phys. Rev. Lett.* **85**, 5440 (2000).

[31] K. LÖSER, M. WENDEROTH, T. K. A. SPAETH, J. K. GARLEFF, R. G. ULBRICH, M. PÖTTER, and M. ROHLFING, *Phys. Rev. B* **86**, 085303 (2012).

[32] S. M. SZE, *Physics of Semiconductors*, John Wiley & Sons, New York, 1981.

[33] BERGMANN and SCHAEFER, *Festkörper*, volume 6 of *Lehrbuch für Experimentalphysik*, Walter de Gruyter, Berlin, 1992.

[34] F. J. HIMPSEL, P. HEIMANN, and D. E. EASTMAN, *Phys. Rev. B* **24**, 2003 (1981).

[35] R. I. G. UHRBERG, G. V. HANSSON, J. M. NICHOLLS, and S. A. FLODSTRÖM, *Phys. Rev. Lett.* **48**, 1032 (1982).

[36] P. PERFETTI, J. M. NICHOLLS, and B. REIHL, *Phys. Rev. B* **36**, 6160 (1987).

[37] F. J. HIMPSEL, G. HOLLINGER, and R. A. POLLAK, *Phys. Rev. B* **28**, 7014 (1983).

[38] A. K. RAMDAS and S. RODRIGUEZ, *Reports on Progress in Physics* **44**, 1297 (1981).

[39] H. FÖLL, Semiconductors I, Hyperscript, 2012, AMAT, University of Kiel.

[40] M. HEINRICH, C. DOMKE, P. EBERT, and K. URBAN, *Phys. Rev. B* **53**, 10894 (1996).

[41] J. K. GARLEFF, M. WENDEROTH, R. G. ULBRICH, C. SÜRGERS, and H. V. LÖHNEYSEN, *Phys. Rev. B* **72**, 073406 (2005).

[42] P. R. STUDER, Single donors in silicon for atomic scale devices, 2011.

[43] J. K. GARLEFF, M. WENDEROTH, R. G. ULBRICH, C. SÜRGERS, H. V. LÖHNEYSEN, and M. ROHLFING, *Phys. Rev. B* **76**, 125322 (2007).

[44] M. SCHÖCK, C. SÜRGERS, and H. V. LÖHNEYSEN, *Phys. Rev. B* **61**, 7622 (2000).

[45] M. ROHLFING, M. PÖTTER, J. GARLEFF, M. WENDEROTH, K. LÖSER, and R. G. ULBRICH, to be published.

[46] G. BINNIG, C. F. QUATE, and C. GERBER, *Phys. Rev. Lett.* **56**, 930 (1986).

[47] U. HARTMANN, *Journal of Applied Physics* **64**, 1561 (1988).

[48] M. NONNENMACHER, M. P. O'BOYLE, and H. K. WICKRAMASINGHE, *Applied Physics Letters* **58**, 2921 (1991).

[49] C. J. CHEN, *Introduction to Scanning Tunneling Microscopy*, Oxford University Press, New York, 1993.

[50] L. DE BROGLIE, *Nature* **112**, 540 (1923).

[51] J. E. LILIENFELD, *Physikalische Zeitschrift* **23**, 506 (1922).

[52] R. H. FOWLER and L. NORDHEIM, *Proceedings of the Royal Society of London. Series A* **119**, 173 (1928).

[53] J. R. OPPENHEIMER, *Phys. Rev.* **31**, 66 (1928).

[54] G. GAMOW, *Zeitschrift für Physik* **51**, 204 (1928).

[55] R. W. GURNEY and E. U. CONDON, *Nature* **122**, 439 (1928).

[56] H. VAN VLECK, Julian E. Mack Lecture, University of Wisconsin, unpublished, 1979.

[57] B. BLEANEY, *Contemporary Physics* **25**, 315 (1984).

[58] J. BARDEEN, *Physical Review Letters* **6**, 57 (1961).

[59] J. TERSOFF and D. R. HAMANN, *Physical Review Letters* **50**, 1998 (1983).

[60] R. J. HAMERS, *Annual Review of Physical Chemistry* **40**, 531 (1989).

[61] H. SCHLEIERMACHER, Charakterisierung von Spitzen für die Rastertunnelmikroskopie, Master's thesis, Georg-August Universität of Göttingen, 2006, Bericht über das Praxissemester.

[62] J. P. IBE, P. P. BEY, JR., S. L. BRANDOW, R. A. BRIZZOLARA, N. A. BURNHAM, D. P. DILELLA, K. P. LEE, C. R. K. MARRIAN, and R. J. COLTON, *Journal of Vacuum Science & Technology A* **8**, 3570 (1990).

[63] J. K. GARLEFF, Vergleichende Rastersonden- und lichtmikroskopische Untersuchungen der Morphologie von [110]- und [111]-Spaltflächen an Silizium, Master's thesis, Georg-August-Universität Göttingen, 2001, Diplomarbeit.

[64] B. SPICHER, private communication.

[65] S. LOTH, *Atomic scale images of acceptors in III-V semiconductors: band bending, tunneling paths and wave functions*, PhD thesis, Georg-August-Universität Göttingen, 2007.

[66] M. A. ROSENTRETER, *Rastertunnelmikroskopie auf der GaAs(110)-Oberfläche bei Temperaturen von 8 K - 300 K*, PhD thesis, Georg-August-Universität Göttingen, 1997, Dissertation.

[67] K. BESOCKE, *Surface Science* **181**, 145 (1987).

[68] J. K. GARLEFF, *Quasi-eindimensionale elektronische Zustände auf der Si(111)-2x1-Oberfläche*, PhD thesis, Georg-August-Universität Göttingen, 2005.

[69] M. ROHLFING and J. POLLMANN, *Phys. Rev. Lett.* **88**, 176801 (2002).

[70] R. M. FEENSTRA and J. A. STROSCIO, *Journal of Vacuum Science Technology B: Microelectronics and Nanometer Structures* **5**, 923 (1987).

[71] W. BLUDAU, A. ONTON, and W. HEINKE, *Journal of Applied Physics* **54** (1974).

[72] J. E. NORTHRUP and M. L. COHEN, *Phys. Rev. Lett.* **49**, 1349 (1982).

[73] K. STOKBRO, C. THIRSTRUP, M. SAKURAI, U. QUAADE, B. Y.-K. HU, F. PEREZ-MURANO, and F. GREY, *Phys. Rev. Lett.* **80**, 2618 (1998).

[74] W. SCHMIDT and K. SEINO, *Current Applied Physics* **6**, 331 (2006).

[75] L. LIMOT, E. PEHLKE, J. KRÖGER, and R. BERNDT, *Phys. Rev. Lett.* **94**, 036805 (2005).

[76] C. LIU, I. MATSUDA, R. HOBARA, and S. HASEGAWA, *Phys. Rev. Lett.* **96**, 036803 (2006).

[77] T. ANDO, A. B. FOWLER, and F. STERN, *Rev. Mod. Phys.* **54**, 437 (1982).

[78] E. DUPONT-FERRIER, P. MALLET, L. MAGAUD, and J. Y. VEUILLEN, *EPL (Europhysics Letters)* **72**, 430 (2005).

[79] J. K. GARLEFF and K. LÖSER, Phosphor-Papier.

[80] R. M. FEENSTRA, J. M. WOODALL, and G. D. PETTIT, *Phys. Rev. Lett.* **71**, 1176 (1993).

[81] K. TEICHMANN, M. WENDEROTH, S. LOTH, R. G. ULBRICH, J. K. GARLEFF, A. P. WIJNHEIJMER, and P. M. KOENRAAD, *Phys. Rev. Lett.* **101**, 076103 (2008).

[82] H. MÜTHER, Physik II - Randwertprobleme, online-script to lecture, 2005.

[83] M. PÖTTER, private communication.

[84] A. C. HEWSON, *The Kondo Problem to Heavy Fermions*, 1997.

Danksagung

Ich möchte mich bei allen bedanken, die mir diese Arbeit ermöglicht haben. Prof. Dr. Rainer G. Ulbrich danke ich für die Bereitstellung des Themas und viele hilfreiche Diskussionen. Prof. Dr. Michael Rohlfing möchte ich für die Zweitkorrektur der Arbeit danken.

Martin Wenderoth hat mit unermüdlicher Begeisterung für das Thema und immer neuen Ideen dazu beigetragen, dass ich die Lust an der Si(111)-2×1 Oberfläche nicht verloren habe. Außerdem hat er es mir als einem damals völligen Neuling im Programmieren mit seinen fundierten C++ Kenntnissen ermöglicht, die Programmiersprache quasi nebenbei bei der Arbeit an GoeSTM zu erlernen. Das Wichtigste ist aber, dass Martin immer für gute Stimmung in der Arbeitsgruppe und damit ein sehr gutes Arbeitsklima sorgt. Vielen Dank dafür!

Der gesamten AG Wenderoth (Martin Wenderoth, Bernhard Spicher, Karen Teichmann, Thomas Druga, Henning Prüser, Tim Iffländer, Philipp Kloth, Sergej Burbach, Tilll Hatje, Christian Werner, Philil Willke, Philipp Ansorg, Adrienne Ashoff, Felix Lüpke, Roland Pültz, Steffen Rolf-Pissarczyk, Steffen Weikert, Thomas Spaeth, Peter Löptien, Marco Bertelli, Jan Homoth, Lars Winking, Alexander Weißmann und Sebastian Loth) möchte ich für die schöne gemeinsame Zeit danken, mit guten Gesprächen, viel Kaffee am Teich und unvergesslichen gemeinsame Konferenzbesuchen. Aus dieser Gruppe möchte ich Thomas Spaeth, mit dem ich während seiner Diplomarbeit zur Si(111)-2×1-Oberfläche viel Spaß hatte, und Bernhard Spicher, der bei allem Fragen und Problemen zum Labor (und auch sonst) immer helfen konnte, besonders erwähnen.

Jens Garleff ist für eine Woche aus Eindhoven nach Göttingen gekommen, um mir zu zeigen, wie man aus einem Klotz Silizium Proben herstellt, die man zuverlässig im Tieftemperatur-STM untersuchen kann, vielen Dank.

Die Laborarbeit wäre nicht möglich ohne Hilfe von den Werkstätten. Für eine gute Versorgung mit flüssigem Helium haben Herr Piepenbrink und Bastian Beylandt immer gesorgt.

Ganz wichtig war für mich die Unterstützung durch meine Eltern, die immer an mich geglaubt haben.

Als letztes, dafür als wichtigstes möchte ich meinen drei Jungs, den beiden Kleinen, Jonas und Raphael, und dem Großen, Sebastian, danken. Ihr habt immer dafür gesorgt, dass die Arbeit nicht das Einzige in meinem Leben war, selbst während der Messruns.

Curriculum Vitae

Karolin Löser

geboren am 04.07.1981 in Göttingen

Staatsangehörigkeit: deutsch

vorauss. 01/2012	**Promotion zur Erlangung des Grades eines Doktors der Naturwissenschaften im Fach Physik** am IV. Physikalischen Institut der Universität Göttingen
seit 10/2012	**wissenschaftliche Mitarbeiterin** im Fachgebiet Rechnerarchitektur und Systemprogrammierung der Universität Kassel
10/2007–09/2012	**wissenschaftliche Mitarbeiterin** im IV. Physikalischen Institut der Universität Göttingen
10/2007	**Beginn der Doktorarbeit** am IV. Physikalischen Institut der Universität Göttingen
07/2007	**Diplom im Fach Physik** an der Technischen Universität Berlin
03/2006	**Beginn der Diplomarbeit** am Institut für Festkörperphysik der Technischen Universität Berlin
10/2003	**Vordiplom im Fach Physik** an der Technischen Universität Berlin
10/2001	**Beginn des Physikstudiums** an der Technischen Universität Berlin
06/2001	**Allgemeine Hochschulreife** am Grotefend Gymnasium in Hann. Münden

Göttingen, den 09. Januar 2013

Publikationen:

1. K. Löser, M. Wenderoth, T. K. A. Spaeth, J. K. Garleff, R. G. Ulbrich, M. Pötter und M. Rohlfing,
   Spectroscopy of positively and negatively buckled domains on Si(111)-2×1
   *Physical Review B***86**(8), 085303 (2012).
   URL: `http://link.aps.org/doi/10.1103/PhysRevB.86.085303`
   DOI: `http://dx.doi.org/10.1103/PhysRevB.86.085303`

2. M. Wanke, K. Löser, G. Pruskil, D. Vyalikh, S.L. Molodtsov, M. Dähne, S. Danzenbächer und C. Laubschat,
   Electronic properties of selb-assembled rare-earth silicide nanowire on Si(001)
   *Physical Review B***83**, 205417 (2011).
   URL: `http://link.aps.org/doi/10.1103/PhysRevB.83.205417`
   DOI: `http://dx.doi.org/10.1103/PhysRevB.83.205417`

3. M. Wanke, K. Löser, G. Pruskil, und M. Dähne,
   Structural and electronic properties of rare-earth silicide nanowires on Si(557)
   *Physical Review B***79**, 155428 (2009).
   URL: `http://link.aps.org/doi/10.1103/PhysRevB.79.155428`
   DOI: `http://dx.doi.org/10.1103/PhysRevB.79.155428`

4. M. Wanke, K. Löser, G. Pruskil, und M. Dähne,
   Formation of dysprosium silicide nanowires on Si(557) with two-dimensional electronic structure
   *Journal of Applied Physics***103**, 094319 (2008).
   URL: `http://jap.aip.org/resource/1/japiau/v103/i9/p094319_s1`
   DOI: `http://dx.doi.org/10.1063/1.2912990`

Präsentationen:

1. K. Löser, M. Wenderoth, T. K. A. Spaeth und R. G. Ulbrich,
   Different bandstructures of for- and backward buckled π-bonded chains of the Si(111)-2$\times$1 surface reconstruction revealed by STS-measurements
   Frühjahrstagung 2011 der DPG in Dresden.

2. T. K. A. Spaeth, M. Wenderoth, K. Löser und R. G. Ulbrich,
   The Si(111)-2x1 surface: Formation of π-bonded chains and co-existence of forward and backward buckling
   International Conference on Nanoscience and Technology (ICN+T 2010) in Beijing

3. T. K. A. Spaeth, M. Wenderoth, K. Löser und R. G. Ulbrich,
Formation of the Si(111)-2×1 reconstruction
Frühjahrstagung 2010 der DPG in Dresden.

4. T. K. A. Spaeth, M. Wenderoth, K. Löser und R. G. Ulbrich,
Coexistence of forward and backward buckled π-bonded chains on the Si(111)-2×1 surface
Frühjahrstagung 2010 der DPG in Dresden.

5. K. Löser, M. Wenderoth, T. K. A. Spaeth, J. K.Garleff und R. G. Ulbrich,
Impurity induced charge density oscillations in the π-bonded chains of the Si(111)-2×1 surface
Frühjahrstagung 2009 der DPG in Dresden.

6. T. K. A. Spaeth, M. Wenderoth, K. Löser, J. K.Garleff und R. G. Ulbrich,
Decomposition of the Si(111)-2×1 Surface Reconstruction at Room Temperature: an STM Study
Frühjahrstagung 2009 der DPG in Dresden.

7. M. Wanke, K. Löser, G. Pruskil, P. Stojanov, E. Huwald, J. R und M. Dähne,
Two-dimensional electronic structure of dysprosium silicide nanowires on Si(557)
Frühjahrstagung 2008 der DPG in Dresden.

8. K. Löser, M. Wanke, G. Pruskil und M. Dähne,
Topography and valencebandstructure of dysprosium-silicide on Si(557)
Frühjahrstagung 2007 der DPG in Dresden.